

University of Zagreb
Faculty of Science

Marko Pinterić

**ELECTRONIC PROPERTIES OF
THE SUPERCONDUCTING AND
DENSITY WAVE PHASES IN
ORGANIC ANISOTROPIC
MATERIALS**

Doctoral thesis

Zagreb, 2003.

Acknowledgements

This thesis would not appear in its present form without the kind assistance and support of a number of people and organizations. I would like to thank the following:

My supervisor dr. Silvia Tomić – for her invaluable support and guidance, as well as invested energy and time, in all phases of my scientific work, from the research to writing this thesis.

My colleagues dr. Đuro Drobac and dr. Mladen Prester – for generously making possible that a major part of the research was successfully done on their ac susceptometer, as well as for useful discussions, comments and suggestions.

My colleague Tomislav Vuletić – for the long lasting collaboration, useful discussions and all the provided help.

My colleagues dr. Ognjen Milat, dr. Bojana Hamzić and Sanja Dolanski Babić, MS – for the fruitful scientific collaboration.

All other colleagues and employees of the Institute of Physics, Zagreb – for providing an excellent and friendly working atmosphere.

Prof. dr. Kazumi Maki – for the fruitful scientific collaboration, useful discussions, comments and suggestions.

Prof. dr. Kazushi Kanoda, prof. dr. Dieter Schweitzer and prof. dr. Takahiko Sasaki – for providing the samples used in the research and useful discussions.

Prof. dr. Amir Hamzić – for accepting to be the chairman of the thesis committee and the obligingness shown in the final phase of the thesis completion.

Prof. dr. Bruno Cvikl and dr. Dean Korošak of the Faculty of Civil Engineering, Maribor – for the educational and scientific collaboration.

Ministry of education, science and sport of Republic of Slovenia – for their financial support during the course of this work.

And finally, my wife Gordana – for her love, support and patience. It is to her, as well as to my daughter Lucija and son Dominik, that I dedicate this thesis.

Contents

Introduction	4
1 Known properties of the κ-(BEDT-TTF)₂X materials	6
1.1 Phase diagram	6
1.2 Normal state properties	8
1.2.1 Crystal structure	8
1.2.2 Electronic properties	11
1.2.3 Relaxation effects	16
1.3 Insulating spin density wave state in κ -(BEDT-TTF) ₂ - Cu[N(CN) ₂]Cl	19
1.4 Superconducting state in κ -(BEDT-TTF) ₂ Cu[N(CN) ₂]Br and κ -(BEDT-TTF) ₂ Cu(NCS) ₂	20
2 Theory of unconventional superconductivity	24
2.1 Cooper pair	24
2.2 Symmetry considerations	27
2.3 Energy of elementary excitations	30
2.4 Phase transition temperature	32
2.5 Bulk properties	34
3 Experimental determination of superconducting quantities	39
3.1 ac susceptometer	40
3.2 Calibration	43
3.3 Experimental conditions	50
3.4 Penetration depth extraction	51
3.5 Superfluid density analysis	54
4 Investigation of the insulating spin density wave state	58
4.1 Samples and the experimental setup	58
4.2 Single particle resistivity	59
4.3 Non-ohmic conductivity	61

4.4	ac conductivity	63
5	Investigation of the superconducting state	67
5.1	Samples	67
5.1.1	κ -(BEDT-TTF) ₂ Cu[N(CN) ₂]Br	67
5.1.2	κ -(BEDT-TTF) ₂ Cu(NCS) ₂	69
5.2	Complex susceptibility	70
5.2.1	Anomalies in complex susceptibility	75
5.3	Penetration depth	77
5.4	Superfluid density	81
6	Discussion	89
6.1	Insulating spin density wave state	89
6.2	General remarks considering the superconducting state	91
6.3	Superfluid density	93
6.4	Remnant disorder in the superconducting state	97
6.5	Coexistence of two phases	99
7	Summary	103
	Bibliography	105
	List of publications	112
	Biography	115
	List of figures	116
	List of tables	121
	Index	122

Introduction

Superconductivity, one of the most exciting phenomena in the solid state physics, was discovered at temperature of only few Kelvin far back in time in 1911. Since then an amazing number of different classes of materials, from room temperature classical metals to cuprates, has been found showing the same properties of a truly perfect bulk conductivity and an exclusion of the magnetic flux from the interior. The temperature, at which superconductivity is detected, is increasing to higher and higher values, already enabling important technical applications and promising us that some day useable room temperature superconductors will revolutionize the way we live our everyday life.

An exciting step forward was done when in 1957 Bardeen, Cooper, and Schrieffer created their epoch making BCS theory of superconductivity. For a moment superconductivity was seen as one of the best understood many-body problems of the physics and in all materials the responsible mechanism was seemingly exactly the same. Situation was significantly changed when in 1979 heavy fermion superconductors were discovered, closely followed by organic superconductors in 1980 and high-temperature superconducting cuprates in 1986. It was found that these new superconductors exhibit unconventional properties, many of which cannot be explained in the frames of the original BCS theory. Thus the understanding of superconducting mechanism is nowadays again a topic full of questions and mystery.

In this thesis, I will try to shed a new light on the problem of understanding the ground state of the BEDT-TTF superconductors, which have been for too long the object of quarrel between different experimental and theoretical groups in the world. Despite relatively low superconducting phase transition temperatures, these materials prove to be very interesting, as they have many things in common with other classes of superconducting materials, in particular with high-temperature superconducting cuprates; That is, they are highly anisotropic, two-dimensional materials, their superconducting state is located in the vicinity of the antiferromagnetic phase, and there are indications of high electron correlations. Further, the crystal structure is

rather simple, so investigations of the BEDT-TTF materials are promising in terms of making a breakthrough in the understanding of the general properties of the superconducting mechanism. On the other hand, because of the rich cuprate-like phase diagram, it is of vital significance to understand the normal state, as well as both the superconducting and the insulating ground states. Therefore, in this thesis we study and correlate the properties of the superconducting and insulating spin density wave ground states.

Finally, it should be pointed out that ambitions of this thesis are not limited on giving another study of the ground states, but they also provide a plausible way out of the mystery of the determination of the exact superconducting symmetry in the BEDT-TTF materials. Furthermore, it will also provide a detailed description of the employed techniques and methods, which are necessary in order to obtain a reliable and complete determination of some of the magnetic properties of the studied superconductor. Therefore, it could be used not only as a bare scientific contribution to the investigation of the problem of superconductivity, but also as a manual and guide to a more reliable experimental determination of the magnetic properties in superconducting materials.

1 Known properties of the κ -(BEDT-TTF) $_2X$ materials

1.1 Phase diagram

Organic superconductivity was first reported by Jérôme *et al.* [1] in 1980 in the quasi-one-dimensional organic material (TMTSF) $_2$ PF $_6$. Further research led to various novel compounds, the most distinguished of which is the family of quasi-two-dimensional materials based on the BEDT-TTF molecule. Up to this moment, the κ -(BEDT-TTF) $_2X$ materials of this family [abbreviated as κ -(ET) $_2X$], where X represents polymerized anion, achieve the highest phase transition temperatures among low-dimensional organic superconductors, making them the most suitable for the experimental study of the superconducting state.

The first distinguished property of the κ -(ET) $_2X$ materials is the vicinity of the superconducting (SC) and antiferromagnetic (AF) ground states, as well as the paramagnetic and insulating normal states, which can be clearly seen in the proposed phase diagram for the κ -(ET) $_2X$ phase (Fig. 1.1). Kanoda argues that the metal-nonmetal transition or the crossover depicted by the shaded boundary in the figure is driven by electron correlations, which corresponds to the Mott transition [2]. This is confirmed by the calculation demonstrating that the effective Coulomb correlation value is very close to the bandwidth one. Further, three materials in this phase

κ -(BEDT-TTF) $_2$ Cu[N(CN) $_2$]Cl [abbreviated as κ -(ET) $_2$ Cl],

κ -(BEDT-TTF) $_2$ Cu[N(CN) $_2$]Br [abbreviated as κ -(ET) $_2$ Br], and

κ -(BEDT-TTF) $_2$ Cu(NCS) $_2$ [abbreviated as κ -(ET) $_2$ NCS]

have different ground states at the atmospheric pressure; That is, while the former is an antiferromagnetic insulator, the latter two are superconductors. In κ -(ET) $_2$ Cl, the applied pressure suppresses the AF state and stabilizes

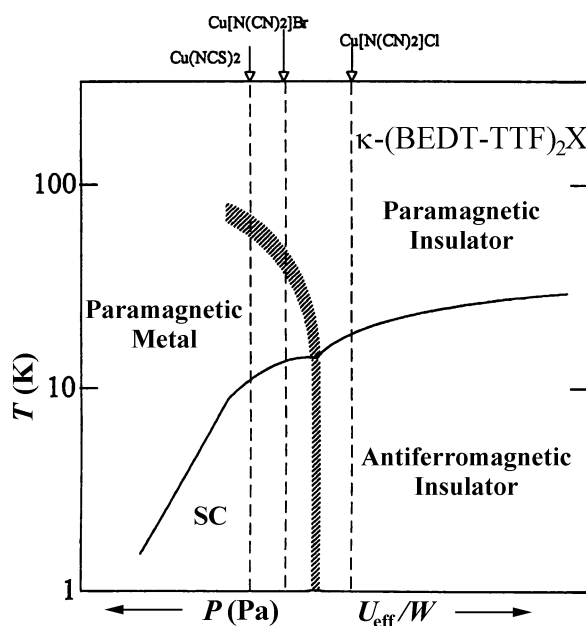


Fig. 1.1: Proposed phase diagram for κ -(ET) $_2X$ quasi-two-dimensional materials. An increase of the ratio of the effective Coulomb interaction and the bandwidth (U_{eff}/W) is analogous to the decrease of the pressure P on the material. Shaded area corresponds to the phase diagram region, in which the ratio U_{eff}/W is critical in regard to the Mott transition. “SC” denotes the superconducting phase. [2]

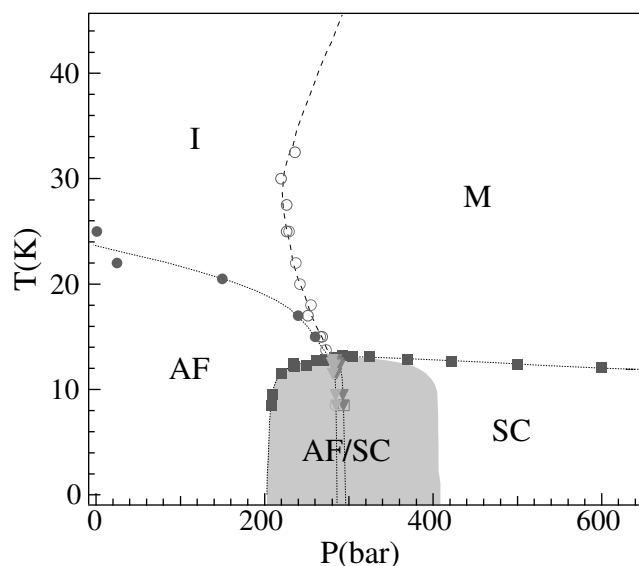


Fig. 1.2: The experimental phase diagram of κ -(ET) $_2$ Cl. “I”, “M”, “AF” and “SC” denote the insulating, metallic, antiferromagnetic and superconducting phases, respectively. Shaded area denotes region of the inhomogeneous phase coexistence, while double-dashed line represents the AF-SC boundary. [3]

the SC state [3], whereas by deuteration of κ -(ET) $_2$ Br, the ground state is gradually pushed from the SC toward the AF state [4]. The phase diagram is, therefore, quite similar to that of the cuprates if doping is replaced by pressure or deuteration.

Lefebvre *et al.* [3] studied the phase diagram of κ -(ET) $_2$ Cl experimentally using the ^1H nuclear magnetic resonance (NMR) and the ac susceptibility measurements (Fig. 1.2). Significant hysteresis in the ac susceptibility and a gradual change of the NMR line shape was discovered between 200 and 400 bars, pointing to a coexistence of the superconducting and antiferromagnetic phases. However, it remained unknown if the coexistence is of a microscopic or a mesoscopic (e.g., stripes) type.

1.2 Normal state properties

1.2.1 Crystal structure

The κ -(ET) $_2X$ compound is composed of two organic, quasi-planar molecules BEDT-TTF [bis(etilen-dithiolo)tetrathiofulvalen, abbreviated also as ET], shown in Fig. 1.3, and one polymerized anion X . The BEDT-

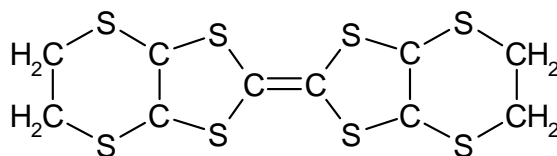


Fig. 1.3: BEDT-TTF molecule.

	b (Å)	a (Å)	c (Å)	$\varphi(b, ac)$	V (Å ³)
κ -(ET) ₂ Cl	29.979	12.977	8.480	90°	3299
κ -(ET) ₂ Br	30.016	12.942	8.539	90°	3317
	a (Å)	c (Å)	b (Å)	$\varphi(a, cb)$	V (Å ³)
κ -(ET) ₂ NCS	16.256	13.143	8.456	110.28°	1695

Table 1.1: Lattice parameters in order of size, the angle between the longest axis and the plane defined by other two axes, and the volume of the unit cell, for the compounds elaborated in this thesis.

TTF molecules form mutually orthogonal dimers, which are then arranged into the conducting layers sandwiched between the polymerized anion layers.

The κ -(ET)₂Br and κ -(ET)₂Cl crystals unit cell is orthorhombic (symmetry Pnma) and consists of two donor and two acceptor layers, that is of four BEDT-TTF dimers and four anions (Fig. 1.4). The layers coincide with the planes defined by two perpendicular crystallographic axes a and c , in a way that the BEDT-TTF dimers close the angle of 45° with axes. The third axis b coincides with the perpendicular direction to the ac planes.

On the other hand the κ -(ET)₂NCS crystal unit cell is monoclinic (symmetry P2₁) and consists of only one donor and one acceptor layer, that is of two BEDT-TTF dimers and two anions (Fig. 1.5). The layers coincide with the planes defined by two perpendicular crystallographic axes b and c , in a way that the BEDT-TTF dimers close the angle of 45° with axes. The third axis a is canted for angle of 20.28° from the perpendicular direction to the bc planes.

The reason for seemingly large discrepancy between unit cells lays in the fact that the BEDT-TTF molecules are canted differently in regard to the perpendicular direction in two successive layers in the κ -(ET)₂Br and κ -(ET)₂Cl crystals, which is not the case in the κ -(ET)₂NCS crystal. As a result, the crystallographic directions and lattice parameters are completely different. However, if the lattice parameters are written in the order of length and the volumes of the unit cells are calculated, as illustrated in Table 1.1, it is obvious that unit cells are very similar, apart from the fact that the unit

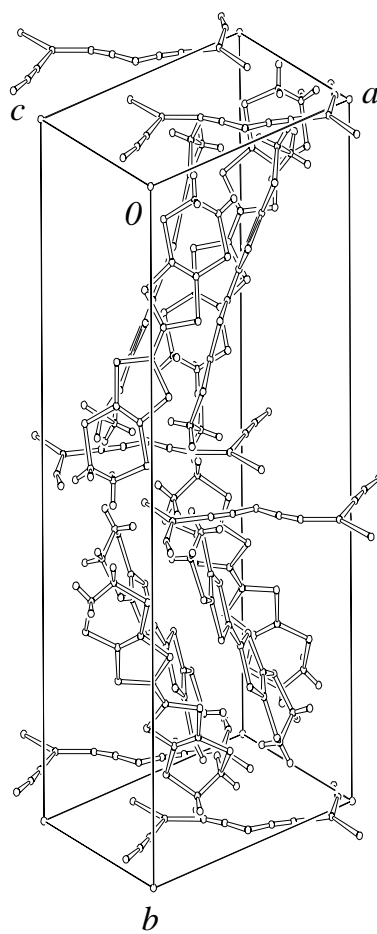


Fig. 1.4: Three-dimensional view of the unit cell for the κ -(ET)₂Cl and κ -(ET)₂Br crystals.

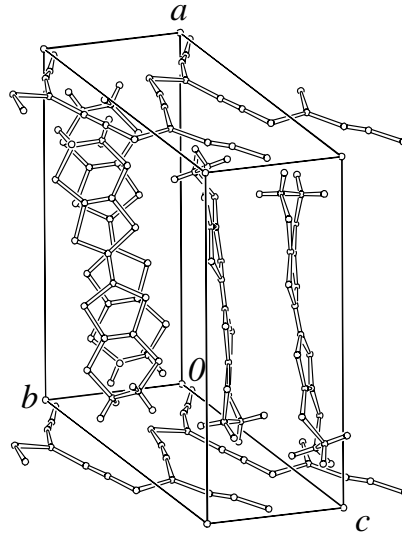


Fig. 1.5: Three-dimensional view of the unit cell for the κ -(ET) $_2$ NCS crystal.

cell of the κ -(ET) $_2$ NCS crystal is smaller by half.

1.2.2 Electronic properties

The most important fact concerning the crystal structure is that small differences do not influence important physical properties at room temperature (RT), which are in principle exactly the same for all three materials. Overlapping of the external BEDT-TTF molecular orbitals in the donor layers is strong in both planar directions, so these molecular orbitals form a two-dimensional bandwidth. On the other hand, the inter-plane coupling is very weak. The exact anisotropy data for conductivity were published only for the κ -(ET) $_2$ Br material, giving the anisotropy inside the conductive planes $\sigma_a/\sigma_c \approx 1.5$ and the anisotropy between the conductive planes and the direction perpendicular to them $\sigma_a/\sigma_b \approx 1000$ [5]. The κ -(ET) $_2X$ materials are therefore distinctly two-dimensional, which is also a prominent property of cuprates.

Conductivity at RT inside the conductive planes amounts to about $1 (\Omega\text{cm})^{-1}$ in the κ -(ET) $_2$ Cl material [6], to about $30 (\Omega\text{cm})^{-1}$ in the κ -(ET) $_2$ NCS material [7], and to the range of $1\text{--}50 (\Omega\text{cm})^{-1}$ in the κ -(ET) $_2$ Br material, depending on the conditions of the synthesis [5]. There is no significant difference among most of the samples of all materials in the temperature region between RT and 100 K, where resistivity shows a weak semiconducting behavior. However, while the κ -(ET) $_2$ Cl thermal activation of resistivity increases significantly below 60 K [8] (see Fig. 4.1 on page 60), resistivity

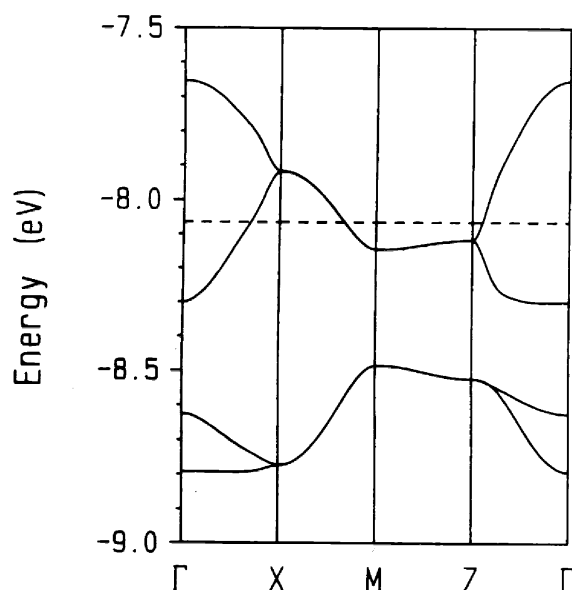


Fig. 1.6: Numerically obtained dispersion relations for the two highest occupied bands. Dashed line designates Fermi energy. [12]

of κ -(ET) $_2$ Br and κ -(ET) $_2$ NCS shows a hump around 80 K and metallic behavior below that temperature [5, 7] (see Fig. 5.1 on page 68). Situation is however complicated by the fact that the κ -(ET) $_2$ Br samples of some synthesis display a metallic behavior in the whole temperature region between RT and T_C [9] (see Fig. 5.2 on page 68).

The situation regarding resistivity is further complicated by indications that some Cu(II) may replace regular Cu(I) during synthesis, affecting the resistivity behavior [10]. The correlation between different mean free paths in samples of different syntheses and the presence of Cu(II) ions has also been suggested [11].

Using the X-ray diffraction data in the κ -(ET) $_2$ Br and κ -(ET) $_2$ Cl materials at 127 K, Geiser *et al.* [12] determined electronic structure using the tight binding calculation based on the extended Hückel method. According to this calculation, qualitatively similar results were obtained for both materials, pointing in particular to the existence of two bands (Fig. 1.6), with the values of $W_L \approx 0.31$ eV and $W_U \approx 0.65$ eV, for the lower and the upper bandwidth, respectively. The obtained total bandwidth value amounts to $W \approx 1.14$ eV. A similar band structure was obtained in the κ -(ET) $_2$ NCS material using the self-consistent orthogonalized linear combination of the atomic orbitals method [13].

A formal oxidation arrangement assigns one hole per dimer, so the upper

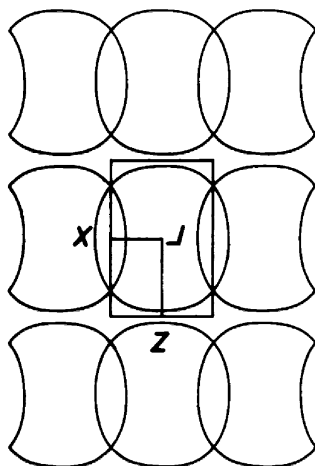


Fig. 1.7: Numerically obtained Fermi surface associated with the half-filled band of Fig. 1.6. The box in the center denotes the Brillouin zone. [12]

band is half-occupied. Then the Fermi surface consists of overlapped deformed circles (Fig. 1.7), which results in the combination of an oval-shaped quasi-two-dimensional cylinder and a pair of open quasi-one-dimensional sheets. The predicted Fermi surface was successfully confirmed by the Shubnikov - de Haas and de Haas - van Alphen experiments, but only in the κ -(ET) $_2$ Cl and κ -(ET) $_2$ NCS materials. In particular, measurements detect two orbital frequencies, α due to the closed hole pockets and β due to the magnetic breakdown encircling the entire Fermi surface [14], the values of which are in a good quantitative agreement with the theoretical predictions. The κ -(ET) $_2$ Br material exhibits, however, some slight aberrations from this simple picture. The detection and value of the high frequency β orbital agrees with the theoretical prediction, while the two distinctive low-frequency orbitals appear only after the pressure of about 5 kbar is applied at low temperatures [15]. Note that this pressure corresponds well to the one at which the superconducting state is completely suppressed. However, neither of the two obtained frequencies agrees with the expected frequency value for α hole pocket orbital. This discrepancy can be explained if results of the X-ray measurements made by Nogami *et al.* [16] are taken into consideration. It was reported that the superlattice structural transition, assigned to the longitudinal displacement or deformation of anion layer chains, appears below 200 K, which leads to the halving of the Brillouin zone in the k_c direction. As the result, the new bone-like, star-like and pocket-like Fermi surface structures appear, the areas of which correspond to the frequencies obtained by the magnetotransport measurements [15].

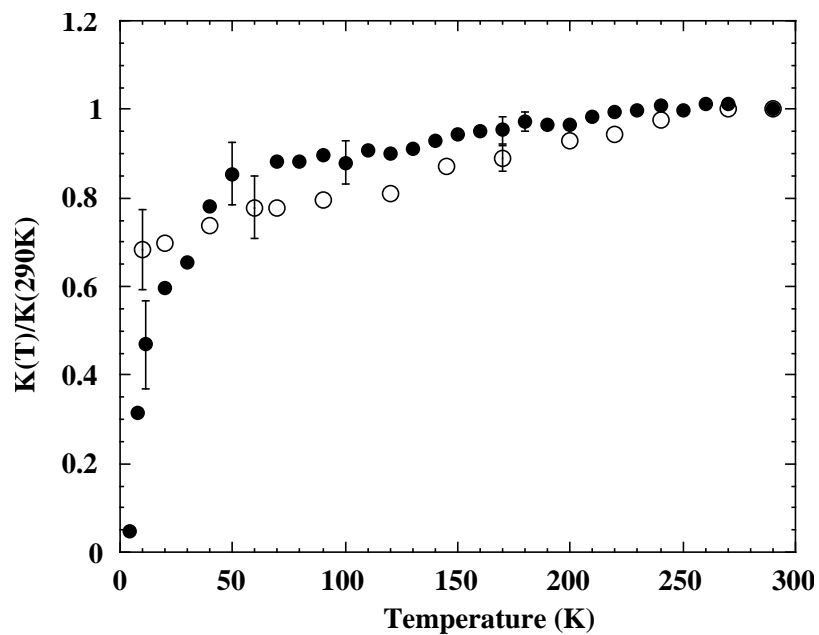


Fig. 1.8: Temperature dependence of the Knight shift normalized by its room temperature value for κ -(ET) $_2$ Br at 1 bar (\bullet) and 4 bar (\circ). [17]

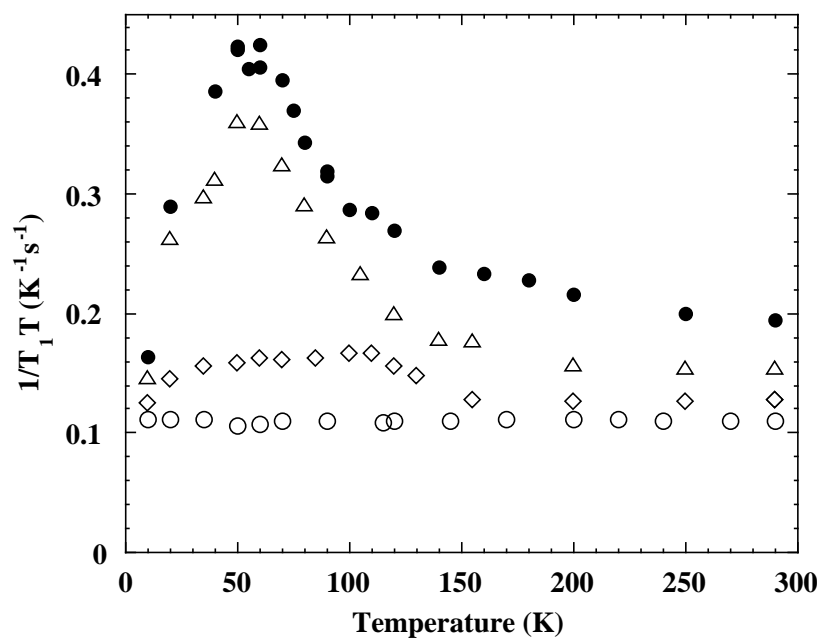


Fig. 1.9: $1/T_1T$ versus temperature for κ -(ET) $_2$ Br at different pressures: 1 bar (\bullet), 1.5 kbar (Δ), 3 kbar (\diamond), and 4 kbar (\circ). [17]

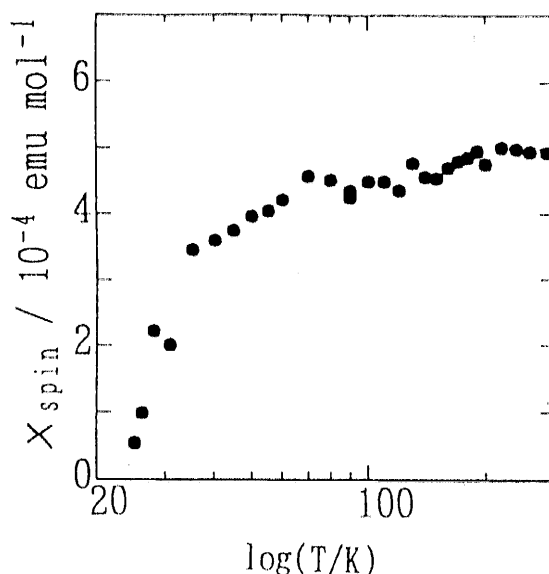


Fig. 1.10: Temperature dependence of the ESR molar magnetic susceptibility for κ -ET $_2$ Cl. [19]

Despite of the high conductivity, normal state above the SC ground state [in κ -(ET) $_2$ Br and κ -(ET) $_2$ NCS] shows several properties at the atmospheric pressure that are distinct from conventional metals, supporting the importance of electron correlations. In particular, the Knight shift decreases significantly below approximately 50 K, suggesting a suppression of the density of the states – that is, the appearance of a pseudogap near the Fermi energy (Fig. 1.8) [17]. A broad dip in the electronic density of the states around the Fermi energy was also observed by the scanning tunneling microscopy (STM) measurements below about the same temperature [18]. Finally, the spin-lattice relaxation rate $1/T_1$ does not follow the Korringa law, valid for most normal metals, which states that $1/T_1T$ is independent of the temperature. Instead, there is a peak in $1/T_1T$ at about 50 K, which suggests the presence of the short-range AF correlations (Fig. 1.9) [17]. This peak disappears under the external pressure concomitantly with the suppression of superconductivity and the disappearance of the drop in the Knight shift behavior (Fig. 1.8).

A useful estimate of electron correlations can be obtained by using electron susceptibility data. The molar magnetic susceptibility was measured using the electronic spin resonance technique in the κ -(ET) $_2$ Cl material by Kubota *et al.* (Fig. 1.10) [19]. If the density of the states at the Fermi energy $N(E_F) = 0.91 \text{ eV}^{-1}$ [12] in these two materials is taken into consid-

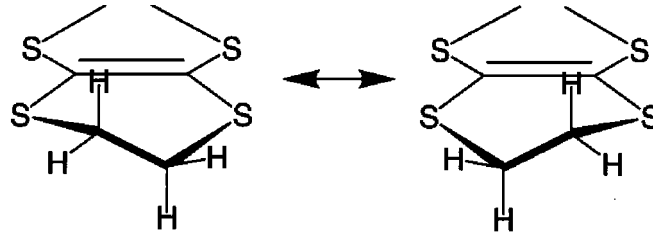


Fig. 1.11: Two possible conformations of the ethylene group. [21]

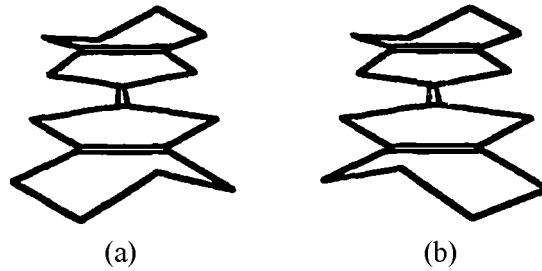


Fig. 1.12: Two possible arrangements of the outer C-C bonds: (a) eclipsed and (b) staggered. [12]

eration, it is obvious that the susceptibility is enhanced. Using the Hubbard susceptibility expression one can estimate the Coulomb interaction value to about $U \approx 1.04$ eV for both materials [20]. Note that a similar value is also reported by the authors of Ref. 17. The large interaction, comparable to the bandwidth $U \approx W$, is consistent with other experimental indications of the strong electron correlations. On the other hand, since the same conclusion is obtained for both the antiferromagnetic κ -(ET) $_2$ Cl and the superconducting κ -(ET) $_2$ Br materials, the electron correlations in the normal state cannot explain their difference of the ground state.

1.2.3 Relaxation effects

Another important normal state feature that requires special attention is an order-disorder transition that bears glassy features, first reported by the ac specific heat measurements [21]. The transition was ascribed to the gradual freezing down of the remaining motion of the ethylene groups of the BEDT-TTF molecules, which are thermally activated at high temperatures between the two possible conformations (Fig. 1.11), as reported by the X-ray diffraction measurements [12]. That is, the relative orientation of the outer C-C bonds can be either eclipsed or staggered (Fig. 1.12). Upon lowering the temperature, the former and the latter are adopted for κ -(ET) $_2$ Br

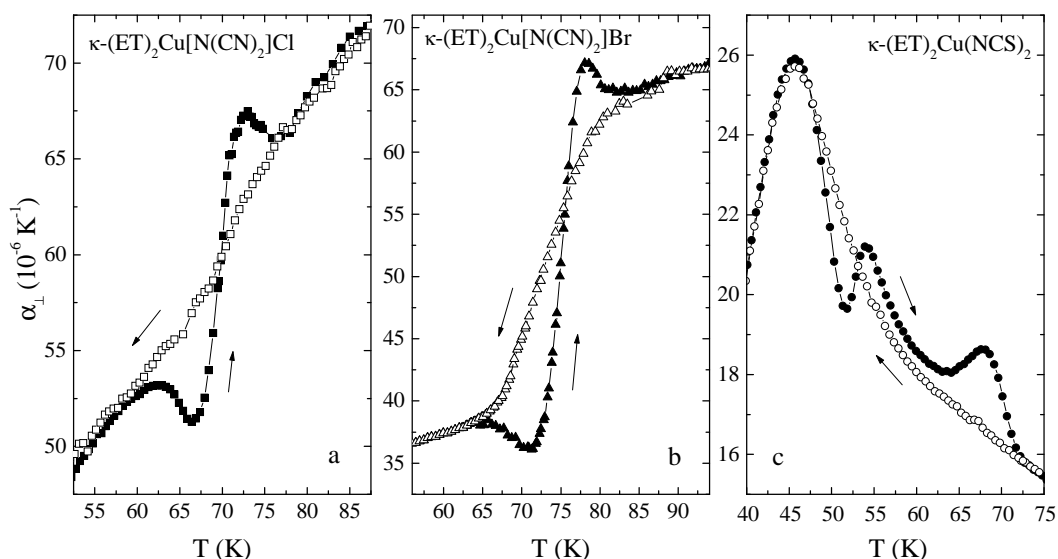


Fig. 1.13: Coefficient of the thermal expansion perpendicular to the planes, α_{\perp} , versus T close to the glass transition for (a) κ -(ET) $_2$ Cl (b) κ -(ET) $_2$ Br, and (c) κ -(ET) $_2$ NCS. Solid and open symbols denote the heating and cooling curves, respectively. No cooling-rate dependence of behavior was observed for rates between -0.02 K/min and -5 K/min. [22]

and κ -(ET) $_2$ NCS, respectively. The X-ray measurements also report that at 127 K the ethylene groups are already ordered in the whole bulk, however the authors of Ref. 21 argued that the sensitivity of the calorimetry is much higher than the diffractometry concerning the disorder and that the disorder of the ethylene groups at this temperature could still exist. The existence of the glass transition was confirmed by the measurements of the coefficient of the thermal expansion [22], which determined transition regions and transition temperatures more precisely. The transition region is situated between 60 and 80 K in the κ -(ET) $_2$ Cl [Fig. 1.13(a)], between 65 and 85 K in the κ -(ET) $_2$ Br [Fig. 1.13(b)], and between 45 and 75 K in the κ -(ET) $_2$ NCS material [Fig. 1.13(c)]. Transition temperatures were identified at $T_G \approx 70$ K in the κ -(ET) $_2$ Cl, at $T_G \approx 75$ K in the κ -(ET) $_2$ Br, or at $T_{G1} \approx 70$ K and $T_{G2} \approx 53$ K in the κ -(ET) $_2$ NCS material.

An important question arises whether the order-disorder transition in the κ -(ET) $_2$ Br material is somehow connected to the reported superlattice structural transition below 200 K, which doubles the lattice parameter along c -axis [16]. The authors argued that the transition is due to the longitudinal displacement of chains in the anion layer. The NMR studies showed that the motion of ethylene groups starts freezing below 200 K and that an incom-

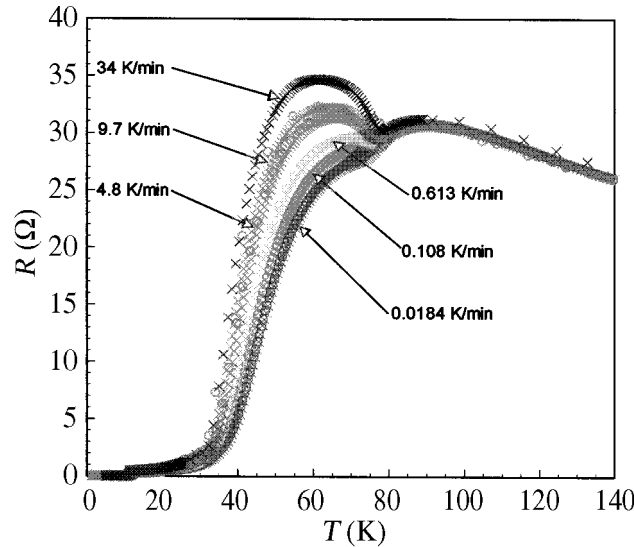


Fig. 1.14: The resistivity as a function of the temperature for the κ -(ET) $_2$ Br sample cooled at different cooling rates. [24]

mensurate modulation of the electron density is observed below that temperature [17]. In order to elucidate relaxation transition, Tanatar *et al.* [23] took the resistance measurements of the structural relaxation kinetics; That is, the isothermal time dependent resistivity and temperature dependent resistivity as a function of the thermal history were measured. They argued that the competition between the interaction of ethylenes with anions and the energy difference between two molecular conformations determine whether a superstructure or ordered state is formed. In connection to the NMR results they concluded that between 100 K and 200 K the incommensurate superstructure of the ethylene groups exists, the presence of which could also be connected to the reported superlattice transition. Further, they report that a coexistence of two phases, the ethylene groups superstructure and the ethylene groups ordering, exists between 60 K and 100 K, with the temperature of 80 K as the border between the two phases. In accordance with other experiments, (re)ordering bears glassy properties in this temperature region, while below 60 K the ordered phase finally stabilizes.

Anyhow, the passage through the region of the glass transition appears to play a crucial role regarding the level of the residual intrinsic disorder at low temperatures for all three materials alike. Rapid cooling rates are reflected in the smaller resistivity ratio between T_G and T_C for κ -(ET) $_2$ Br and κ -(ET) $_2$ NCS materials and larger resistivity humps centered at about 60 K (Fig. 1.14) [4, 25]. The residual disorder might also be connected to

the anomalous changes in the thermal expansion behavior at about 80 K, in particular with a large and abrupt change and a small hysteresis in the behavior of the linear expansion of coefficients along all three principle axes [26, 27]. That is, in κ -(ET)₂Br the linear expansion of a parameter changes the sign, while the linear expansions of b and c show rapid drop of the value.

The sample dependence and relaxation effects were also observed in the magnetization measurement results for κ -(ET)₂Br [28]. Samples of one synthesis show the second peak in the magnetization *versus* field ($M - H$) curve, corresponding to the dimensional crossover in the vortex system, in contrast to crystals of another synthesis that show only one. The observed anomalous cooling rate dependence of the $M - H$ curve was attributed to the change in the resistivity curves and the remnant disorder in the sample.

1.3 Insulating spin density wave state in κ -(BEDT-TTF)₂Cu[N(CN)₂]Cl

The first magnetization measurements performed by Welp *et al.* [29] claimed an antiferromagnetic transition at 45 K and a weak ferromagnetic state below 22 K. Later, the results of the NMR measurements showed a large enhancement of the spin-lattice relaxation rate below 50 K and a sharp peak at 27 K [30]. The former was interpreted to be due to the antiferromagnetic spin fluctuations, and the latter as a sign of an antiferromagnetic phase transition. Indeed, the established order is commensurate with the underlying lattice and possesses a rather large moment of (0.4–1.0) μ_B /dimer, which is much larger than the value of 0.08 μ_B /molecule observed in the case of the spin density wave in (TMTSF)₂PF₆ formed by itinerant spins [31]. In addition, magnetization measurements by former authors [30] showed that the weak ferromagnetism appears below 23 K due to the canting of spins. As in this temperature region a finite energy gap is already opened in the charge degrees of freedom, Miyagawa *et al.* [30] suggested that the magnetic ordering of localized spins driven by the electron-electron correlations was in the origin of the observed phase transition. Kino *et al.* [32] proposed a theoretical model in which the AF ordering with the large magnetic moment and a simultaneous metal-to-insulator phase transition is predicted as the effect of a strong enough on-site Coulomb interaction within the Hartree-Fock approximation.

Magnetic anisotropy measurements showed that an antiferromagnetic transition with a concomitant canted antiferromagnetic state is established at 22 K [6]. The easy axis was confirmed to be along the crystallographic b -axis

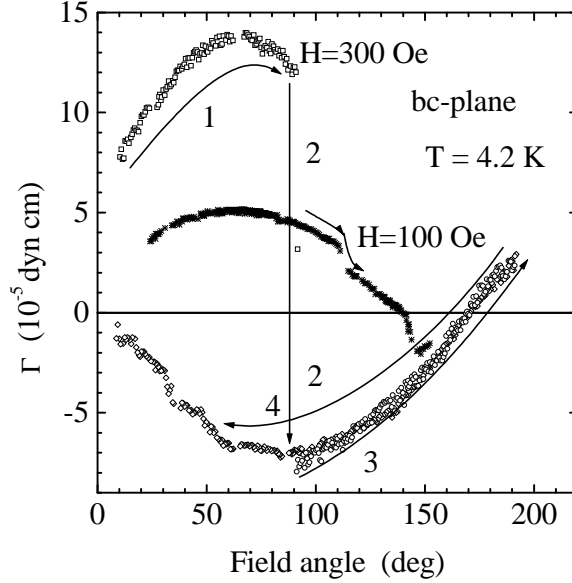


Fig. 1.15: Torque *versus* angle in the bc -plane at 4.2 K for two field values. Arrows (1,2,3) and (4) indicate the increasing and decreasing fields ($H = 300$ Oe), respectively. [6]

with the AF spins canted by angle 6×10^{-2} degrees from it. It was argued that the observed features might be well described if the Dzyaloshinsky-Moriya interaction is taken into account [33]. Magnetic field reversal of the ferromagnetic magnetization also indicated the existence of a domain structure (Fig. 1.15) [6]. It was concluded that the low-temperature state is the weak ferromagnetic state divided in domains with the equivalent spin configurations.

1.4 Superconducting state in κ -(BEDT-TTF) $_2\text{Cu}[\text{N}(\text{CN})_2]\text{Br}$ and κ -(BEDT-TTF) $_2\text{Cu}(\text{NCS})_2$

The superconducting ground state in κ -(ET) $_2\text{Br}$ and κ -(ET) $_2\text{NCS}$ materials is established below $T_C \approx 11.5$ K and $T_C \approx 9.5$ K, respectively [35]. Reported penetration depths, in accordance to the structure of the materials, are strongly anisotropic, that is $\lambda_{\parallel} = 0.5 - 2 \mu\text{m}$ [36, 37, 38] and $\lambda_{\perp} = 40 - 300 \mu\text{m}$ [36, 39, 40, 41]. Coherence length values are much smaller, $\xi_{\parallel} = 20 - 60 \text{ \AA}$ and $\xi_{\perp} = 3 - 7 \text{ \AA}$, which gives $\kappa_{\parallel} \approx 300$ and $\kappa_{\perp} \approx 2 \times 10^5$ for the Ginzburg-Landau parameters. Hagel *et al.* [34] have also determined

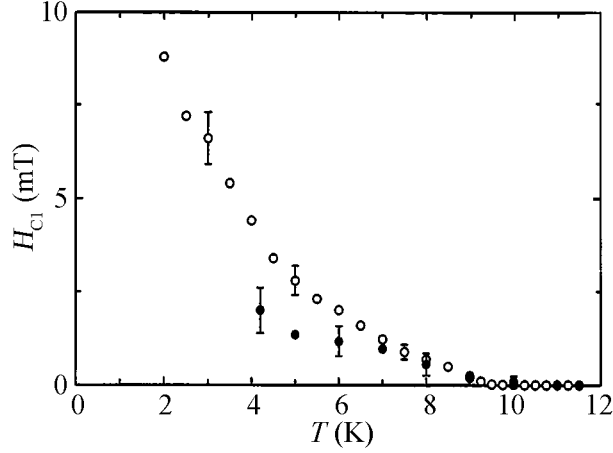


Fig. 1.16: Lower critical field H_{C1} for κ -(ET) $_2$ Br for the field perpendicular to isotropic planes determined by two different methods. [34]

critical magnetic fields for the κ -(ET) $_2$ Br material. The lower critical field, below which the Meissner state is established, is presented in Fig. 1.16.

The presence of the significant electron correlations strongly favors the possibility of an unconventional SC. Results in favor of a d -wave order parameter have been obtained by different experimental techniques. The ^{13}C NMR measurements showed that the spin-lattice relaxation rate follows a T^3 dependence at very low temperatures. This result, together with the Knight shift experiment, provides evidence for spin-singlet pairing with nodes in the gap [42]. The low-temperature specific heat [43], as well as the thermal conductivity [44], also showed a power-law behavior $C_s(T) \propto T^2$ and $\kappa(T) \propto T$, respectively. Further, the penetration depth $\lambda(T)$, measured by microwave cavity perturbation [38], tunnel diode oscillation [39], muon-spin relaxation [45], and ac susceptibility [46], also displayed the power-law behavior, usually in the form of a T and/or a T^2 behavior for $\lambda(T)$ at low temperatures.

The possibility of the unconventional pairing was also predicted by theoretical calculations. Louati *et al.* [47] have proposed that the nesting between the pair of the open quasi-one-dimensional sheets is responsible for the strong antiferromagnetic correlations. The calculation quantitatively reproduces the unusual behavior of $1/T_1T$ and Knight shift in the normal state, and it also suggests an anisotropic mechanism for the SC pairing in a form of the antiferromagnetic fluctuations, which leads to the formation of the d -wave pairing. The nesting mechanism opens an AF gap in the open quasi-one-dimensional sheets, so the superconductivity is attributed to the oval-shaped quasi-two-dimensional cylinders.

Further, the calculation showed that the increase of the t_1/t_2 ratio, where t_1 and t_2 represent transfer integrals between the BEDT-TTF dimers in two different in-plane crystallographic directions, decreases the value of the superconducting coupling constant. Concomitantly both Fermi surfaces deform, the nesting is no longer perfect and the antiferromagnetic correlation weakens. Therefore, if one connects the increase of the t_1/t_2 ratio, to the increase of the external pressure, it is possible to explain the disappearance of superconductivity, as well as the disappearance of the peak in $1/T_1T$. Since the t_1/t_2 ratio is related to W/U_{eff} , this explains the relation between the pressure and the U_{eff}/W ratio implicitly given in the κ -(ET) $_2X$ phase diagram (Fig. 1.1).

Further, recent angle-resolved measurements of the SC gap structure using STM [48] and the thermal conductivity [49] both clearly showed the fourfold symmetry in the angular variation, characteristic of the d -wave superconducting gap. Former also report the maximum value of the order parameter to be $\Delta(0) = 3.4 k_B T_C$, what is substantially more than expected for the s -wave pairing. However, both measurements have revealed that the nodes are directed along directions rotated by 45° relative to the in-plane crystallographic axes, indicating the $d_{x^2-y^2}$ -wave superconductivity. Such a nodal structure indicates that both Fermi surfaces should participate in the SC pairing, what is in contrast with theoretical predictions [47].

In contrast to the presented indications of the superconducting order parameter with nodes, some other penetration depth studies using the cavity perturbation technique [36], the muon-spin relaxation [50], and the dc magnetization [51], as well as the most recent specific heat measurements [52, 53], led to results favoring a conventional s -wave order parameter. In particular, a strong-coupling s -wave order parameter was claimed to be observed in the latter experiments. Unlike the previous specific heat measurements [43], in which the lattice specific heat was measured in the deuterated κ -(ET) $_2\text{Br}$ material, the ground state of which is the AF state, in the latter experiments the lattice specific heat was measured in the normal state produced by fields higher than $H_{C2} \approx 10$ T. However, authors of Ref. 43 argue that in case of huge fields some additional terms due to possible paramagnetic localized moments or impurities can appear and obscure the reliability of the lattice specific heat, especially at temperatures below 1 K.

The question arises as to what the source of the conflicting results is and how this discrepancy could be resolved. As far as the experimental determination of the penetration depth in the mixed state is concerned [50, 51], fields as low as 70–300 Oe might present a serious problem, as pointed out by Lee *et al.* [37]. Above these fields the rigid three-dimensional vortex lattice is replaced by the quasi-independent two-dimensional lattices, and the

result for the penetration depth might be influenced by the complex vortex dynamics. On the other hand, additional complications might occur due to an order-disorder transition, described in Sec. 1.2.3. And finally, attention should be given to the difference in properties depending on the sample, that is, the synthesis of the sample.

2 Theory of unconventional superconductivity

In this chapter the extension of the most successful theory of superconductivity up to date – the BCS theory of superconductivity – will be presented. After the original theory was first published in 1957 by Bardeen, Cooper and Schrieffer [54], it instantly became one of the most successful microscopic theories in the physics of the condensed matter. However, it was the discovery of new superconducting materials, heavy fermion superconductors in 1979, organic material superconductors in 1980, and high-temperature superconducting cuprates in 1986, that threw shadow on its ultimate success. Nevertheless, further theoretical developments proved that the basic principle of the original BCS theory, the formation of the superconducting Cooper pair, is still valid, and that the theory should only be extended by assuming the possibility of an anisotropic wave function of the Cooper pair.

This assumption paved the way to immense number of different wave functions and physical properties resulting from them. However, all new phenomena can be qualitatively classified in only a few distinct situations, depending on the dimensionality of the Fermi surface and the topology of the superconducting energy gap. The topic is still too general and too comprehensive for primarily experimental thesis on superconductivity. Therefore, for the matter of simplicity only the singlet spin Cooper pairs will be considered in particular details, while the extensive literature, on which this presentation is based [55, 56, 57], provides a more detailed insight into all possibilities. Further, we limit analysis for the case of a three-dimensional Fermi surface, while in the case of a two-dimensional Fermi surface, a special care has to be exercised, as for example in Sec. 6.3.

2.1 Cooper pair

The basic idea that lays behind the BCS theory is the assertion made by Cooper in 1956 [58]; That is, the Fermi sea of electrons is unstable against

the formation of at least one bound pair, regardless of how weak the interaction is, so long as it is attractive. The question arises as to what kind of interaction could be responsible for the attractive interaction between two electrons. It turns out that there are many mechanisms, which could lead to such interaction, as far as an appropriate mediator of the interaction between two electrons is included. Even before the BCS theory was published, it was known that if electron-lattice interaction is taken into account, an attractive term in the interaction of electrons appears. Thus, a part of interaction between two electrons, mediated by vibrations of the crystal lattice (so-called *phonons*) gives an almost isotropic attractive interaction, leading in the original BCS theory to the formation of the Cooper pairs with a zero angular momentum (*s-wave*). Later it turned out that other mediators, like ferromagnetic (so-called *paramagnons*) and antiferromagnetic (so-called *antiparamagnons*) spin fluctuations also give an attractive interaction, which is however essentially anisotropic and leads to the formation of the Cooper pairs with a non-zero angular momentum (*p-wave*, *d-wave* ...). The anisotropic pairing of the Cooper pair is (at least in the experimental community) usually referred to as the *unconventional superconductivity*.

In order to demonstrate the formation of the Cooper pair, the generalized approach of the Cooper's originally simple model will be presented. Two electrons are added to Fermi sea of electrons, very near to Fermi surface, with the stipulation that the extra electrons interact with each other, but not with those of the sea, except via the exclusion principle. Thus, we want to solve the two-particle wave function $\psi(\mathbf{r})$, where \mathbf{r} is relative position vector of two electrons, using the Schrödinger equation. In the momentum (\mathbf{k}) representation we obtain the following expression

$$\frac{\hbar^2 k^2}{m} g(\mathbf{k}) + \int \frac{d^3 k'}{(2\pi)^3} V(\mathbf{k} - \mathbf{k}') g(\mathbf{k}') = \left(\Delta + \frac{\hbar^2 k_F^2}{m} \right) g(\mathbf{k}), \quad (2.1)$$

where $g(\mathbf{k})$ is the two-particle wave function in the momentum representation, $V(\mathbf{k} - \mathbf{k}')$ the potential between two electrons, m electron mass, k_F Fermi wave vector and Δ bounding energy. The interaction potential is a function of the momentum direction and can be expanded using spherical harmonics $Y_{lm}(\hat{k})$

$$V(\mathbf{k} - \mathbf{k}') = \sum_{l=0}^{\infty} V_l(k, k') \sum_{m=-l}^l Y_{lm}(\hat{k}) Y_{lm}^*(\hat{k}'). \quad (2.2)$$

In the *weak coupling limit* the potential is assumed to be non-zero, but constant and attractive only within a thin layer over the Fermi surface

$\varepsilon_l \ll \varepsilon_F = \hbar^2 k^2 / 2m$, where ε_F represents Fermi energy. That is,

$$V_l(\mathbf{k} - \mathbf{k}') = -V_l, \text{ for } \varepsilon_F < \frac{\hbar^2 k^2}{2m}, \frac{\hbar^2 k'^2}{2m} < \varepsilon_F + \varepsilon_l. \quad (2.3)$$

Using Eq. (2.3) and replacing the summation over wave vector with the integration over energy relative to Fermi energy $\xi = \hbar^2 k_F^2 / 2m - \varepsilon_F$, we finally obtain

$$\left\{ \frac{\hbar^2}{m} (k^2 - k_F^2) - \Delta \right\} g(\mathbf{k}) - N_0 \int_0^{\varepsilon_l} d\xi' \int \frac{d\Omega'}{4\pi} \sum_{l=0}^{\infty} V_l \sum_{m=-l}^l Y_{lm}(\hat{k}) Y_{lm}^*(\hat{k}') g(\mathbf{k}') = 0, \quad (2.4)$$

where N_0 represents the density of the states at the Fermi level. Each value of the orbital angular momentum l corresponds to a specific eigenfunction $g_l(\mathbf{k})$ with eigenenergy Δ_l . Therefore, by expanding $g(\mathbf{k})$ using spherical harmonics $Y_{lm}(\hat{k})$

$$g(\mathbf{k}') = g_{l'}(\mathbf{k}') = \sum_{m'=-l'}^{l'} a_{l'm'}(k') Y_{l'm'}(\hat{k}'), \quad (2.5)$$

where $a_{l'm'}(k')$ are expansion coefficients, and using the orthonormality property of spherical functions we finally obtain

$$\left\{ \frac{\hbar^2}{m} (k^2 - k_F^2) - \Delta_l \right\} g_l(\mathbf{k}) - N_0 V_l \int_0^{\varepsilon_l} d\xi' g_l(\mathbf{k}') = 0, \\ g_l(\mathbf{k}) = \frac{N_0 V_l}{2\xi - \Delta_l} \int_0^{\varepsilon_l} d\xi' g_l(\mathbf{k}'). \quad (2.6)$$

Integrating both sides of Eq. (2.6) over ξ in range $(0, \varepsilon_l)$, given that the interaction is sufficiently weak, $N_0 V_l \ll 1$, gives

$$\Delta_l = \frac{2\varepsilon_l}{1 - e^{\frac{2\varepsilon_l}{N_0 V_l}}} \approx -2\varepsilon_l e^{\frac{2\varepsilon_l}{N_0 V_l}}. \quad (2.7)$$

Thus a bound state, the energy of which is a function of the orbital angular momentum, occurs in the case of an arbitrarily weak interaction between two electrons.

The Cooper pairs are composed of fermions with spin $S = \frac{1}{2}$, so the pair wave function should describe a boson with a total spin of $S = 0$ (singlet) or $S = 1$ (triplet). On the other hand, the whole wave function should be

antisymmetric with respect to the exchange of two particles. In the case of the singlet state, the spin part of the wave function can be written as $(\alpha_1\beta_2 - \beta_1\alpha_2)$, where indices denote particle numbers, while α and β refer to the “up” and “down” spin states, respectively. The spin part must then be combined with the spatial part of the wave function to give the total wave function of the Cooper pair

$$\psi_l(\mathbf{k}) = (\alpha_1\beta_2 - \beta_1\alpha_2)g_l(\mathbf{k}) = (\alpha_1\beta_2 - \beta_1\alpha_2) \sum_{m=-l}^l a_{lm}(k)Y_{lm}(\hat{k}). \quad (2.8)$$

Note that the condition for the antisymmetry of the whole function requires that the spatial part is symmetric; That is, l must take even values $l = 0, 2, 4, \dots$

On the other hand, in the case of the triplet state three distinct spin parts of the function can be written $(\alpha_1\alpha_2)$, $(\alpha_1\beta_2 + \beta_1\alpha_2)$, and $(\beta_1\beta_2)$ with the z -spin projection of $S_z = 1$, $S_z = 0$, and $S_z = -1$, respectively. The total wave function of the pair is

$$\begin{aligned} \psi_l(\mathbf{k}) &= (\alpha_1\alpha_2)g_{l,1}(\mathbf{k}) + (\alpha_1\beta_2 + \beta_1\alpha_2)g_{l,2}(\mathbf{k}) + (\beta_1\beta_2)g_{l,3}(\mathbf{k}), \\ &\text{with } g_{l,d} = \sum_{m=-l}^l a_{lm,d}(k)Y_{lm}(\hat{k}). \end{aligned} \quad (2.9)$$

Note that the condition for the antisymmetry of the whole function requires that the spatial part is antisymmetric; That is l must take odd values $l = 1, 3, 5, \dots$

2.2 Symmetry considerations

It was shown in the previous section that the Cooper pair wave function can be expanded using the spherical harmonics. The condition for the antisymmetry of the whole function, which imposed that the space part of the wave function is either symmetrical or antisymmetrical, significantly reduced the number of acceptable spherical harmonics by halving the number of acceptable angular momentum values l . Moreover, when the superconducting state in crystals is considered, the number of possible allowed spherical harmonics is further reduced by the requirement that the wave function symmetry should be in accordance with the crystal symmetry. Taking into consideration that the presence of the interaction can reduce the symmetry of the wave function, we conclude that the wave function symmetry should be equal or lower than the crystal symmetry.

Mathematically speaking, we can form a group of $\alpha, \beta = 1 \dots d$ linear combinations of the spherical harmonics, ψ_α , that are transformed into themselves by any symmetry operator g from the crystals symmetry group G , that is

$$\psi_\alpha(g\hat{k}) = \psi_\alpha(\hat{k}') = \sum_{\beta=1}^d c_{\alpha,\beta} \psi_\beta(\hat{k}),$$

where $c_{\alpha,\beta}$ are transformation coefficients. One says that such a group of d functions forms the basis of an irreducible representation Γ of a certain spatial symmetry group G . For example, in an isotropic system, which is invariant under all spatial rotations, the irreducible representations are labeled by the value of the orbital angular momentum l , and the set of the $2l + 1$ spherical harmonics with the given orbital momentum l forms the basis of the irreducible representation. In the case of the triplet state of the Cooper pair also the spin-orbit coupling should be considered. Only in the case of the negligible spin-orbit coupling, the states remain degenerate with respect to the rotation of spin vectors, while for the strong spin-orbit coupling spin becomes a “bad” quantum number.

After the appropriate irreducible representation Γ with $\alpha = 1 \dots d$ elements is determined, we can write the wave function of the singlet Cooper pair as a linear combination of them

$$g(\mathbf{k}) = \sum_{\alpha=1}^d \eta_\alpha \psi_\alpha(\hat{k}). \quad (2.10)$$

The set of complex coefficients η_α is called the *order parameter*. Superconducting states with either a one-component order parameter $\eta = |\eta|e^{i\varphi}$ or multi-component order parameters are plausible.

In addition to the point symmetry operations, the symmetry group \mathbf{G} of the normal state also contains the operation of time reversal R and gauge transformations $U(1)$:

$$\mathbf{G} = U(1) \times R \times G.$$

The transition to a superconducting state causes phase coherence, i.e., states with different phases φ of the order parameter $|\eta|e^{i\varphi}$ become distinguishable, which is usually described as the spontaneous breaking of gauge symmetry $U(1)$. Other types of symmetry breaking of the symmetry group \mathbf{G} may also occur as a result of the transition in a particular superconducting state. Then the point symmetry of the superconducting state does not have full point symmetry of the crystal lattice and one usually refers to such cases (at least in the theoretical community) as to the *unconventional superconductivity*. Mathematically speaking, the conventional superconductivity corresponds to the identity representation, denoted as A_{1g} or A_g in Tables 2.1,

d	Γ	$\psi_\alpha(\hat{k})$
1	A_{1g}	$az^2 + b(x^2 + y^2)$
1	A_{2g}	$xy(x^2 - y^2)$
1	B_{1g}	$x^2 - y^2$
1	B_{2g}	xy
2	E_g	xz, yz

Table 2.1: Basis functions $\psi_\alpha(\hat{k})$ of even ($S = 0$) representations of group D_{4h} (tetragonal crystals). Γ denotes representation name and d its dimensionality.

d	Γ	$\psi_\alpha(\hat{k})$
1	A_{1g}	$ax^2 + by^2 + cz^2$
1	A_{2g}	xy
1	B_{1g}	xz
1	B_{2g}	yz

Table 2.2: Basis functions $\psi_\alpha(\hat{k})$ of even ($S = 0$) representations of group D_{2h} (orthorhombic crystals). Γ denotes representation name and d its dimensionality.

2.2 and 2.3, while all other representations correspond to the unconventional superconductivity. Note that this is the second possible, more theoretical definition of the term “unconventional”, apart from the one we have already presented in Sec. 2.1. However, this theoretical definition is rather rarely used, so in the rest of this thesis we shall stick to the experimental definition of the unconventional superconductivity as to the superconducting state in which the pairing is anisotropic (non- s -wave pairing).

The accumulated data concerning the low-temperature behavior of high-

d	Γ	$\psi_\alpha(\hat{k})$
1	A_g	$ax^2 + by^2 + cz^2 + dxy$
1	B_g	$axz + byz$

Table 2.3: Basis functions $\psi_\alpha(\hat{k})$ of even ($S = 0$) representations of group C_{2h} (monoclinic crystals). Γ denotes representation name and d its dimensionality.

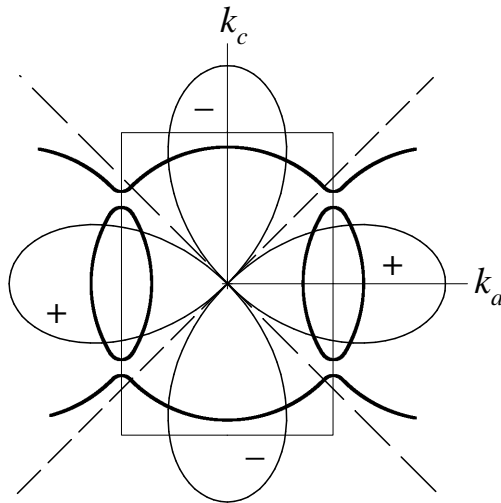


Fig. 2.1: Order parameter $d_{x^2-y^2}$ for κ -(ET) $_2X$ materials. Thick lines represent the Fermi surface, lines with a medium thickness superconducting gap and thin lines the Brillouin zone and crystallographic axes. Dashed lines represent node directions in the superconducting gap.

temperature superconducting cuprates suggests the formation of the $d_{x^2-y^2}$ pairing. Since the crystal structure of most cuprates is tetragonal (Table 2.1), this means that the pairing is in theoretical terms unconventional (B_{1g}). It is however remarkable that the $d_{x^2-y^2}$ pairing is absolutely conventional for the remaining cuprates with an orthorhombic crystal structure (Table 2.2).

Finally, for both superconducting κ -(ET) $_2X$ salts, κ -(ET) $_2$ Br, which has an orthorhombic crystal structure (Table 2.2), and κ -(ET) $_2$ NCS, which has a monoclinic crystal structure (Table 2.3), the $d_{x^2-y^2}$ pairing is in theoretical terms conventional. For the illustration, the relation between Fermi surface and gap structure according to angle-resolved experiments [48, 49] is shown in Fig. 2.1.

2.3 Energy of elementary excitations

In Sec. 2.1 the creation of the superconducting pair was sketched using the two-body method. In order to study other interesting properties, especially the elementary excitations in the superconductor, the many-body approach should be applied. For this purpose the second quantization method is most appropriate. Please note that for the reason of simplicity, only singlet Cooper pairs will be examined in this section.

A special, BCS Hamiltonian has to be constructed in order to account

for the attraction potential between electrons in the Cooper pairs

$$H = \sum_{\mathbf{k}\sigma} \xi_{\mathbf{k}} c_{\mathbf{k}\sigma}^+ c_{\mathbf{k}\sigma} + \sum_{\mathbf{k}\mathbf{k}'} V_{\mathbf{k}\mathbf{k}'} c_{\mathbf{k}\uparrow}^+ c_{-\mathbf{k}\downarrow}^+ c_{-\mathbf{k}'\downarrow} c_{\mathbf{k}'\uparrow}. \quad (2.11)$$

Here, c^+ and c are creation and annihilation operators of electrons, respectively, σ refer to any spin state, while \uparrow and \downarrow refer to the “up” and “down” spin states, respectively. The instability of the electron gas to this Hamiltonian against the formation of the Cooper pairs can be taken into account by expressing the wave function in the form of the following product

$$|\Psi\rangle = \prod_{\mathbf{k}} (u_{\mathbf{k}} + v_{\mathbf{k}} c_{\mathbf{k}\uparrow}^+ c_{-\mathbf{k}\downarrow}^+) |0\rangle, \quad (2.12)$$

where $v_{\mathbf{k}}$ and $u_{\mathbf{k}}$ are probabilities that the $(\mathbf{k} \uparrow, -\mathbf{k} \downarrow)$ state is occupied or vacant, respectively, while $|0\rangle$ represents the vacuum state. Obviously,

$$v_{\mathbf{k}}^2 + u_{\mathbf{k}}^2 = 1. \quad (2.13)$$

The importance of the above expression of the ground state is that it is the superposition of states with different numbers of the Cooper pairs. The consequence of this fundamental fact is non-vanishing values of so-called anomalous averages

$$b_{\mathbf{k}} = \begin{cases} \langle \Psi | c_{-\mathbf{k}\downarrow} c_{\mathbf{k}\uparrow} | \Psi \rangle, & T = 0, \\ \langle c_{-\mathbf{k}\downarrow} c_{\mathbf{k}\uparrow} \rangle, & T > 0. \end{cases} \quad (2.14)$$

Note that the function $b_{\mathbf{k}}$ determines the expectation value of the Cooper pair, so it corresponds to the Cooper pair wave function $g(\mathbf{k})$. Because of the large number of the particles involved, the fluctuations about $b_{\mathbf{k}}$ should be small, so it would be useful to express the corresponding product of operators formally as

$$c_{-\mathbf{k}\downarrow} c_{\mathbf{k}\uparrow} = b_{\mathbf{k}} + (c_{-\mathbf{k}\downarrow} c_{\mathbf{k}\uparrow} - b_{\mathbf{k}}) \quad (2.15)$$

and subsequently neglect the quantities which are bilinear in the presumably small fluctuation term in parentheses. This is so-called *mean-field* approach to the solution of the system. Using this approach, the BCS Hamiltonian is transformed into the form

$$H = \sum_{\mathbf{k}\sigma} \xi_{\mathbf{k}} c_{\mathbf{k}\sigma}^+ c_{\mathbf{k}\sigma} + \sum_{\mathbf{k}\mathbf{k}'} V_{\mathbf{k}\mathbf{k}'} (c_{\mathbf{k}\uparrow}^+ c_{-\mathbf{k}\downarrow}^+ b_{\mathbf{k}'} + b_{\mathbf{k}}^+ c_{-\mathbf{k}'\downarrow} c_{\mathbf{k}'\uparrow} - b_{\mathbf{k}}^+ b_{\mathbf{k}'}). \quad (2.16)$$

Further, if we use the definition of the mean-field potential

$$\Delta_{\mathbf{k}} = - \sum_{\mathbf{k}'} V_{\mathbf{k}\mathbf{k}'} b_{\mathbf{k}'} = - \sum_{\mathbf{k}'} V_{\mathbf{k}\mathbf{k}'} \langle c_{-\mathbf{k}'\downarrow} c_{\mathbf{k}'\uparrow} \rangle, \quad (2.17)$$

the Hamiltonian transforms to

$$H = \sum_{\mathbf{k}\sigma} \xi_{\mathbf{k}} c_{\mathbf{k}\sigma}^+ c_{\mathbf{k}\sigma} - \sum_{\mathbf{k}} (\Delta_{\mathbf{k}} c_{\mathbf{k}\uparrow}^+ c_{-\mathbf{k}\downarrow}^+ + \Delta_{\mathbf{k}}^+ c_{-\mathbf{k}\downarrow} c_{\mathbf{k}\uparrow} - \Delta_{\mathbf{k}} b_{\mathbf{k}}^+). \quad (2.18)$$

Note that $\Delta_{\mathbf{k}}$ has the symmetry as $g(\mathbf{k})$. For a zero mean-field potential $\Delta_{\mathbf{k}} = 0$, there is no superconductivity and the anomalous averages as well as the pair wave function must vanish $g(\mathbf{k}) = \langle c_{-\mathbf{k}\downarrow} c_{\mathbf{k}\uparrow} \rangle = 0$. Similarly, for a positive or a negative $\Delta_{\mathbf{k}}$, $g(\mathbf{k})$ is also positive or negative, respectively. Therefore, we can take that their space dependencies are identical to some proportionality factor Δ , that is,

$$\Delta_{\mathbf{k}} = \Delta g(\mathbf{k}). \quad (2.19)$$

In order to diagonalize the Hamiltonian, we have to perform the Bogoliubov transformation. This is done by defining the new Fermi operators $\gamma_{\mathbf{k}}^+$ according to equations

$$\begin{aligned} c_{\mathbf{k}\uparrow} &= u_{\mathbf{k}}^+ \gamma_{\mathbf{k}0} + v_{\mathbf{k}} \gamma_{\mathbf{k}1}^+, \\ c_{-\mathbf{k}\downarrow}^+ &= -v_{\mathbf{k}}^+ \gamma_{\mathbf{k}0} + u_{\mathbf{k}} \gamma_{\mathbf{k}1}^+. \end{aligned} \quad (2.20)$$

The Hamiltonian is diagonalized for the condition

$$\begin{aligned} 2\xi_{\mathbf{k}} u_{\mathbf{k}} v_{\mathbf{k}} + \Delta_{\mathbf{k}}^+ v_{\mathbf{k}}^2 - \Delta_{\mathbf{k}} u_{\mathbf{k}}^2 &= 0, \\ \text{i.e., } \frac{\Delta_{\mathbf{k}}^+ v_{\mathbf{k}}}{u_{\mathbf{k}}} &= \sqrt{\xi_{\mathbf{k}}^2 + |\Delta_{\mathbf{k}}|^2} - \xi_{\mathbf{k}}. \end{aligned} \quad (2.21)$$

Finally, the diagonalized Hamiltonian reads

$$H = \sum_{\mathbf{k}} (\xi_{\mathbf{k}} - E_{\mathbf{k}} + \Delta_{\mathbf{k}} b_{\mathbf{k}}^+) + \sum_{\mathbf{k}} E_{\mathbf{k}} (\gamma_{\mathbf{k}0}^+ \gamma_{\mathbf{k}0} + \gamma_{\mathbf{k}1}^+ \gamma_{\mathbf{k}1}), \quad (2.22)$$

where $\gamma_{\mathbf{k}}^+$ obviously represents the operator of creation of the elementary excitation with energy $E_{\mathbf{k}} = \sqrt{\xi_{\mathbf{k}}^2 + |\Delta_{\mathbf{k}}|^2}$. As anticipated, $\Delta_{\mathbf{k}}$ plays the role of an energy gap.

2.4 Phase transition temperature

In order to fulfill the self-consistency of our calculation, the solution for $\langle c_{-\mathbf{k}'\downarrow} c_{\mathbf{k}'\uparrow} \rangle$ must be inserted back to Eq. (2.17). If we rewrite $c_{\mathbf{k}}$ operators in terms of $\gamma_{\mathbf{k}}$ operators and drop combinations $\gamma_{\mathbf{k}0}^+ \gamma_{\mathbf{k}1}^+$, which do not contribute to averages, we find

$$\Delta_{\mathbf{k}} = - \sum_{\mathbf{k}'} V_{\mathbf{k}\mathbf{k}'} u_{\mathbf{k}'}^+ v_{\mathbf{k}'} \langle 1 - \gamma_{\mathbf{k}'0}^+ \gamma_{\mathbf{k}'0} + \gamma_{\mathbf{k}'1}^+ \gamma_{\mathbf{k}'1} \rangle. \quad (2.23)$$

Taking into account that $\langle \gamma_{\mathbf{k}'0}^+ \gamma_{\mathbf{k}'0} + \gamma_{\mathbf{k}'1}^+ \gamma_{\mathbf{k}'1} \rangle$ equals to two times the probability of excitation, we can write $1 - \langle \gamma_{\mathbf{k}'0}^+ \gamma_{\mathbf{k}'0} + \gamma_{\mathbf{k}'1}^+ \gamma_{\mathbf{k}'1} \rangle = 1 - 2f(E_{\mathbf{k}'})$, where $f(E) = (1 + e^{E/kT})^{-1}$ is the Fermi-Dirac distribution. Replacing $u_{\mathbf{k}'}^+ v_{\mathbf{k}'}$ using Eqs. (2.13) and (2.21), we finally obtain

$$\Delta_{\mathbf{k}} = - \sum_{\mathbf{k}'} V_{\mathbf{k}\mathbf{k}'} \frac{\Delta_{\mathbf{k}'}}{2E_{\mathbf{k}'}} \tanh \frac{E_{\mathbf{k}'}}{2kT}. \quad (2.24)$$

As pointed out in Sec. 2.1, in weak coupling limit the potential is assumed to be non-zero and attractive only within a thin layer over the Fermi surface $\varepsilon \ll \varepsilon_F = \hbar^2 k^2 / 2m$. However, potential is anisotropic, so the Eq. (2.3) should be transformed to

$$V_{\mathbf{k}\mathbf{k}'} = -V \frac{g(\mathbf{k})g(\mathbf{k}')}{N}, \text{ for } \varepsilon_F < \frac{\hbar^2 k^2}{2m}, \frac{\hbar^2 k'^2}{2m} < \varepsilon_F + \varepsilon, \quad (2.25)$$

$$\text{with } N \equiv \int_0^\pi \sin \vartheta' d\vartheta' \int_0^{2\pi} d\varphi' g^2(\mathbf{k}'). \quad (2.26)$$

Putting Eqs. (2.19) and (2.25) into Eq. (2.24) we get

$$Ng(\mathbf{k}) = -\frac{N_0}{4\pi} g(\mathbf{k}) V \int_0^\varepsilon d\xi' \int_0^\pi \sin \vartheta' d\vartheta' \int_0^{2\pi} d\varphi' \frac{g^2(\mathbf{k}')}{2E_{\mathbf{k}'}} \tanh \frac{E_{\mathbf{k}'}}{2kT}.$$

Using the substitution $x = \sqrt{\xi'^2 + \Delta^2 g^2(\mathbf{k}')}$, and using $\varepsilon \gg \Delta$ for integral limits we finally obtain

$$N = -\frac{N_0}{8\pi} V \int_0^\varepsilon dx \int_0^\pi \sin \vartheta d\vartheta \int_0^{2\pi} d\varphi \frac{g^2(\mathbf{k})}{\sqrt{x^2 - \Delta^2 g^2(\mathbf{k})}} \tanh \frac{x}{2kT}. \quad (2.27)$$

Here we dropped the index of \mathbf{k} in the integration which is no longer necessary.

At 0 K, $\tanh(x/2kT)$ is replaced by unity, $\Delta = \Delta(0)$, so the expression after the integration reduces to

$$\begin{aligned} N &= -\frac{N_0}{8\pi} V \int_0^\pi \sin \vartheta d\vartheta \int_0^{2\pi} d\varphi g^2(\mathbf{k}) \int_0^\varepsilon dx \frac{1}{\sqrt{x^2 + \Delta^2(0)g^2(\mathbf{k})}} \\ &= -\frac{N_0}{8\pi} V \int_0^\pi \sin \vartheta d\vartheta \int_0^{2\pi} d\varphi g^2(\mathbf{k}) \ln \frac{\varepsilon + \sqrt{\varepsilon^2 + \Delta^2(0)g^2(\mathbf{k})}}{\Delta(0)g(\mathbf{k})}. \end{aligned}$$

Taking that $\varepsilon \gg \Delta(0)$, we finally obtain

$$N = \frac{N_0}{8\pi} V \left[\int_0^\pi \sin \vartheta d\vartheta \int_0^{2\pi} d\varphi g^2(\mathbf{k}) \ln g(\mathbf{k}) - \ln \left(\frac{2\varepsilon}{\Delta(0)} \right) N \right]. \quad (2.28)$$

On the other hand, at phase transition temperature T_C superconducting gap vanishes $\Delta = 0$ and Eq. (2.27) reduces to

$$\begin{aligned} N &= -\frac{N_0}{8\pi} V \int_0^\pi \sin \vartheta d\vartheta \int_0^{2\pi} d\varphi g^2(\mathbf{k}) \int_0^\varepsilon dx \frac{\tanh(x/2kT_C)}{x} \\ &= -\frac{N_0}{8\pi} V \int_0^\pi \sin \vartheta d\vartheta \int_0^{2\pi} d\varphi g^2(\mathbf{k}) \int_0^{\varepsilon/2kT_C} dy \frac{\tanh(y)}{y} \\ &= -\frac{N_0}{8\pi} V \ln \left(\frac{4e^\gamma}{\pi} \frac{\varepsilon}{2kT_C} \right) N. \end{aligned} \quad (2.29)$$

Here we used expression

$$\int_0^A \frac{\tanh(x)}{x} dx = \ln \left(\frac{4e^\gamma}{2\pi} A \right),$$

where $\gamma \approx 0.577$ is the Euler's constant.

Comparing Eqs. (2.28) and (2.29) we finally obtain

$$\begin{aligned} \Delta(0) &= \pi e^{-\gamma} e^{-S} k_B T_C, \\ \text{with } S &= \int_0^\pi \sin \vartheta d\vartheta \int_0^{2\pi} d\varphi g^2(\mathbf{k}) \ln g(\mathbf{k}) / \int_0^\pi \sin \vartheta d\vartheta \int_0^{2\pi} d\varphi g^2(\mathbf{k}). \end{aligned} \quad (2.30)$$

Obviously, for the isotropic situation $g(\mathbf{k}) = 1$, $S = 0$, and the expression reduces to the well-known BCS expression $\Delta(0) = \pi e^{-\gamma} k_B T_C = 1.76 T_C$.

2.5 Bulk properties

In this Section calculations will be made assuming the closed Fermi sphere. Such Fermi surface is indeed very unlikely to appear in the unconventional superconductors, however such assumption simplifies the explanation of the calculation. On the other hand, the final results are not influenced by the Fermi surface shape, but depend solely on the topology of the nodes.

Knowing the shape of the energy gap for the superconductor, one can easily calculate the variation of thermodynamic quantities at low temperatures. The electronic *specific heat* is defined as

$$C_s = \sum_{\mathbf{k}\alpha} E_{\mathbf{k}} \frac{\partial f_{\mathbf{k}}}{\partial T} = \frac{N_0}{2\pi} \int_0^\infty d\xi \int_0^\pi \sin \vartheta d\vartheta \int_0^{2\pi} d\varphi \frac{1}{T^2} \frac{E_{\mathbf{k}}^2 e^{E_{\mathbf{k}}/T}}{(e^{E_{\mathbf{k}}/T} + 1)^2}. \quad (2.31)$$

In the case of the full gap coupling in the limit, $T \rightarrow 0$, $E_{\mathbf{k}} = \sqrt{\xi^2 + \Delta^2} \approx \Delta + \xi^2/2\Delta$, Eq. (2.31) gives

$$C_s \approx \frac{2N_0\Delta^2}{T^2} e^{-\Delta/T} \int_0^\infty d\xi e^{-\xi^2/2\Delta T} \approx \sqrt{2\pi} N_0 T \left(\frac{\Delta(0)}{T} \right)^{5/2} e^{-\Delta(0)/T}.$$

When energy of the quasiparticle is in the form $E_{\mathbf{k}} = \sqrt{\xi^2 + \Delta^2 \sin^2 \vartheta}$, we see that the gap has nodes for $(\vartheta = 0, \pi)$, that is, two node points appear in the case of the closed Fermi sphere. Taking into consideration that the main contributions to the integral in Eq. (2.31) come from the regions around these node points $(\vartheta < \xi/\Delta, \pi - \vartheta < \xi/\Delta)$, Eq. (2.31) can be rewritten as

$$C_s \approx \frac{N_0}{4\pi T^2} \int_0^\infty d\xi \frac{\xi^2}{\cosh^2(\xi/2kT)} \int_0^{\xi/\Delta} \vartheta d\vartheta \int_0^{2\pi} d\varphi = \frac{7\pi^4}{30} N_0 T \left(\frac{T}{\Delta(0)} \right)^2.$$

When energy of excited electron is in the form $E_{\mathbf{k}} = \sqrt{\xi^2 + \Delta^2 \sin^4 \vartheta \sin^2 2\varphi}$ (d_{xy} -wave), we see that gap has nodes for $(\vartheta = 0, \pi)$ and $(\varphi = 0, \pi/2, \pi, 3\pi/2)$. Latter nodes actually absorb former, so two circles – that is, node lines – appear in the case of the closed Fermi sphere. Taking into consideration that the main contributions to the integral in Eq. (2.31) come from the regions around these lines $(|\varphi| < \xi/\Delta, |\pi/2 + \varphi| < \xi/\Delta, \dots)$, Eq. (2.31) can be rewritten as

$$C_s \approx \frac{N_0}{\pi T^2} \int_0^\infty d\xi \frac{\xi^2}{\cosh^2(\xi/2kT)} \int_0^\pi \sin \vartheta d\vartheta \int_0^{\xi/\Delta} d\varphi = \frac{36\zeta(3)}{\pi} N_0 T \left(\frac{T}{\Delta(0)} \right)^1.$$

The following expressions were used in the calculations above:

$$\int_0^\infty \frac{dz z^4}{\cosh^2 z} = \frac{7\pi^4}{240}; \quad \int_0^\infty \frac{dz z^3}{\cosh^2 z} = \frac{9}{8}\zeta(3)$$

Taking into account that the normal state specific heat at low temperatures is proportional to $C_n \propto T$ and that $T_C \propto \Delta(0)$ we can finally write

$$\frac{C_s}{C_n} \propto \begin{cases} \left(\frac{T_C}{T}\right)^{5/2} e^{-\frac{T_C}{T}}, & \text{nodeless gap,} \\ \left(\frac{T}{T_C}\right)^2, & \text{gap with point nodes,} \\ \left(\frac{T}{T_C}\right), & \text{gap with line nodes.} \end{cases} \quad (2.32)$$

The next important contribution concerns the *paramagnetic susceptibility*. Although the weak magnetic field, which is screened by the persistent superconducting currents, does not penetrate in the superconductor bulk, the spin (Pauli) paramagnetism in superconductors is an observable phenomenon. Now the susceptibility of the electron gas in the superconducting state will be calculated. In the case of the singlet pairing, the superconducting pairs give no contribution to the susceptibility, so the entire spin magnetic moment is due to the quasiparticles

$$M = \mu_B \sum_{\mathbf{k}} [f(E_{\mathbf{k},-}) - f(E_{\mathbf{k},+})],$$

where $E_{\mathbf{k},\pm} = E_{\mathbf{k}} \pm \mu_B H$ are energies of excitations with spins parallel and antiparallel to the magnetic field \mathbf{H} , and $\mu_B = 9.27 \times 10^{-24}$ J/T is Bohr magneton. We can rewrite the expression as

$$M = 2\mu_B^2 N_0 H \left\{ \frac{1}{4\pi} \int_0^\infty d\xi \int_0^\pi \sin \vartheta d\vartheta \int_0^{2\pi} d\varphi \frac{\partial f(E_{\mathbf{k}})}{\partial E_{\mathbf{k}}} \right\} = 2\mu_B^2 N_0 H Y, \quad (2.33)$$

where

$$\begin{aligned} Y = \rho_n &= \frac{1}{8\pi} \int_0^\infty d\xi \int_0^\pi \sin \vartheta d\vartheta \int_0^{2\pi} d\varphi \frac{1}{kT} \frac{e^{E_{\mathbf{k}}/T}}{(e^{E_{\mathbf{k}}/T} + 1)^2} \\ &= \frac{1}{16\pi kT} \int_0^\infty d\xi \int_0^\pi \sin \vartheta d\vartheta \int_0^{2\pi} d\varphi \frac{1}{\cosh^2(E_{\mathbf{k}}/2kT)} \end{aligned} \quad (2.34)$$

is called the *Yosida function* and determines the fraction of the normal electrons ρ_n in the superconductor. Now, the susceptibility is simply defined as

$$\chi = \frac{\partial M}{\partial H} = 2\mu_B^2 N_0 Y. \quad (2.35)$$

Using the same reasoning as for the specific heat, and the expression for the susceptibility in the normal state $\chi_n = 2\mu_B N_0$, it can be easily shown that

$$\frac{\chi_s}{\chi_n} = Y \propto \begin{cases} \left(\frac{T_C}{T}\right)^{1/2} e^{-\frac{T_C}{T}}, & \text{nodeless gap,} \\ \left(\frac{T}{T_C}\right)^2, & \text{gap with point nodes,} \\ \left(\frac{T}{T_C}\right), & \text{gap with line nodes.} \end{cases} \quad (2.36)$$

The spin magnetic moment is also screened by the persistent superconducting currents, so a special procedure should be performed in order to measure susceptibility of the quasiparticles. For that reason the NMR method is employed. It is a well-known fact that, when the sample is located in a magnetic field H , there exists a strong absorption of the electromagnetic radiation at frequencies, which coincide with the magnetic precession frequencies of the nuclear spins. Further, if a particular electron is described by the wave function ψ , there exists a certain probability $|\psi|^2$ that its magnetic moment μ_e is located at the nucleus site with the magnetic moment μ_n . This obviously leads to the interaction between two magnetic moments

$$H_{\text{int}} \propto |\psi|^2 \mu_n \mu_e = |\psi|^2 \mu_n \frac{\chi H}{n_e},$$

where n_e is the density of the (normal) electron gas. The existence of an extra interaction changes the frequency of the absorbed electromagnetic waves by

$$\delta\omega \propto \frac{\mu_n |\psi|^2}{n_e \hbar} \chi H \propto \chi. \quad (2.37)$$

This effect is known as the *Knight shift*. By measuring the ratio $\delta\omega_s/\delta\omega_n$, one can determine the susceptibility of the quasiparticles in the superconducting state, as well as the density of the normal electrons. The Knight shift is also a useful probe for the spin pairing of the superconducting electrons. If the Cooper pair is a singlet, the Knight shift should go smoothly to zero at $T = 0$, which is not the case for the triplet Cooper pair.

Using the similar procedure other physical quantities at low temperatures can be also obtained. Another example is the *spin-lattice relaxation rate* $1/T_1$, which is at low temperatures given as [59]

$$\frac{1}{T_{1,s}} \propto \begin{cases} \left(\frac{T_C}{T}\right)^{7/2} e^{-\frac{T_C}{T}}, & \text{nodeless gap,} \\ \left(\frac{T}{T_C}\right)^5, & \text{gap with point nodes,} \\ \left(\frac{T}{T_C}\right)^3, & \text{gap with line nodes.} \end{cases} \quad (2.38)$$

In a superconductor, the sum of the normal electron density ρ_n and the superconducting electron density ρ_s should give unity. Using Eq. (2.34) we can therefore write

$$\rho_s = 1 - \rho_n = 1 - \frac{1}{16\pi kT} \int_0^\infty d\xi \int_0^\pi \sin \vartheta d\vartheta \int_0^{2\pi} d\varphi \frac{1}{\cosh^2(E_{\mathbf{k}}/2kT)}. \quad (2.39)$$

This physical quantity is usually referred to as the *superfluid density* and is of primary interest in our research. In accordance to the behavior of the normal electron density [Eq. (2.36)], the superfluid density at low temperatures shows exponential temperature behavior for the nodeless superconducting symmetry and power-law, in particular a linear and a squared temperature behavior, for the superconducting gap with the line and the point nodes, respectively.

3 Experimental determination of superconducting quantities

As it was elaborated in Sec. 1.4, an enormous experimental as well as theoretical attention was directed toward the determination of the symmetry of the superconducting state so far, however the effort was shadowed by contradictory results. Starting from this point, our idea was not only to make yet another research of the superconducting state, but also to solve the mystery of the observed discrepancy. Indeed, we believe that our research, considering the experimental technique, has several advantages when compared to the measurements that were done so far.

First, it should be noted that the measurement of the penetration depth has one distinct advantage; The measurements of the penetration depth allow direct calculation of the density of the superfluid electrons. Most experiments described in Sec. 1.4 are based on the measurement of a particular physical quantity, originating from the quasiparticles in the system. Therefore, these experiments usually face large problems in order to distinguish between the quasiparticle contribution and other (most notably phonon) contributions to the measured physical quantity. Further, in our experiment the penetration depth was obtained in the truly Meissner state, so the vortex effects were excluded as well. And finally, we performed full characterization of the material using the same single crystal and the same experimental method in two different magnetic field positions, parallel and perpendicular to the isotropic planes. In order to succeed in obtaining reliable absolute values of the penetration depth, not only in the parallel but also in the perpendicular geometry, for the first time we have used, according to our best knowledge, the improved calibration method in the former case. The details of the experimental technique, as well as the extended data analysis, will be given in the following sections.

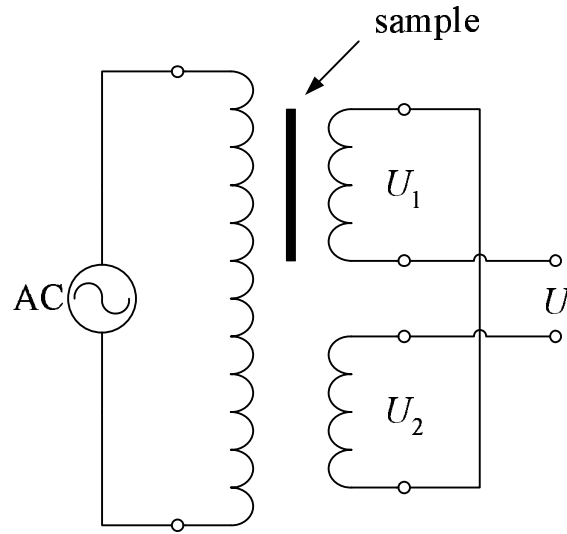


Fig. 3.1: Schematic diagram of the ac susceptibility measurement. For clarity, the secondary coils are drawn outside of the primary coil.

3.1 ac susceptometer

The experimental methods of the magnetic response measurement can be divided into two groups: static and dynamic, depending on whether the sample is placed into the time-invariant or the time-dependent – usually harmonic – magnetic field. The absolute value of the magnetic moment and the change of the magnetic moment, is detected in the former and the latter case, respectively. However, if the measurement is done in the linear part of the magnetic response function near the zero-field value, both methods give the same result. Moreover, the obtained magnetic response function is complex; That is, while the real part of the function gives us a magnetic response of the studied system, the imaginary part of the function gives us an insight into the dissipation processes.

The method of the ac susceptibility [60], as one of the dynamic methods, is based on the fact that the inductance of the coils changes if a magnetized sample is placed inside of it. If such a coil is positioned in the harmonically time-dependent magnetic field, the induced voltage will be changed by the contribution of the sample. The voltage change in the low-field limit can be directly connected to the dynamical ac susceptibility.

In the basic setup the ac susceptometer consists of three coaxially placed coils; One primary coil, which is used to create a time-dependent magnetic field and two identical secondary (pick-up) coils inside of it, which are connected in a way that their induced voltages are subtracted (Fig. 3.1). Ob-

viously, without a sample, the induced voltage of each of the coils equals to $U_1 = U_2 = U_0$, so their subtraction U equals to zero. A magnetized sample inserted in one of the coils changes the magnetic flux Φ threading the coil. Thus, by the virtue of the Faraday law, the overall induced voltage U_1 changes by the flux (i.e., magnetization) time rate

$$U_1 = U_0 + \mu_0 \frac{d\Phi}{dt} = U_0 + \mu_0 GS \frac{dM}{dt}, \quad (3.1)$$

where G represents geometrical factors of the detection coil, S is the filling factor, M sample magnetization, and $\mu_0 = 4\pi \times 10^{-7}$ H/m the permeability of the vacuum. In general, the contribution of the sample is much smaller than the induced voltage of the empty coil. This small signal of our primary interest can be easily extracted by the compensation of U_0 , in a setup described above. In this case the resulting voltage U can be written as

$$U = U_1 - U_2 = \mu_0 GS \frac{dM}{dH} \frac{dH}{dt}, \quad (3.2)$$

if we also take into consideration that the time-dependent magnetic response is introduced by the time-dependent magnetic field. The term dM/dH represents the measured dynamic susceptibility χ_m . If the time-dependent part of the magnetic field H_{ac} is harmonic with the frequency ω , that is

$$H = H_{dc} + H_{ac} e^{i\omega t},$$

the final expression for the resulting voltage reads as

$$U = i \omega \mu_0 GS \chi_m H_{ac}. \quad (3.3)$$

In what follows, we discuss important properties of the ac susceptibility method. First, U is obviously shifted by a certain phase with regard to H_{ac} , and moreover χ_m is in general a complex function. The measurements setup requires therefore a phase-sensitive detection. Further, it is also necessary to ensure that all the relaxation mechanisms in the sample are faster than the change of the magnetic field – in this case the measured susceptibility represents the isothermal susceptibility. In the opposite case we would measure the adiabatic susceptibility, which is always smaller than the isothermal one. Finally, strictly speaking the setup measures the redistribution of the magnetic flux due to the sample insertion into one of the coils. Only if all flux lines originating from the sample are closed outside the secondary coil, the setup measures the sample magnetism. This is precisely true only if the sample area exactly matches the area of the secondary coil. Since this condition is technically impossible to fulfill, a special variable called the *filling*

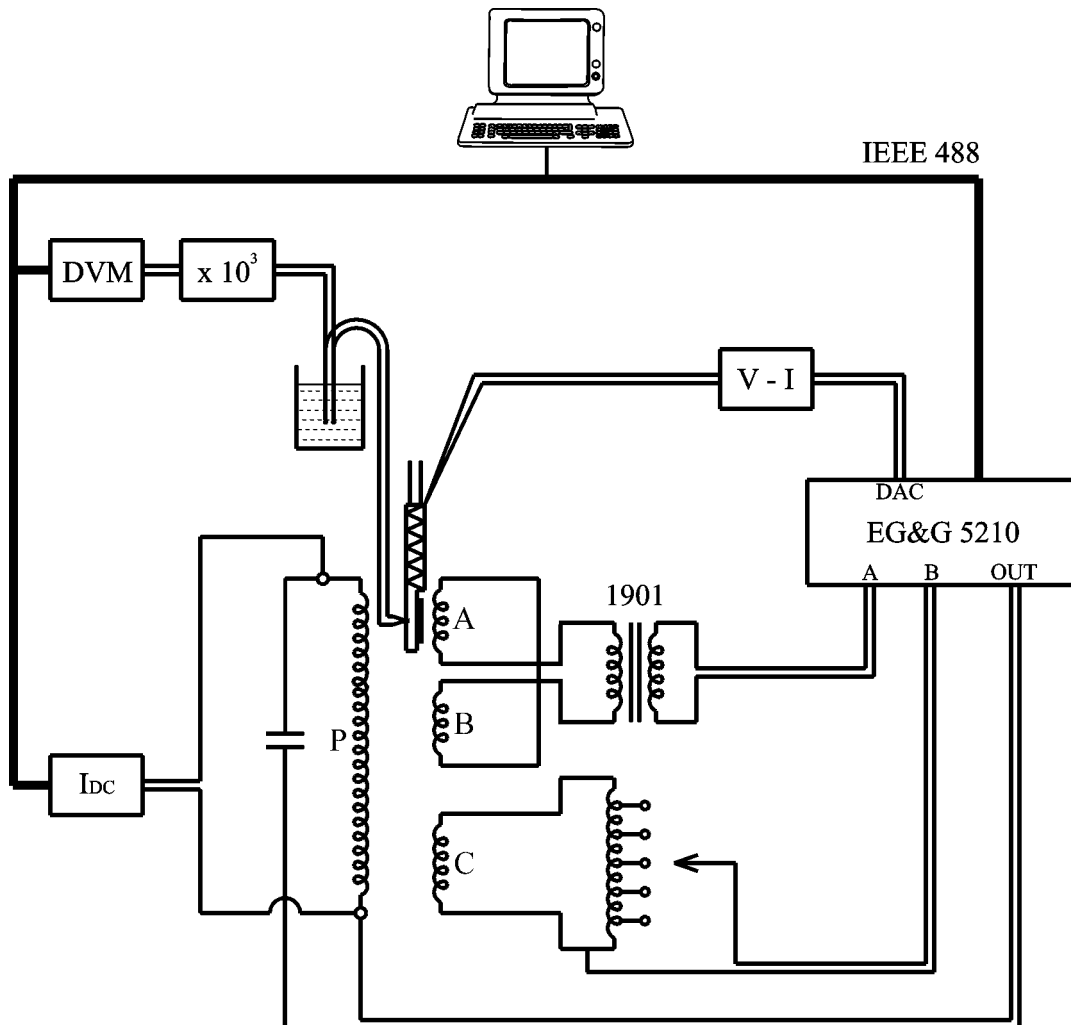


Fig. 3.2: Block scheme of the ac susceptometer. [60]

factor is introduced, which gives the proportion between the measured and the actual flux originating from the sample. The filling factor depends solely on the geometrical factors and is obviously always smaller than the unity. For small samples it is generally proportional to the sample volume.

Measurements of the ac susceptibility were performed using a commercial ac susceptometer (CryoBIND/Sistemprojekt, Zagreb [61]) (Fig. 3.2). A long, four layers copper coil immersed into a liquid nitrogen bath is used as the primary coil (P). Three short coils are used as secondary coils, coaxially positioned along the axis of the primary coil and immersed into a liquid helium bath. Two of them, 14 layers A and B coils, are balanced to the induced voltage equivalent to one coil turn or better. These coils are used to measure

the induced voltage U , as described above, which is then amplified using the EG&G 1901 low noise transformer. When both of them are empty, there still exists a small non-zero induced voltage due to the residual unbalance of the A and B coils. The third secondary coil (C) has the function to compensate this signal with the use of the autotransformer. The lock-in EG&G 5210 is used as the source of the current for the primary coil, as well as the phase sensitive voltmeter. The tip of the sample holder is made of the single crystal sapphire, an electrical insulator with a good thermal conductivity at low temperatures. During the measurement the tip is positioned in the center of the upper secondary coil (A). The heater made of the nonmagnetic resistance wire, and powered by the buffered DAC (digital-to-analog converter) output of the lock-in EG&G 5210, is attached to the top of the sapphire block. The sensitivity of such system, expressed in equivalent magnetic moments, is $\Delta m = 2 \times 10^{-9}$ emu in the broad temperature range. A gold 0.07% iron-copper thermocouple attached to the sapphire block is used as a thermometer. It is distinguished by the high sensitivity in the whole temperature range between 1.5 and 300 K and by the negligible magnetic contribution at low temperatures. The freezing-point of the water is used as a reference temperature. Finally, the studied sample, attached to the sapphire block, has a good thermal contact with both the heater and the thermometer. The whole setup is controlled by the computer.

3.2 Calibration

In addition to the filling factor explained above, another general experimental problem concerning the measurement of susceptibility should be addressed. Namely, when the sample is positioned in the applied magnetic field H_{app} , it is magnetized and its own magnetization M is the source, due to the sample finiteness, of an additional magnetic field in the sample vicinity. This field is historically called the demagnetizing field H_{dem} , since for the paramagnetic materials its contribution is opposite to the applied field. The demagnetizing field is determined by the geometry of the sample and the exact calculation is possible only in the cases of some special geometries. An instructive example represents the ellipsoid sample. When the ellipsoid sample is located in the applied field H_{app} , it is uniformly magnetized [62] and the only H_{dem} contribution, proportional to the sample magnetization, comes from the discontinuity of the magnetization at the sample surface. In calculating the susceptibility, the field that has to be taken into accounts is the total field in the sample vicinity

$$H_{\text{tot}} = H_{\text{app}} + H_{\text{dem}} = H_{\text{app}} - DM.$$

The constant factor D is called the *demagnetization factor* and depends solely on the geometrical parameters of the ellipsoid. For the samples of other regular shapes, magnetization is not uniform, and there is an additional H_{dem} contribution due to the divergence of the sample magnetization. Nevertheless, for some distinct geometries, e.g., disks [63], it is still possible to make approximate calculations of the demagnetization factor. Knowing the value of D , the correction to the measured susceptibility $\chi_m = dM/dH_{\text{app}}$ due to the extra magnetic field can be easily calculated. The correct value of the susceptibility – that is, the value that is the property of the material itself – is then equal to

$$\chi = \frac{dM}{dH_{\text{tot}}} = \frac{dM}{dH_{\text{app}}} \frac{dH_{\text{app}}}{dH_{\text{tot}}} = \frac{\chi_m}{1 - D\chi_m}. \quad (3.4)$$

Real samples practically never come in the ideal shapes and it is practically impossible to perform the precise calibration. Nevertheless, for special cases the demagnetization factor can be neglected. As it was pointed out before, the demagnetization factor depends exclusively on the geometrical parameters of the sample. Further, it turns out that *only* if the dimension of the sample parallel to the magnetic field l_{\parallel} is much larger than the largest dimension of the sample perpendicular to the magnetic field l_{\perp} , i.e., $l_{\parallel} \gg l_{\perp}$, the demagnetization factor is small and can be neglected ($D \approx 0$). As the ratio l_{\perp}/l_{\parallel} increases, D becomes monotonically larger and more sensitive to the tiny difference in the geometrical parameters. Therefore, only the measurement of the needle-shaped samples, with the needle direction parallel to the magnetic field, enables us to get the exact value of the material susceptibility straightforwardly.

In our particular case the material is a quasi-two-dimensional one, so in order to get the full physical characterization of the sample, the magnetization should be measured in at least two distinct orientations. Obviously, even if a particular sample complies with the $l_{\parallel} \gg l_{\perp}$ condition in one of the orientations, it cannot possibly comply with this condition for two distinct orientations. Nevertheless, in order to eliminate the filling factor and to get the exact value of the magnetization in our samples for two distinct orientations, a specially conceived calibration of the system was performed.

The κ -(ET)₂X crystals are thin rhombic platelets with faces parallel to the conducting planes and with a typical face dimension almost one order of magnitude larger than a typical thickness. In order to obtain full characterization of the sample, it has to be attached to the sapphire sample holder in a way that the applied ac field is either perpendicular or parallel to the high-conducting planes of the studied single crystals. From now on, the

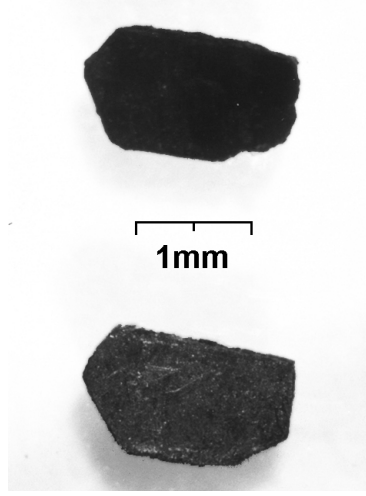


Fig. 3.3: The κ -(ET)₂Br (above) and its reference sample (below).

case of a magnetic field aligned with the crystallographic axis perpendicular to the high-conducting crystal planes [b -axis for κ -(ET)₂Br, a^* -axis for κ -(ET)₂NCS], is denoted as the $H_{ac} \perp$ plane, while the case of a magnetic field direction lying inside the high-conducting crystal plane [ac plane for κ -(ET)₂Br, bc plane for κ -(ET)₂NCS] is denoted as the $H_{ac} \parallel$ plane.

The principle of our calibration is based on the creation of the specially and carefully designed niobium foil, which we will from now on refer to as the *reference sample*. For each κ -(ET)₂Br or κ -(ET)₂NCS single crystal, a special reference sample was created independently to ensure that its dimensions and shape were as close as possible to the original (see Fig. 3.3). Using Eqs. (3.4) and (3.3), the total voltage induced on the detection coils when we measure the κ -(ET)₂X sample can then be rewritten as

$$U = i \omega \mu_0 G S H_{ac} \frac{\chi}{1 + D\chi}. \quad (3.5)$$

Similarly, for the reference sample, the voltage induced on the detection coils equals to

$$U_r = i \omega \mu_0 G S_r H_{ac} \frac{\chi_r}{1 + D_r \chi_r}. \quad (3.6)$$

Index “r” designates the reference sample. From now on, I will refer to the expression $1/(1 + D\chi)$ as the *demagnetization effect*. In general, the susceptibility as well as the induced voltage are complex quantities, and the extraction of the real and the imaginary voltage components leads to complicated expressions. However, since we measure in the purely Meissner regime, where the imaginary component of susceptibility amounts to $\chi'' =$

$\chi_r'' = 0$, Eqs. (3.5) and (3.6) give the exact relationship between the real part of the induced voltage and the real part of the susceptibility.

Taking into account that, at low temperatures, the penetration depth in the niobium reference sample is negligible compared to its dimensions, we can take for calibration purposes that the zero-temperature real susceptibility amounts to $\chi_r'(0 \text{ K}) = -1$ (full diamagnetism). Then we can obtain the value for the susceptibility of the \varkappa -(ET)₂X sample from Eqs. (3.5) and (3.6)

$$\chi' = -\frac{S_r \frac{1}{1-D_r}}{S \frac{1}{1+D\chi'}} \frac{U}{U_r(0 \text{ K})}$$

The corresponding zero-temperature voltage value $U_r(0 \text{ K})$ is obtained by the interpolation of the measured data in the temperature region between the lowest measured temperature $T_{\min} = 4.2 \text{ K}$ and $T_{\max} < T_{C,r} = 9.25 \text{ K}$, where $T_{C,r}$ represents the superconducting phase transition temperature of the reference sample. Interpolations for different T_{\max} values gave practically identical results.

If measured samples are much smaller than the detection coil, the filling factor is generally proportional to the sample volume, so we finally get the following expression

$$\chi' = -\frac{V_r \frac{1}{1-D_r}}{V \frac{1}{1+D\chi'}} \frac{U}{U_r(0 \text{ K})} \quad (3.7)$$

where V and V_r are volumes of the \varkappa -(ET)₂X and the reference sample, respectively.

Diamagnetic volume of the superconducting sample in the Meissner state under an applied magnetic field is related to the absolute real part of the susceptibility $|\chi'| = -\chi'$. The volume of the sample penetrated by the magnetic field is therefore related to $1 - |\chi'| = 1 + \chi'$. The latter quantity enables calculations of the penetration depth and the superfluid density. Obviously, both measured quantities $-\chi'$ and $1 + \chi'$ contain the same experimental error, which in our experiments amounts to a few percent of the measured χ' value. This fact requires special attention when the sample is in the $H_{ac} \perp$ plane geometry.

The calibration procedure described above is widely accepted as reliable for obtaining the absolute value of the penetrated volume and consequently the penetration depth value for the \varkappa -(ET)₂X samples in the $H_{ac} \parallel$ plane geometry. In this geometry the ratio $l_{\parallel}/l_{\perp} \geq 2$ is the largest. The consequence is that D is very small and does not depend much on the sample geometry [63]. In other words, the demagnetization effect is close to 1, and also does not depend much on the sample geometry. Therefore, even if the

κ -(ET)₂X and its reference sample are not very similar, the middle factor in Eq. (3.7) can be simply replaced by the unity:

$$\chi' = -\frac{V_r}{V} \frac{U}{U_r(0K)}. \quad (3.8)$$

Further, in this case the κ -(ET)₂X sample susceptibility is not close to the completely diamagnetic and the penetrated volume and its corresponding quantity $1 + \chi'$ are at least one order of magnitude larger than the experimental error.

This is, however, not true for the $H_{ac} \perp$ plane geometry. In this case the κ -(ET)₂X sample susceptibility is almost completely diamagnetic ($\chi' \approx -1$) and consequently the value $1 + \chi'$ is smaller for about one order of magnitude than in the opposite geometry. Further, the ratio between the sample dimension parallel to the magnetic field and other two perpendicular dimensions is also smaller for about one order of magnitude than for the opposite geometry ($l_{\parallel}/l_{\perp} < 0.5$). As a result, the demagnetization factor is large and much more sensitive to the sample geometry, which increases experimental error in $-\chi'$ and $1 + \chi'$. The strong decrease in $1 + \chi'$ value and the increase in its experimental error leads to a situation, where the $1 + \chi'$ data are smaller than the corresponding error. Obviously, this makes the extraction of the penetration depth values extremely difficult. This is the reason why the previous authors [39, 46], failed to publish *absolute* values of the penetration depth. Taniguchi *et al.* [4] actually performed a simple calibration for this geometry, in order to get absolute values of χ' . They calculated the demagnetization factor using ellipsoid approximation and claimed an error of 10% in χ' absolute value for $\chi' \approx -1$, which we consider to be underestimated, taking into account the complexity of the real sample geometry. Nevertheless, even this error is too large to enable a reliable extraction of the penetration depth.

Initially, following this conventional reasoning, we also did not obtain the absolute value of the penetration depth directly [64]. Later, however, we have developed a method, which strongly decreases the experimental error in χ' to less than 1% and allows us to get the reliable absolute value of penetrated volume for the $H_{ac} \perp$ plane geometry as well [65]. In the following, we argue and show that our claim is justified.

The obvious solution of the problem is to calculate the exact demagnetization factor for both samples, which is however an extremely difficult task. This is due to the fact that the demagnetization factor is analytically available only for ellipsoids and numerically calculated for some other ideal bodies, like cubes and cylinders. The real samples, however, do not match any of these shapes. Therefore, our starting point is that the reference sample represents a perfect copy of the studied sample (Fig. 3.3), implying very close values of

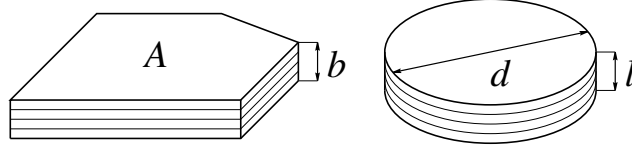


Fig. 3.4: Approximation of the real sample with face area A and thickness b with the disk of diameter $d = 2\sqrt{A/\pi}$ and length of $l = b$.

the respective demagnetization factors D and D_r . Since the \varkappa -(ET) $_2X$ sample susceptibility is almost completely diamagnetic in this geometry, we can use the approximation $\chi' \approx -1$. Therefore, demagnetization effects for both samples must be very close in value and the middle factor in Eq. (3.7) in the first order of approximation can be replaced by the unity. Further, in order to improve the precision and eliminate the small remaining difference in the demagnetization effect, the middle factor in the second order of approximation is calculated by the following procedure. Both \varkappa -(ET) $_2X$ and reference sample were taken to be fully superconducting disks (that is, thin cylinders with an aspect ratio of length and diameter of about 0.4) with the same face area and the same thickness as their originals (Fig. 3.4). We consider the disk approximation to be more suitable for a description of the real sample than the ellipsoid one, used by the authors of Ref. 4. We base this assertion on the fact that the former approximation describes better rather sharp sample edges, which might give a substantial contribution to the demagnetization factor. The middle factor in Eq. (3.7) is then given by the calculated ratio of demagnetization effects for these two bodies, $\frac{1}{1-D_{\text{disk},r}} / \frac{1}{1-D_{\text{disk}}}$, that is

$$\chi' \approx -\frac{V_r \frac{1}{1-D_{\text{disk},r}}}{V \frac{1}{1-D_{\text{disk}}}} \frac{U}{U_r(0\text{K})}. \quad (3.9)$$

The systematic error due to the approximation of the specific shape of samples to the shape of the disk is obviously canceled out by division. Numerical data for the demagnetization factor for the disk were taken from the literature [63].

In order to calculate the area and thickness, the dimensions of both \varkappa -(ET) $_2X$ and reference sample were carefully measured with a high precision of 1%. The precision was verified by the following procedure. All significant niobium reference sample dimensions were measured and the volume was calculated. In addition, the same reference sample was weighted and the volume was calculated using the niobium density $\rho_{\text{Nb}} = 8.57 \text{ g/cm}^3$. The difference between two obtained values was always about 1%. Finally, the middle factor in Eq. (3.9) obtained in this way differs from the unity

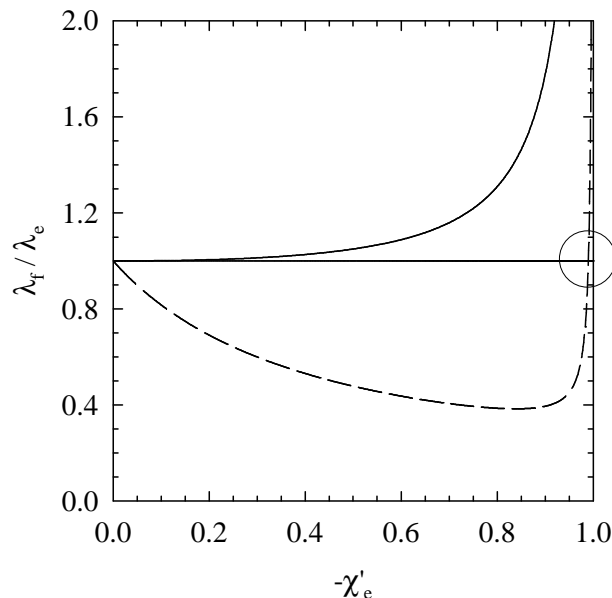


Fig. 3.5: Simulation of the systematic experimental error in the penetration depth evaluation: the ratio of actual and experimentally obtained penetration depth as a function of experimentally obtained susceptibility for *plain* calibration (solid lines) and our *improved* calibration (dashed lines). The circle denotes the area of the most interest.

in only a few percent. This shows that the calculation procedure and the starting assumption are valid.

In the end, we comment on the approximation $\chi' \approx -1$ in Eq. (3.9) in the cases when the susceptibility is not very close to -1 . In order to probe the systematic experimental error in the whole susceptibility range $0 > \chi' > -1$ for the $H_{ac} \perp$ plane geometry, a computer simulation has to be done. The disk approximation of our typical sample gives the demagnetization factor in range $0.7 > D > 0.5$. Since the real sample has more irregular face contours, compared to the round contour of the disk approximation, the real sample demagnetization factor should be somewhat larger. Therefore, in the computer simulation we postulated that the actual demagnetization of the sample amounts to $D_f \approx 0.7$. For the sake of comparison we shall simulate the results as if two different calibrations were used for the $H_{ac} \perp$ plane geometry; the one that was used in the $H_{ac} \parallel$ plane geometry [Eq. (3.8)], denoted as the *plain* calibration and the one that was used in the $H_{ac} \perp$ plane geometry [Eq. (3.9)], denoted as the *improved* calibration, despite of the fact that we have already argued that the former is not effective. In order to make the simulation, the difference between the experimental estimation

of the demagnetization factor D_e and the actual demagnetization factor D_f should also be defined. $D_e/D_f \approx 0.85$ and $D_e/D_f \approx 0.99$ was postulated for *plain* and *improved* calibration, respectively. The results of the simulation are presented in the Fig. 3.5. There the ratio of the actual λ_f and the experimentally obtained λ_e penetration depth as a function of the experimentally obtained susceptibility χ'_e is shown for both calibrations. When χ' approaches -1 , $1 + \chi'$ approaches zero, its error becomes uncomparably larger than the value itself, so the systematic error diverges for all calibrations. However, for $\chi' \approx -0.99$ situation differs significantly. While the error for the *plain* calibration is still huge ($\lambda_f/\lambda_e \approx 10$), the *improved* calibration already gives a reasonably small systematic error (see the encircled area). These results are in full accordance with what we have pointed out before; That is, it is generally believed that it is impossible to make a successful calibration in the proximity of $\chi' \approx -1$, but also that our improved analysis strongly improves the situation for samples with almost completely diamagnetic susceptibility. On the other hand, it should be noted that for $\chi' > -0.98$ the *improved* calibration becomes less reliable. For $\chi' > -0.8$ it is even less reliable than the *plain* calibration.

In the end, we resume that our *improved* calibration procedure for the $H_{ac} \perp$ plane geometry is accurate in $1 + \chi'$ to $\pm 33\%$ for χ' close to -1 and to about -50% for $-0.96 > \chi' > -0.5$. As for the $H_{ac} \parallel$ plane geometry, the accuracy in $1 + \chi'$ is estimated to be about 15% for all measured low-temperature χ' values.

3.3 Experimental conditions

In order to probe the samples in the Meissner state care was taken to reduce the amplitude of the ac field (H_{ac}) until the component $\chi'(T)$ was independent of H_{ac} ($H_{ac} < 42$ mOe) and the $\chi''(T)$ component was negligible. The field used for the extraction of the penetration depth, $H_{ac} = 14$ mOe is well below the critical field for both conditions. Still it is large enough to perform reliable measurements. No frequency dependence ($13 \text{ Hz} < f < 2 \text{ kHz}$) was observed for $H_{ac} < 1$ Oe, so the frequency of the magnetic field was fixed to 231 Hz. In addition no influence of the Earth's field was observed: runs performed with compensation for the Earth's field gave the same results. This is in accordance with the fact that the reported values for lower critical magnetic fields $H_{C1}(T)$, corrected for demagnetization, are far above the Earth's field H_E for all temperatures below 8 K. In this temperature region $H_{C1}(T) \geq 10$ Oe (see Fig. 1.16 on Page 21) [34], while the value of the Earth's field obtained in our laboratory is $H_E \approx 0.36$ Oe [66].

The data were taken by warming in well-controlled temperature sweeps between the lowest attainable temperature 1.5 K (obtained by pumping liquid helium bath) and about 1 K above the phase transition temperature T_C . The temperature sweep speed was between 0.3 K/min and 0.5 K/min. Another issue that drew our attention was the possibility of an experimental artefact in temperature measurement, due to the thermal gradients along the sample holder. Namely, for different sample orientations the position of the sample on the holder differs and for the $H_{ac} \parallel$ plane geometry the thermometer is located almost half-way between the sample and the heater. Despite the fact that the choice of the sapphire as the sample holder material does not favor the presence of any large gradient, we decided to perform a straightforward experimental test to eliminate the possibility of the appearance of the artefact. For this purpose one of the reference niobium samples, which has been used for calibration, was measured at same two distinct positions on the sample holder and under the same measuring conditions as the sample itself, that is, sweep speed was between 0.3 K/min and 0.5 K/min. For all orientations and sweep speeds, the obtained phase transition temperature was in the range of $9.25 \text{ K} < T_{C,r} < 9.29 \text{ K}$. The results show that only a small temperature difference less than 0.05 K exists between the curves, in particular in the region of the onset of diamagnetism (i.e., T_C) and that the value is in full accordance with the literature value of $T_{C,r} = 9.25 \text{ K}$.

3.4 Penetration depth extraction

Once the susceptibility data are obtained, they have to be analyzed in order to obtain the penetration depth temperature dependance, as well as the values at zero temperature. The starting point is the standard formula for a thin superconducting plate in a parallel field [67]

$$1 + \chi' = \frac{2\lambda}{l} \tanh\left(\frac{l}{2\lambda}\right), \quad (3.10)$$

where λ is the penetration depth and l is the sample width in the direction of the field penetration. If we take into account that the ratio $(2\lambda)/l$ is actually the ratio between the volume penetrated by the magnetic field V_P and the whole sample volume V , we can generalize Eq. (3.10) to

$$1 + \chi' = \frac{V_P}{V} \tanh \frac{V}{V_P}. \quad (3.11)$$

In the $H_{ac} \parallel$ plane geometry circulating supercurrents flow within the isotropic planes and also across them, giving a contribution to two distinct in-plane λ_{in} and out-of-plane λ_{out} penetration depths, respectively [see

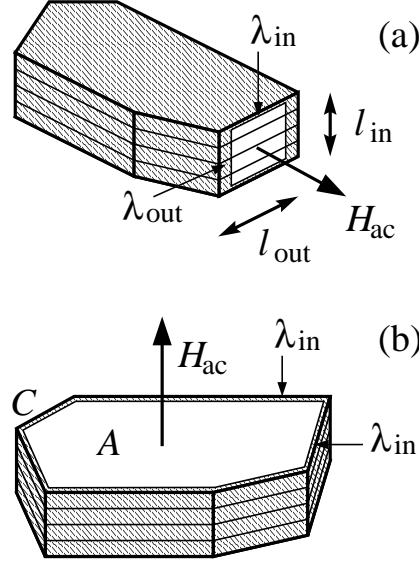


Fig. 3.6: Simplified depiction of the sample in (a) $H_{ac} \parallel$ plane and (b) $H_{ac} \perp$ plane geometry. Shaded parts of the sample represent the volume penetrated by the magnetic field. Condition $\lambda_{out}/\lambda_{in} \gg l_{in}/l_{out}$ in (a) ensures that λ_{in} can be neglected in the analysis.

Fig. 3.6(a)]. Then Eq. (3.11) should be rewritten as

$$1 + \chi' = \left(\frac{2\lambda_{out}}{l_{out}} + \frac{2\lambda_{in}}{l_{in}} \right) \tanh \left(\frac{2\lambda_{out}}{l_{out}} + \frac{2\lambda_{in}}{l_{in}} \right)^{-1}. \quad (3.12)$$

However, in most of the studied crystals the condition $\lambda_{out}/\lambda_{in} \gg l_{out}/l_{in}$ is easily fulfilled, no matter which absolute λ values from literature are used. Then the in-plane penetration depth λ_{in} can be neglected in Eq. (3.12) and the out-of-plane penetration depth λ_{out} can be obtained from the susceptibility data using the expression [see Fig. 3.7(a)]

$$1 + \chi' = \frac{2\lambda_{out}}{l_{out}} \tanh \left(\frac{l_{out}}{2\lambda_{out}} \right). \quad (3.13)$$

The direct confirmation of the validity of use of Eq. (3.13) instead of Eq. (3.12) was verified on two measured samples, as will be shown in the beginning of Sec. 5.2.

Especially, if the sample sides are not aligned perfectly to the magnetic field, or the sample does not have regular and mutually perpendicular sides [see Fig. 3.7(b)], then the expression for the penetration depth can be extracted directly from Eq. (3.11). In this case the penetrated volume amounts

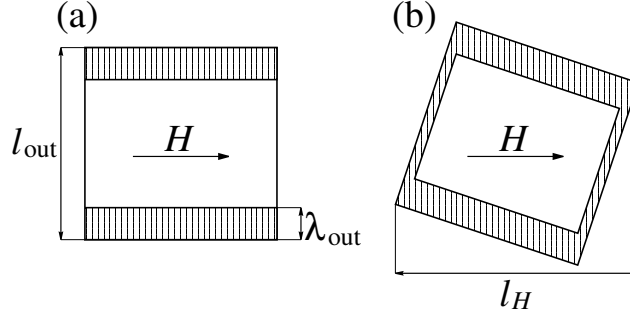


Fig. 3.7: Simplified depiction of the sample in the $H_{ac} \parallel$ plane geometry for the situations (a) when the sample sides are perfectly aligned to the magnetic field and (b) when the sample sides are canted from the magnetic field direction. Shaded parts of the sample represent the area (volume) penetrated by the magnetic field. λ_{in} contribution is not shown.

to $V_P \approx 2l_H\lambda_{out}d$ and the whole volume to $V = Ad$, where d is the thickness of the sample, A the area of the face, and l_H the maximal dimension in the direction of the magnetic field. Finally, this gives us the following expression

$$1 + \chi' = \frac{2l_H\lambda_{out}}{A} \tanh \frac{A}{2l_H\lambda_{out}} \equiv \frac{2\lambda_{out}}{l_\lambda} \tanh \frac{l_\lambda}{2\lambda_{out}}, \quad (3.14)$$

where l_λ is defined as $l_\lambda \equiv A/l_H$. In most cases sample sides are not perfectly aligned to the magnetic field, so in the analysis Eq. (3.14) was used much more often than Eq. (3.13).

Now we address in more detail the $H_{ac} \perp$ plane geometry. The magnetic field is strictly perpendicular to the conducting planes, so is the responding magnetization that expels it out of the bulk. The resultant circulating supercurrents will therefore flow within the planes, which will only give a contribution to in-plane penetration depth λ_{in} [see Fig. 3.6(b)].

Initially, as it was elaborated in the previous Section, we failed to obtain the absolute value of the susceptibility in this particular direction because of the calibration reasons. However, following the method of Kanoda *et al.* [46] it is still possible to determine the deviation of λ_{in} from the minimum value at the lowest attainable temperature T_{min} . For a thin round disk of radius R , the authors of Ref. 46 obtained the following approximate expression

$$\lambda_{in}(T) - \lambda_{in}(T_{min}) = R \left[1 - \left(\frac{\chi'(T)}{\chi'(T_{min})} \right)^{1/3} \right]. \quad (3.15)$$

They also argued that this expression is free from simplifications made in its extraction. Therefore, for thin disks, which are not perfectly round, the

sample radius in the expression can be replaced by $R = (A/\pi)^{1/2}$, where A is the area of the sample large face. This expression was regularly used in our earlier susceptibility measurements, since it enabled, combined with the penetration depth values from other experiments, the full determination of the penetration depth temperature dependence [64].

Since the absolute value of the susceptibility is accessible due to the *improved* calibration, we are also able to determine the absolute value of the susceptibility. Consequently, the penetration depth can be determined as well, starting from Eq. (3.11). If the sample has the shape of a platelet, the magnetic field penetrates along the whole edge of the face and we can rewrite the generalized formula to

$$1 + \chi' = \frac{C\lambda_{\text{in}}}{A} \tanh \frac{A}{C\lambda_{\text{in}}}, \quad (3.16)$$

where C is the circumference and A the area of the platelet face [see Fig. 3.6(b)].

3.5 Superfluid density analysis

The final step of the experimental research consists of the superfluid density ρ_s determination. This physical quantity can be constructed using the classical London equation, stating

$$\lambda^2 = \frac{mc^2}{4\pi\rho_s e^2}, \quad (3.17)$$

where $c = 3 \times 10^8$ m/s is the speed of light, while $m = 9.1 \times 10^{-31}$ kg and $e = 1.6 \times 10^{-19}$ As represent the electron mass and charge, respectively. In the quasi-two-dimensional system, two superfluid densities, in-plane superfluid density $\rho_{s,\text{in}}$ and out-of-plane superfluid density $\rho_{s,\text{out}}$ can be constructed

$$\rho_{s,\text{in}} = \left(\frac{\lambda_{\text{in}}(0)}{\lambda_{\text{in}}(T)} \right)^2, \quad (3.18)$$

$$\rho_{s,\text{out}} = \left(\frac{\lambda_{\text{out}}(0)}{\lambda_{\text{out}}(T)} \right)^2, \quad (3.19)$$

where we have taken into consideration that at 0 K all electrons are in the superconducting state, that is $\rho_{s,\text{in}}(0) = \rho_{s,\text{out}}(0) = 1$.

In order to compare the experimental data to the theoretical predictions, a fit to the experimental data should be performed. Since the theoretical expressions usually cannot be easily handled mathematically, the solution

appears to fit the data between the lowest temperature and the phase transition temperature T_C to the polynomial expressions. On the other hand, the theoretical expression can be expanded to the polynomial expression as well and the obtained coefficients can be then compared. As it was shown in Sec. 2.5, since the experimental data strongly suggest the existence of line nodes in the superconducting gap, the in-plane penetration depth $\rho_{s,\text{in}}$ should comply with a linear dependence at low temperatures. On the other hand, as it will be shown in Sec. 6.3, the out-of-plane penetration depth $\rho_{s,\text{out}}$ is intimately connected to the Josephson coupling between conducting planes, indicating a squared dependence at low temperatures. Therefore, both expressions written in terms of reduced temperature $t = T/T_C$ are

$$\rho_{s,\text{in}}(t) = \left(\frac{\lambda(0)}{\lambda(t)} \right)^2 = 1 - bt - ct^3 - dt^5 - et^6, \quad (3.20)$$

$$\rho_{s,\text{out}}(t) = \left(\frac{\lambda(0)}{\lambda(t)} \right)^2 = 1 - bt^2 - ct^4 - dt^5 - et^6. \quad (3.21)$$

The expressions require a simultaneous fit to four parameters. This is practically impossible to achieve, if we take into account that parameters depend on each other, therefore a special procedure was developed in order to obtain the parameters. We start by fitting the parameter b in the low-temperature region, where the contribution of other parameters should be still negligible. On the other hand, at temperatures close to T_C ($t \lesssim 1$) we fit the function derivation to the slope in the measured data

$$\left. \frac{d\rho_s}{dt} \right|_{t \lesssim 1} \equiv -\eta. \quad (3.22)$$

Finally, if we take into consideration that the superfluid density in the normal state should vanish

$$\rho_s(1) = 0, \quad (3.23)$$

we reduced our problem to three unresolved parameters (c , d , and e) and two equations [Eqs. (3.22) and (3.23)]. If we use those two equations in order to eliminate the parameters d and e , we obtain

$$\rho_{s,\text{in}}(t) = (-t^5 + 2t^4 - t^3)c + [(-3b - \eta + 4)t^5 + (4b + \eta - 5)t^4 - bt + 1], \quad (3.24)$$

$$\rho_{s,\text{out}}(t) = (-t^5 + 2t^4 - t^3)c + [(-2b - \eta + 4)t^5 + (3b + \eta - 5)t^4 - bt^2 + 1]. \quad (3.25)$$

thus the only remaining unresolved parameter c can be obtained by the fit to the data in the whole temperature region.

When one deals with the real data, two additional problems appear. First, it is difficult, and arbitrary to some degree, to determine the exact value of T_C . The problem is manifested in a way that for a bad choice or determination of T_C , ρ_s data do not tend to 0 for $T = T_C$. This problem can be solved by generalization of the Eq. (3.22)

$$\left. \frac{d\rho_s}{d\left(\frac{T}{T_C}\right)} \right|_{T \approx T_C} \equiv -\eta, \quad (3.26)$$

and by letting T_C to be the second fit parameter of a previously one-parameter fit for η

$$\rho_s = \eta - \frac{\eta}{T_C} T. \quad (3.27)$$

Now, T_C and η are fitted simultaneously.

Secondly, in order to construct the superfluid density using Eqs. (3.18) and (3.19), one has to insert the corresponding $\lambda(0)$ values into the expressions. The solution is somewhat more straightforward when the experimental and the calibration procedure give absolute $\lambda(T)$ values. On the other hand, if the $\lambda(T) - \lambda(T_{\min})$ data are obtained in the experiment, using Eq. (3.15), the $\lambda(0)$ value is taken from the literature. However, the construction of the absolute penetration depth $\lambda(T) = [\lambda(T) - \lambda(T_{\min})] + [\lambda(T_{\min}) - \lambda(0)] + \lambda(0)$ points to the missing parameter $\Delta\lambda \equiv \lambda(T_{\min}) - \lambda(0)$, which should be extracted from the experimental data. Once $\lambda(0)$ or $\Delta\lambda$ are obtained from the experimental data, they can be optimized in the ρ_s fits in order to get as good concordance as possible between the data and the fit parameters. This is done by replacing the coefficient of t^0 , which by the definition in Eqs. (3.20) and (3.21) equals the unity, with undetermined coefficient a . Then the former low-temperature one parameter fit to b will be replaced by the two parameters fit to a and b . Further, the existence of the additional parameter a slightly modifies Eqs. (3.24) and (3.25) to:

$$\begin{aligned} \rho_{s,\text{in}}(t) = & (-t^5 + 2t^4 - t^3)c + \\ & + [(-3b - \eta + 4a)t^5 + (4b + \eta - 5a)t^4 - bt + a], \end{aligned} \quad (3.28)$$

$$\begin{aligned} \rho_{s,\text{out}}(t) = & (-t^5 + 2t^4 - t^3)c + \\ & + [(-2b - \eta + 4a)t^5 + (3b + \eta - 5a)t^4 - bt^2 + a]. \end{aligned} \quad (3.29)$$

If the obtained value a differs from the unity, then $\lambda(0)$ and $\Delta\lambda$ should be corrected in order to fulfill the condition $\rho_s(0) = 1$. From the conditions

$$\begin{aligned} \left(\frac{\lambda(0)_{\text{new}}}{f(T)} \right)^2 &= \frac{1}{a} \left(\frac{\lambda(0)}{f(T)} \right)^2, \\ \left(\frac{\lambda(0)}{\lambda(0) + \Delta\lambda_{\text{new}} + f(T)} \right)^2 &= \frac{1}{a} \left(\frac{\lambda(0)}{\lambda(0) + \Delta\lambda + f(T)} \right)^2, \end{aligned}$$

we obtain

$$\lambda(0)_{\text{new}} = \frac{\lambda(0)}{\sqrt{a}}, \quad (3.30)$$

$$\Delta\lambda_{\text{new}} \approx \sqrt{a}(\lambda(0) + \Delta\lambda) - \lambda(0). \quad (3.31)$$

for new $\lambda(0)$ and $\Delta\lambda$ values. [The second expression is iterative and based on the presumption that $f(T)(\sqrt{a} - 1) \ll \lambda(0)(\sqrt{a} - 1) + \sqrt{a}\Delta\lambda$ in the low-temperature fit region.] Only after our corrected $\lambda(0)$ and $\Delta\lambda$ values result in the parameter value $a = 1$, we continue with the above described procedure; That is, in the second step in the high-temperature limit fit η and T_C are obtained and finally the parameter c is fitted by the fit in the whole temperature region by Eqs. (3.24) and (3.25).

4 Investigation of the insulating spin density wave state

Despite the fact that our primary interest is the investigation of the superconducting state, an insulating antiferromagnetic state also requires a special attention. Namely, since these states are immediate neighbors, the characterization of the latter might prove to be crucial for understanding of the former.

As pointed out in the Sec. 1.3, it was found that below $T_C = 22$ K the antiferromagnetic ground state with a very small canting of spins is established in κ -(ET)₂Cl [6]. The canting of spins results in a weak ferromagnetic state with domain structure consisting of equivalent spin configurations. In order to understand the dynamics of the ground state even better, we have conducted an investigation of its charge response.

4.1 Samples and the experimental setup

Two high-quality single crystals of κ -(ET)₂Cl, in the shape of rhombic platelets with face areas of about 1.4 mm² and thickness of about 0.2 mm, were studied. From two to four probes were attached to a single crystal using silver paste. The measured contact resistance was less than 20% of the sample resistance and no imaginary component in the resistance was observed at RT. Therefore, the influence of the contacts should be negligible. The sample holder was immersed into a liquid helium bath, and the temperature was measured using the silicon diode or carbon glass resistive thermometers. In order to avoid sample cracks, the sample was cooled using a typical cooling rate of -0.1 K/min between RT and the liquid nitrogen temperature. Below the latter temperature, the sample was cooled using a typical cooling rate of -1 K/min.

The temperature dependent dc resistivity was measured in the two-probe and four-probe configurations, while the nonlinear dc resistivity was measured in the four-probe configuration using the standard dc techniques.

Keithley 220 was used as a current source, while Keithley 181, 182, and 196 were used as voltmeters. For large sample impedances electrometer Keithley 617 in V-I mode was also used, that is the current through the sample was measured after a fixed voltage was applied to the sample. The complex conductivity was measured in the two-probe configuration by the Hewlett-Packard 4284A impedance analyzer ($\nu = 20 \text{ Hz} - 1 \text{ MHz}$). To exclude possible effects due to the sample holder and cables the so-called open-measurement conductivity was performed; That is, the conductivity was measured first with the sample mounted on the sample holder, and then with the empty sample holder. The deduction of the latter from the former result gives the actual sample conductivity.

The complex dielectric function $\varepsilon = \varepsilon' + i\varepsilon''$ can be obtained from the measured complex conductivity $\sigma = \sigma'(\omega) + i\sigma''(\omega)$ using the following expressions

$$\varepsilon'(\omega) = \frac{\sigma''(\omega)}{\varepsilon_0\omega} \quad (4.1)$$

$$\varepsilon''(\omega) = \frac{\sigma'(\omega) - \sigma_0}{\varepsilon_0\omega} \quad (4.2)$$

where $\nu = \omega/2\pi$ stands for the frequency, $\varepsilon_0 = 8.85 \times 10^{-12} \text{ F/m}$ for the permittivity of the vacuum and σ_0 for the dc conductivity. A special care was taken in the determination of σ_0 , which was obtained by the extrapolation of the frequency dependent conductivity to low frequencies.

4.2 Single particle resistivity

In order to avoid the contribution of the collective modes to the conductivity, single particle resistivity was probed in the linear $I - V$ range, i.e., the measurement current was limited to the range, in which the resistivity of sample was independent of the current. dc resistance, shown in Fig. 4.1, increases below room temperature according to the Arrhenius law. Activation energy between 300 and 70 K and between 50 and 25 K amounts to 118 K and 273 K, respectively. This is in good agreement with previously reported results [8]. Below 25 K the activation energy decreases and between 25 and 10 K amounts to 150 K. Below 10 K, the resistance change starts to level off, and its temperature dependence can be described equally well by the semiconducting activation with the activation energy of 21 K, as well as by the variable range hopping mechanism. The latter mechanism suggests that the number of single particle carriers, due to the thermal activation

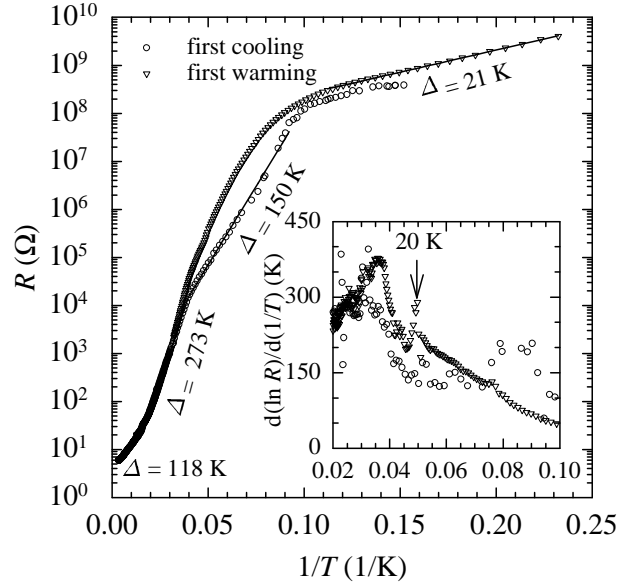


Fig. 4.1: The temperature dependence of the dc resistance for the first cooling and the first warming. Inset shows the temperature dependence of the activation energy.

over the semiconducting gap, is reduced so much that the dominant contribution to conductivity comes from the charge carriers localized on randomly distributed impurities.

We have also observed a hysteresis in the resistance behavior between 10 K and 25 K. That is, the first half-cycle cooling curve with a well defined activation energy of 150 K differs from the curve obtained for all other cooling and warming half-cycles, where the change of the activation energy is gradual in the whole temperature region. Up to now, we do not have plausible explanation for this hysteresis.

Finally, the inset of Fig. 4.1 shows $d(\ln R)/d(1/T)$, which obviously corresponds to the activation energy Δ . We can identify the phase transition with the appearance of a clear peak in the value of the activation energy at 20 K. The peak in cooling is not as clearly distinguishable as it is in warming. This is due to the fact that the cooling sweep is harder to stabilize and a smaller number of temperature points was taken in the same temperature region. The meaning of a broad peak in warming above 25 K remains unknown.

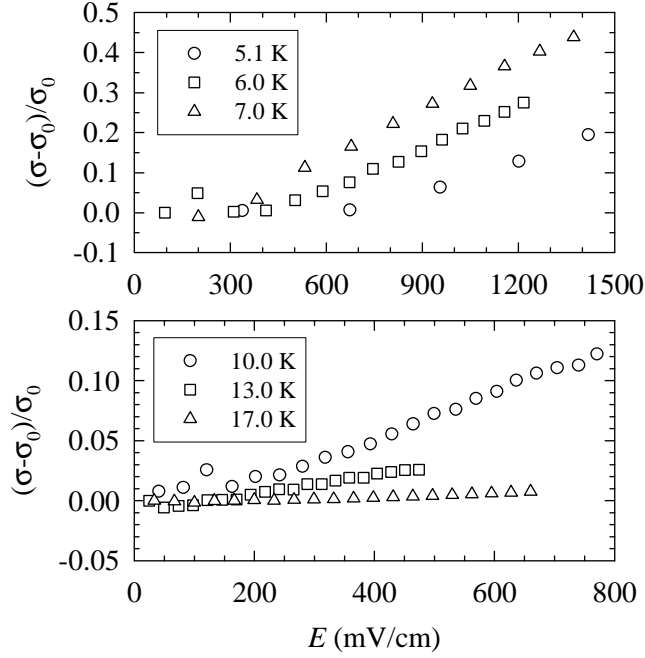


Fig. 4.2: The electrical field dependent conductivity normalized to its ohmic value at six representative temperatures.

4.3 Non-ohmic conductivity

Next we present the results of the field-dependent conductivity measurements. In order to obtain reliable results, we have adjusted the time constant of the measurement $\tau = RC$ according to the increase of the sample resistivity. Further, we have ensured that the current through the sample did not produce a heat exceeding $0.5 \mu\text{W}$, in which case a temperature gradient on the sample holder between the thermometer and the sample may appear.

Below the phase transition temperature the increase of the conductivity above a finite electrical threshold field indicates the opening of a collective conductivity channel (Fig. 4.2). The temperature dependence of the *electrical threshold field* E_T , as well as the non-ohmic conductivity at twice the threshold field, normalized to its ohmic value $(\sigma - \sigma_0)/\sigma_0|_{2E_T}$ are presented in Figs. 4.3 and 4.4.

The behavior of these two quantities can be separated into two distinct temperature regions. At about 13 K, the E_T has a minimum value (Fig. 4.3). Its increase toward the phase transition temperature can be well understood in the frame of the standard model of the sliding spin density wave, weakly pinned to the randomly distributed impurities [68, 69]. However, $(\sigma - \sigma_0)/\sigma_0|_{2E_T}$ is practically negligible in the same temperature region

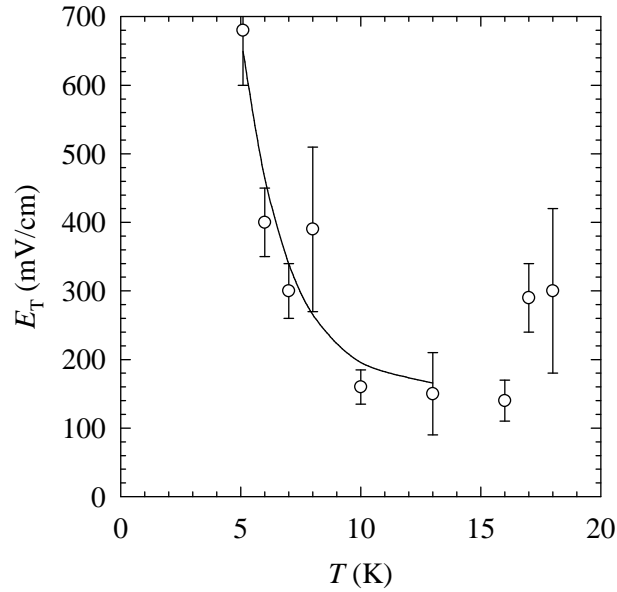


Fig. 4.3: The electrical threshold field as a function of the temperature. Full lines correspond to the fit to the expression $E_T(T) = A \exp[-T/T_0] + B$. See the text for details.

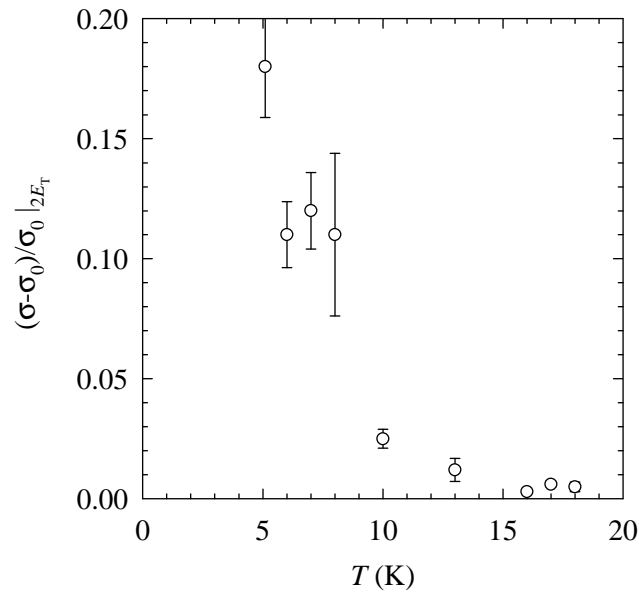


Fig. 4.4: The non-ohmic conductivity at twice the threshold field, normalized to its ohmic value, as a function of the temperature.

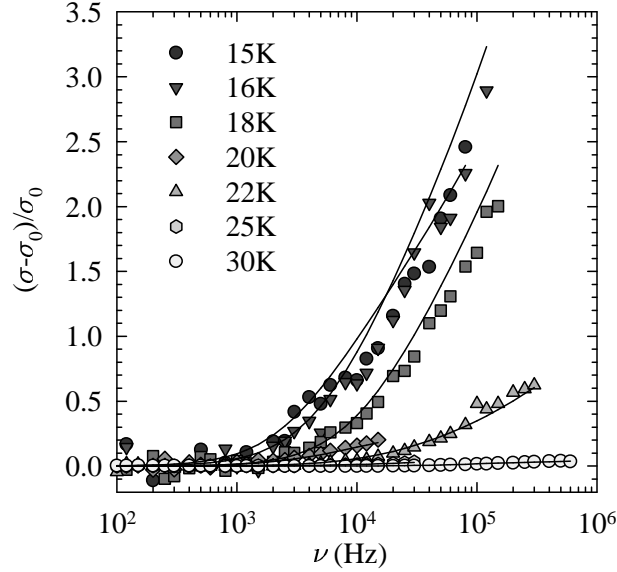


Fig. 4.5: Frequency dependent real part conductivity normalized to its ohmic value at seven representative temperatures.

(Fig. 4.4).

It is interesting to note that increase of E_T toward low temperatures below 13 K (Fig. 4.3) fits well to expression predicted for the charge density waves [68]

$$E_T(T) = Ae^{-\frac{T}{T_0}} + B, \quad (4.3)$$

giving the values of $T_0 = 1.9$ K, $A = 7000$ mV/cm and $B = 160$ mV/cm for the parameters. To our knowledge, this behavior was previously observed only in the NbSe₃ material [70]. However, the semimetallic NbSe₃ with the charge density wave and the semiconducting κ -(ET)₂Cl with the spin density wave have nothing else in common. Furthermore, the increase of the E_T is accompanied by the strong increase of $(\sigma - \sigma_0)/\sigma_0|_{2E_T}$ as well (Fig. 4.4), which is in contradiction to the expectations. Thus it remains unclear how to relate the partial success of the theoretical prediction to the observed ground state.

4.4 ac conductivity

Now we show the frequency-dependent dielectric response. Above 32 K no frequency dependence of the conductivity was observed. The obtained real part conductivity as a function of the frequency below that temperature is presented in Fig. 4.5. Note that the effect appears above the temperature

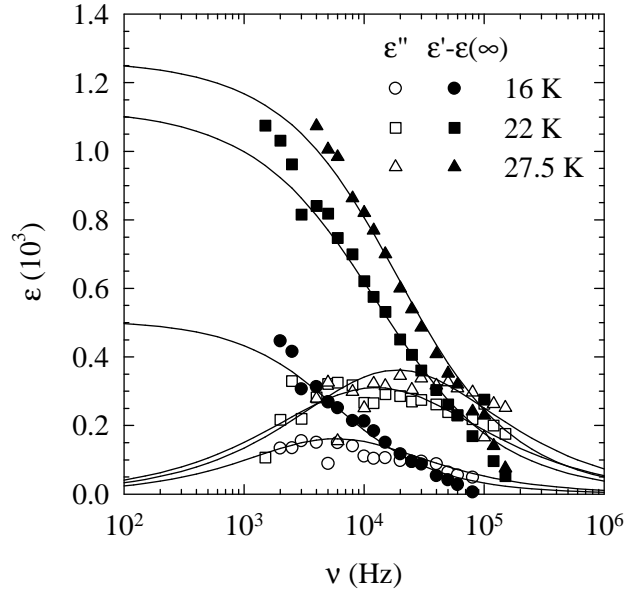


Fig. 4.6: The real and imaginary parts of the dielectric function *versus* the frequency at three representative temperatures. Full lines correspond to fits to the HN function.

of the phase transition, which can be explained in terms of spin density wave fluctuations.

Using Eqs. (4.1) and (4.2) we calculated the frequency dependent dielectric function. Fig. 4.6 shows frequency domain plots of the real and imaginary parts of the dielectric function at three representative temperatures. The full lines in Fig. 4.6 correspond to the calculated fits to the *Havriliak-Negami* (HN) function

$$\varepsilon(\omega) - \varepsilon(\infty) = \frac{\Delta\varepsilon}{1 + (i\omega\tau_0)^{1-\alpha}}, \quad (4.4)$$

which represents empirical generalization of the Debye relaxation. Here $\Delta\varepsilon$ represents the *dielectric strength*, τ_0 the *mean relaxation time* and $1 - \alpha$ the *width of the relaxation time distribution*. In order to obtain a better resolution and precision, we have fitted ε data in the complex plane; That is, the real and imaginary parts of the dielectric function were simultaneously fitted to the same set of parameters.

The three parameters of the fit, which fully characterize the dielectric relaxation, as a function of the inverse temperature, are shown in Fig. 4.7. The dc resistance is also shown for comparison. The value of the dielectric strength decreases with the decrease of the temperature. Further, it is much larger than the value expected due to single particle contributions, so the

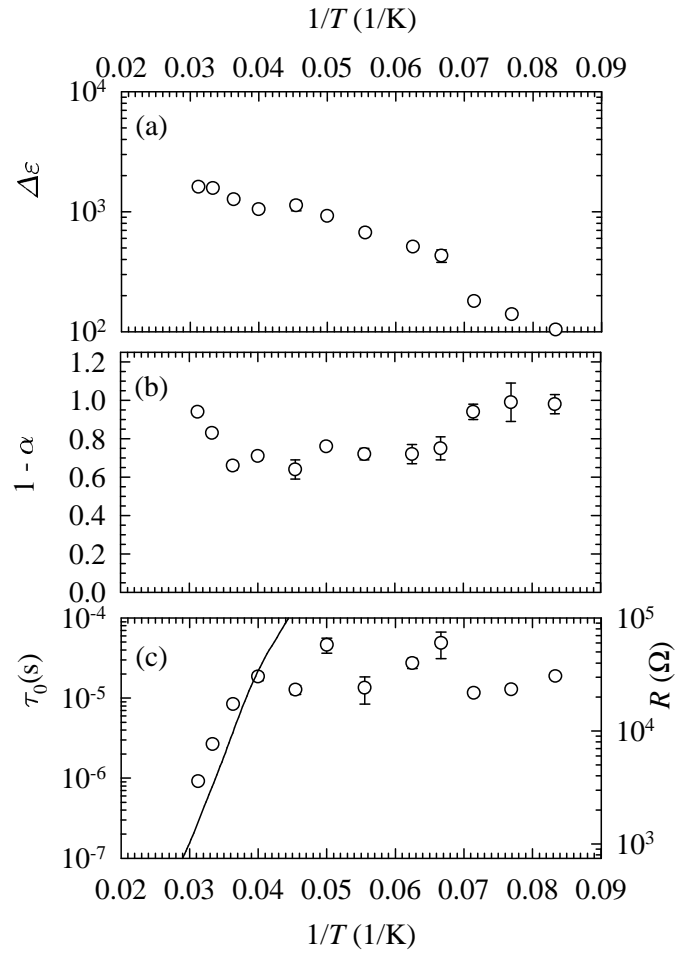


Fig. 4.7: (a) Dielectric strength ($\Delta\varepsilon$), (b) width of the relaxation time distribution ($1 - \alpha$), (c) mean relaxation time (τ_0 , points) and dc resistance (R , full lines) *versus* inverse temperature.

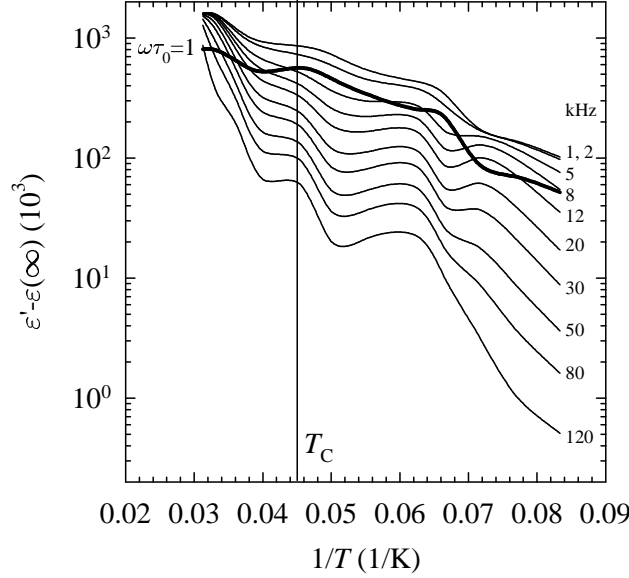


Fig. 4.8: The real part of the dielectric function *versus* the inverse temperature at a few representative frequencies. A full thick line represent the condition $\omega\tau_0 = 1$.

observed mode should be ascribed to the existence of the collective mode in the ground state. On the other hand, the width of the relaxation time distribution amounts to 1 at 32 K, quickly decreases to about 0.7 at 28 K and remains stable at this value down to 15 K. The broadness of the mode in the latter temperature region suggests that the collective mode is pinned to the randomly arranged impurities. However, below 15 K, $1 - \alpha$ narrows and the relaxation of the collective mode should be linked to regularly distributed structures. Finally, we observe that the behavior of the mean relaxation time points to two distinct dissipation regimes. Above the phase transition temperature, τ_0 follows the thermal activation of the resistance, while it saturates below that temperature.

In order to study dissipation regimes, it is also useful to present the temperature behavior of the real part of the dielectric function (Fig. 4.8). Obviously, two distinct dissipation regimes above and below T_C are characterized by different activation energies Δ

$$\varepsilon'(T) \propto \varepsilon' e^{-\frac{\Delta}{T}}. \quad (4.5)$$

$\Delta \approx 270$ K and $\Delta \approx 60$ K for $T > T_C$ and $T < T_C$, respectively.

5 Investigation of the superconducting state

5.1 Samples

5.1.1 κ -(BEDT-TTF)₂Cu[N(CN)₂]Br

Nine nominally pure single crystals of κ -(ET)₂Br, in shape of rhombic platelets with face areas between 0.42 and 2.15 mm² and thickness between 0.29 and 0.69 mm, were measured. The results for the last five of them were calibrated and analyzed in most detail and all showed qualitatively and quantitatively the same behavior. Samples originated from two different syntheses and had different resistivity ratios $RR(T_G/T_C)$ for similar cooling rates employed:

Crystals of the first synthesis, labeled as S1, had the resistivity ratio $RR(T_G/T_C) \approx 200$ (see Fig. 5.1) [24].

Crystals of the second synthesis, labeled as S2, had the resistivity ratio $RR(T_G/T_C) \approx 50$ (see Fig. 5.2) [9].

Here, the *resistivity ratio* is defined as

$$RR(T/T_C) = \frac{\rho(T)}{\rho_C}, \quad (5.1)$$

where ρ_C is the resistivity measured at temperature just above the SC transition.

Three different cooling procedures were used to cool samples from RT to 4.2 K. Special care was taken in the temperature region $60 \text{ K} < T < 100 \text{ K}$, where the relaxation processes appear (see Sec. 1.2.3 and Fig. 1.13). For the *quenched* (denoted as *Q*) state the sample was cooled down to liquid helium temperature in about 1 min, which represents an average speed of about -300 K/min over the whole temperature region. For the *relaxed* (denoted

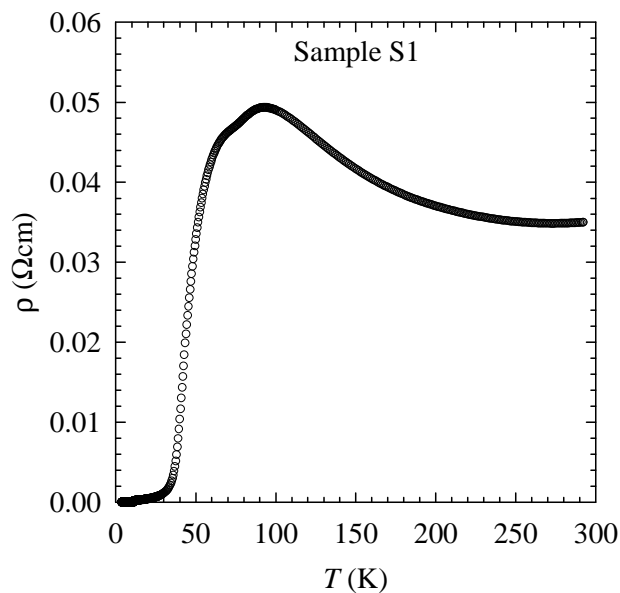


Fig. 5.1: Sample S1: Temperature dependence of resistance. [24]

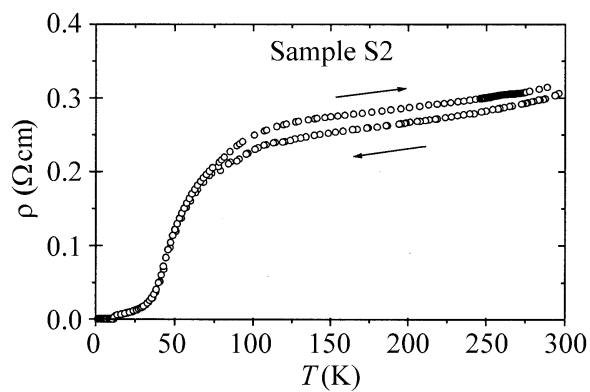


Fig. 5.2: Sample S2: Temperature dependence of resistivity in cooling and warming half-cycle. [9]

as *R*) state the sample was first cooled to 100 K in about 10 min. Between 60 K and 100 K the cooling rate was carefully monitored to amount to about -0.2 K/min. Below 60 K, the sample was finally cooled to 4.2 K in a few minutes. For the *annealed* state (denoted as *A*) the sample was cooled down to liquid nitrogen temperatures in about 1 h. Then it was kept between the liquid nitrogen temperature and 100 K for three days, mostly at temperatures in the vicinity of 80 K. Finally, it was cooled down to the liquid helium temperature in a few minutes.

5.1.2 κ -(BEDT-TTF)₂Cu(NCS)₂

Five nominally pure single crystals of κ -(ET)₂NCS, in shape of rhombic platelets with face areas between 0.61 and 2.29 mm² and thickness between 0.24 and 0.46 mm, were measured. The results for last two of them were calibrated and they both showed qualitatively and quantitatively the same behavior. Samples originated from two different syntheses:

Crystals of the first synthesis proved to be extremely sensitive to the degradation effects, failing to give reliable reproducible results. Therefore, no result can be presented on the basis of these measurements.

Crystals of the second synthesis were labeled as S3 and only preliminary measurements have been finished up to now.

Two different cooling procedures were used to cool samples from RT to 4.2 K. Special care was taken in the temperature region $40 \text{ K} < T < 80 \text{ K}$, where the relaxation processes appear (see Sec. 1.2.3 and Fig. 1.13). Note that the situation is somehow more complicated compared to the one for the κ -(ET)₂Br material, since the glass transition temperature region is lower and two glass transition temperatures are located within the region. For the *quenched* (denoted as *Q*) state the sample was cooled down to the liquid helium temperature in about 1 min, which represents an average speed of about -300 K/min over the whole temperature region. For the *relaxed* (denoted as *R*) state the sample was first cooled to 80 K in about 10 min. Between 40 K and 80 K the cooling rate was carefully monitored to amount to about -0.2 K/min. Below 40 K, the sample was finally cooled to 4.2 K in a few minutes.

A counterpart for the *annealed* state in κ -(ET)₂Br could not be yet established because of the experimental limitations. Namely, the majority of the glass transition temperature region lays below the liquid nitrogen temperature, where the stabilization and the maintenance of the temperature is

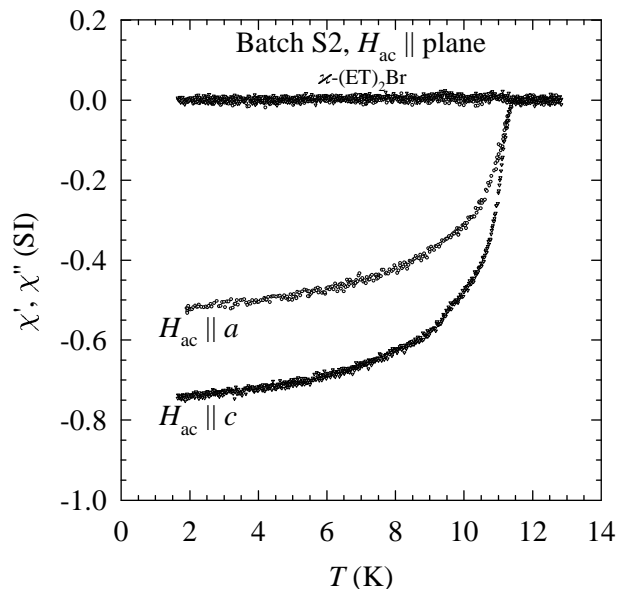


Fig. 5.3: Batch S2: real and imaginary parts of the susceptibility in two distinct directions in the $H_{ac} \parallel$ plane geometry.

complicated. Further, this temperature region embodies two glass transition temperatures, so a very long maintenance of the fixed temperature in the vicinity of the lower limit of this region might not be successful. Indeed, preliminary annealing measurements holding the sample at fixed temperatures of 45 K and 50 K for four hours showed that the relaxation effect was smaller compared to the relaxed cooling in the *whole* temperature region for the same period of time. We conclude that a very slow sweep for several days between 80 and 40 K should be performed in order to obtain a counterpart of the annealed state. However, the requirement for a slow drift below the liquid nitrogen temperature for several days presents an enormous problem in the present experimental conditions.

5.2 Complex susceptibility

We present the behavior obtained in two principal field geometries: that is, the $H_{ac} \perp$ plane and the $H_{ac} \parallel$ plane, as defined in Sec. 3.2. For two κ -(ET)₂Br samples measurements were also performed for two distinct directions in the $H_{ac} \parallel$ plane geometry, that is the magnetic field was aligned to the a and c crystallographic axes (Fig. 5.3). The χ' response in these two orientations was different, which confirms that the field penetration along the l_{out} direction and not the one along the l_{in} direction, dominates the sus-

ceptibility of the sample [see Eq. (3.12)]. Further, we point out that the λ_{out} results obtained for both field orientations were mutually consistent, so we conclude that the specific orientation within the ac plane does not influence the results. It should be also noted that this test measurement was performed only in fast cooling conditions, which corresponds best to the Q state. However, as it can be seen from the Table 5.2, the ratio $\lambda_{\text{out}}/\lambda_{\text{in}}$ for R and A states is even much larger than the one for the Q state, so our conclusions are valid for the former two states as well. Therefore, in all further measurements we have always made sure that in the $H_{\text{ac}} \parallel$ plane geometry the field was aligned with the largest dimension of the platelet face in order to minimize the demagnetization factor.

Our first important result concerns the influence of the cooling rate on the components of the complex susceptibility in the SC state as a function of the synthesis procedure. The susceptibility data obtained for the sample S1 for two different cooling rates are shown in Fig. 5.4. We identify the R state as the *ground state*. In the ground state, superconductivity sets in at 12.0 K and 11.5 K for the $H_{\text{ac}} \perp$ plane and the $H_{\text{ac}} \parallel$ plane geometry, respectively. For the $H_{\text{ac}} \perp$ plane geometry the sample response is almost completely diamagnetic, while for the $H_{\text{ac}} \parallel$ plane geometry the susceptibility is somewhat smaller in magnitude. Our results point to a huge effect of the cooling rate on the susceptibility value and T_{C} . When the sample was cooled faster, the absolute value of the susceptibility was smaller and T_{C} lower. In other words, the diamagnetic region shrinks in the χ' versus T plot. This huge effect is especially emphasized for the $H_{\text{ac}} \parallel$ plane geometry, where the absolute χ' value is almost an order of magnitude smaller for the Q state than for the R state.

The susceptibility data obtained for the sample S2 for three different cooling rates are presented in Fig. 5.5. The first feature, reflecting different sample quality, is that the ground state, characterized as before by an almost complete diamagnetic response, is established in the A state, and not, as in the case of the sample S1, in the R state. For the purpose of clarity, we will refer to the R state of the sample S2 as the *intermediate state*¹. The anisotropy of the susceptibility in the ground state is somewhat larger for sample S2 than for sample S1. The second feature is that the cooling rate effect on the susceptibility value is much smaller for sample S2 compared with the effects obtained for sample S1 (see Fig. 5.4). We can qualitatively describe this effect using the definition of the *cooling rate sensitivity* ξ , which is the ratio of the absolute susceptibility values for the Q state and the R state

¹This state should not, by any means, be identified with the historical notion of the intermediate state in superconductors (Ref. 71).

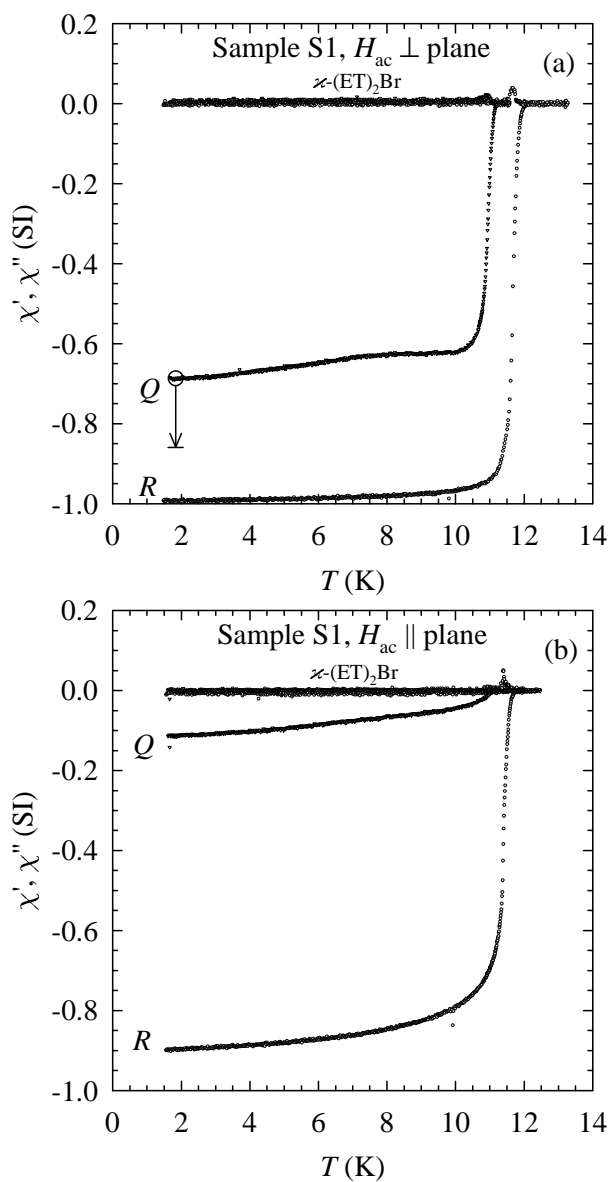


Fig. 5.4: Sample S1: real and imaginary parts of the susceptibility for relaxed (R) and quenched (Q) states in the (a) $H_{ac} \perp$ plane and (b) $H_{ac} \parallel$ plane geometry. The arrow in (a) illustrates the upper limit of the systematic error.

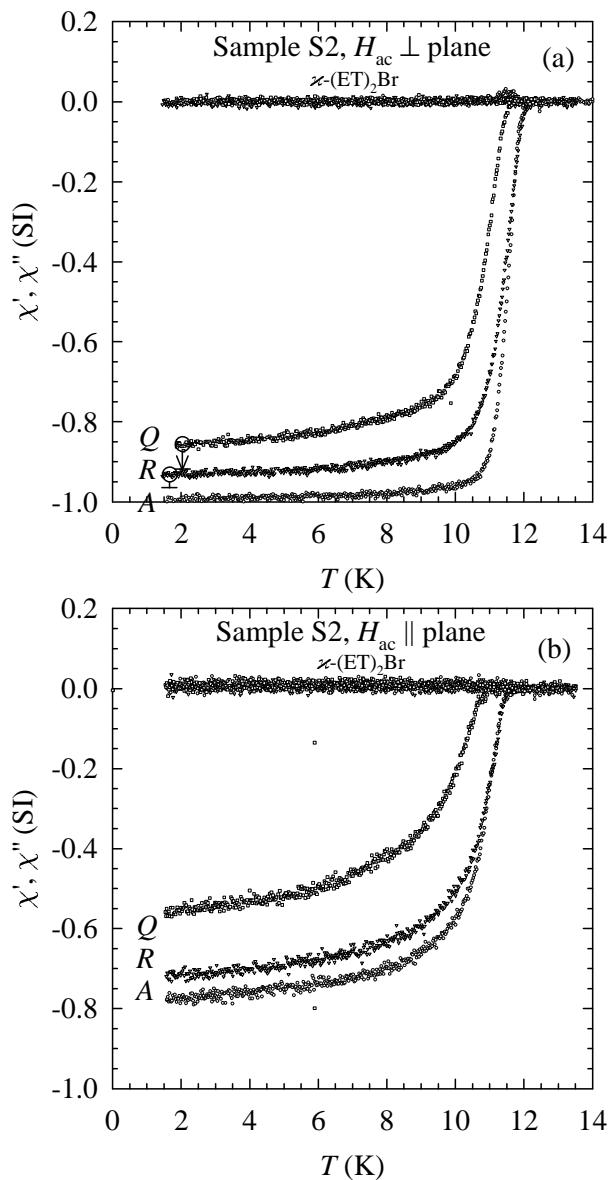


Fig. 5.5: Sample S2: real and imaginary parts of the susceptibility for annealed (A), relaxed (R), and quenched (Q) states in the (a) $H_{ac} \perp$ plane and (b) $H_{ac} \parallel$ plane geometry. The arrows in (a) illustrate the upper limit of the systematic error.

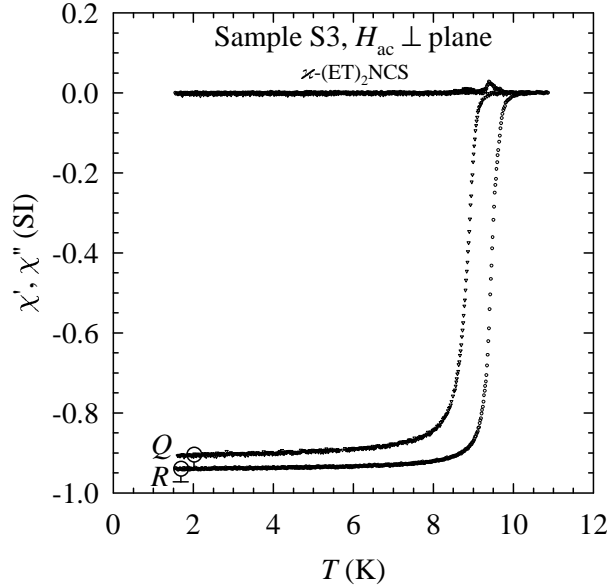


Fig. 5.6: Sample S3: real and imaginary parts of the susceptibility for relaxed (R) and quenched (Q) states in the $H_{ac} \perp$ plane geometry. The error bars illustrate the upper limit of the systematic error.

at the lowest measured temperatures

$$\xi = \frac{\chi'(T_{\min}, Q \text{ state})}{\chi'(T_{\min}, R \text{ state})}. \quad (5.2)$$

Obviously, smaller ξ means larger cooling rate sensitivity. For samples S1 and S2 for the $H_{ac} \perp$ plane geometry we get $\xi = 0.69$ and $\xi = 0.92$, respectively.

The susceptibility data obtained for the sample S3 for two different cooling rates are presented in Fig. 5.6. Only one geometry is shown, as the sample disintegrated into pieces, when the change of orientation was attempted. The presented results are therefore the only available results for the κ -(ET)₂NCS material so far. First note that the state with lower degree of disorder, the R state, did not show almost full diamagnetism, which leads to the conclusion that the ground state was not established. However, the obtained results give us the possibility to calculate the cooling rate sensitivity $\xi = 0.97$, which is even smaller than the one of the sample S2. Both facts suggest, by analogy with the sample S2, that slower cooling (e.g., annealed state) could further decrease the degree of the disorder and increase the absolute value of susceptibility, giving the results in accordance with the ground states of samples S1 and S2. Indeed, here for the R state $\chi' = -0.93$, and such scenario seems

State	$H_{ac} \perp$ plane		$H_{ac} \parallel$ plane	
	χ'	T_C (K)	χ'	T_C (K)
Sample S1				
<i>R</i>	-0.99	12.0	-0.90	11.5
<i>Q</i>	-0.68	11.2	-0.12	10.5
Sample S2				
<i>A</i>	-0.99	12.0	-0.78	11.5
<i>R</i>	-0.93	12.0	-0.72	11.5
<i>Q</i>	-0.86	11.4	-0.57	10.5

Table 5.1: Susceptibility properties, as defined in the text, for (i) sample S1 in the relaxed (ground) and quenched states, and (ii) sample S2 in the annealed (ground), relaxed (intermediate), and quenched states.

reasonable. However because of experimental limitations we haven't been able to check this hypothesis yet. Since we believe that the ground state was not established, and since the results involve only one sample geometry, no further conclusion will be drawn or analysis made from the presented result.

Finally, we point out that the $\chi''(T)$ component was negligible, clearly indicating that all three measured samples were in the Meissner state. For clarity, the most important susceptibility properties presented in this Section are summarized in Table 5.1. The differences in T_C between two samples are within the experimental error.

5.2.1 Anomalies in complex susceptibility

Before proceeding to the penetration depth considerations, it would be interesting to show some complex susceptibility results, which are not reproducible, however they point to a strong domain behavior in the measured samples. Interesting effects, which occasionally appeared regardless of the field orientation and the sample synthesis are small susceptibility jumps, as shown in Fig. 5.7. Sometimes these jumps are reversible, as shown in the situation (b), where one reduction is annihilated by two enhancements of the susceptibility. Jumps can also be irreversible, as shown in the situation (a), where only one reduction of the susceptibility appears.

The second interesting effect that was observed only once, but which persisted for several hours of measurement – even after the sample was warmed to RT and quenched back to the liquid helium temperature – is shown in Fig. 5.8. The temperature dependence of susceptibility appeared as expected in almost the whole temperature region. However, above the

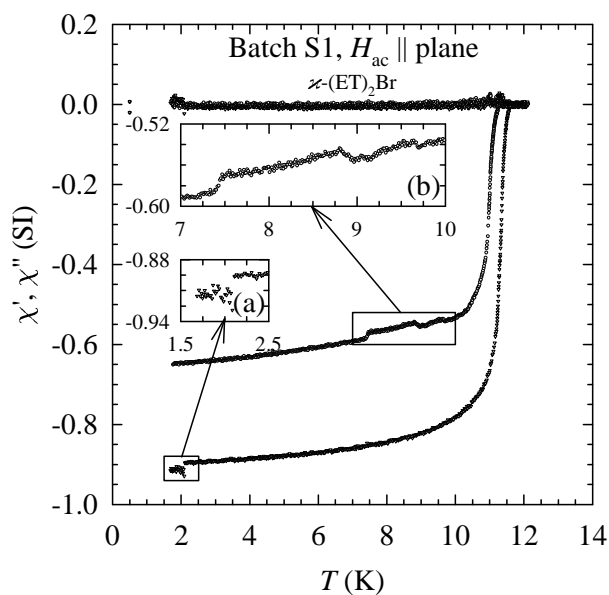


Fig. 5.7: A sample from batch S1: Small jumps in susceptibility for two different cooling rates (a) -0.1 K/min and (b) -100 K/min. Inserts enlarge the range of the greatest interest.

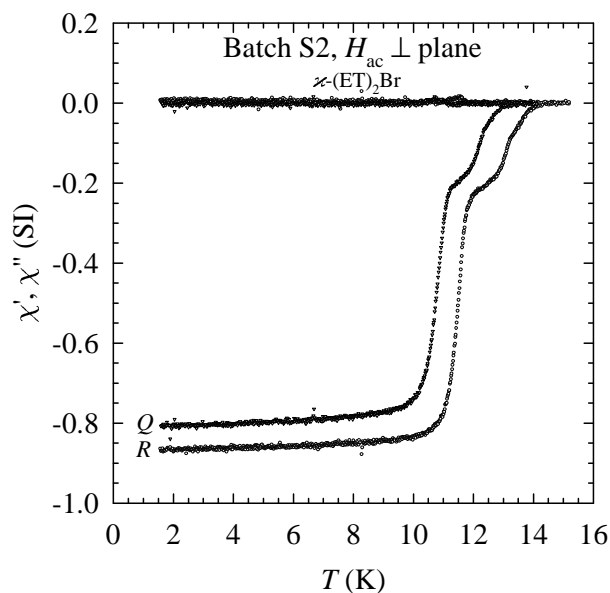


Fig. 5.8: A sample from batch S2: The residual superconductivity in the part of the sample in the temperature region 11–14 K.

expected $T_C = 12.0, 11.2$ K, for R - and Q -states, respectively, the residual diamagnetism appears and persists in the additional temperature region of 2 K. Comparing the full susceptibility of the sample and the residual susceptibility, one can argue that about 25% of the sample remains in the superconducting state even above the expected T_C .

It should be stressed that we were unable to explain these peculiar effects with the influence of some systematic error in the experimental setup.

5.3 Penetration depth

Our second important result concerns the temperature dependence of λ_{in} and λ_{out} as a function of the synthesis procedure in the ground state. In Figs. 5.9 and 5.10 we show the influence of the cooling rate on the anisotropic penetration depth as a function of the sample quality. Note that in the ground state of both samples S1 and S2 the temperature dependence of λ_{in} and λ_{out} at temperatures below about 5 K is well described by the T and T^2 law, respectively. The upper bound of the fit range (5 K) is given by the general requirement that the genuine low-temperature behavior of the penetration depth is strictly obeyed only far from the critical region close to T_C . The solid lines correspond to the calculated fit to the power-law behavior in the temperature range $1.6 \text{ K} < T < 5 \text{ K}$

$$\lambda_{\text{in}} = k_{\text{in}} \left(\frac{T}{T_C} \right) + \lambda_{\text{in}}(0), \quad (5.3)$$

$$\lambda_{\text{out}} = k_{\text{out}} \left(\frac{T}{T_C} \right)^2 + \lambda_{\text{out}}(0). \quad (5.4)$$

We get $k_{\text{in}} = 5.2 \mu\text{m}$, $\lambda_{\text{in}}(0) = 1.5 \pm 0.5 \mu\text{m}$, $k_{\text{out}} = 56 \mu\text{m}$, $\lambda_{\text{out}}(0) = 53 \pm 10 \mu\text{m}$ and $k_{\text{in}} = 2.8 \mu\text{m}$, $\lambda_{\text{in}}(0) = 1.1 \pm 0.4 \mu\text{m}$, $k_{\text{out}} = 69 \mu\text{m}$, $\lambda_{\text{out}}(0) = 85 \pm 10 \mu\text{m}$ for S1 and S2, respectively. The penetration depth values at 0 K, $\lambda(0)$, observed in the ground states of both samples, are in very good accordance with values for the penetration depths given in the literature.

Special attention should be given to the *relative change of the penetration depth* $\eta(T)$ at low temperatures,

$$\eta(T) = \frac{\lambda(T) - \lambda(0)}{\lambda(0)}. \quad (5.5)$$

We denote the deviation of $\lambda_{\text{in}}(T)$ and $\lambda_{\text{out}}(T)$ from their values at 0 K, in units of $\lambda(0)$, as $\eta_{\text{in}}(T)$ and $\eta_{\text{out}}(T)$, respectively. We find that $\eta_{\text{in}}(5 \text{ K}) = 1.4$,

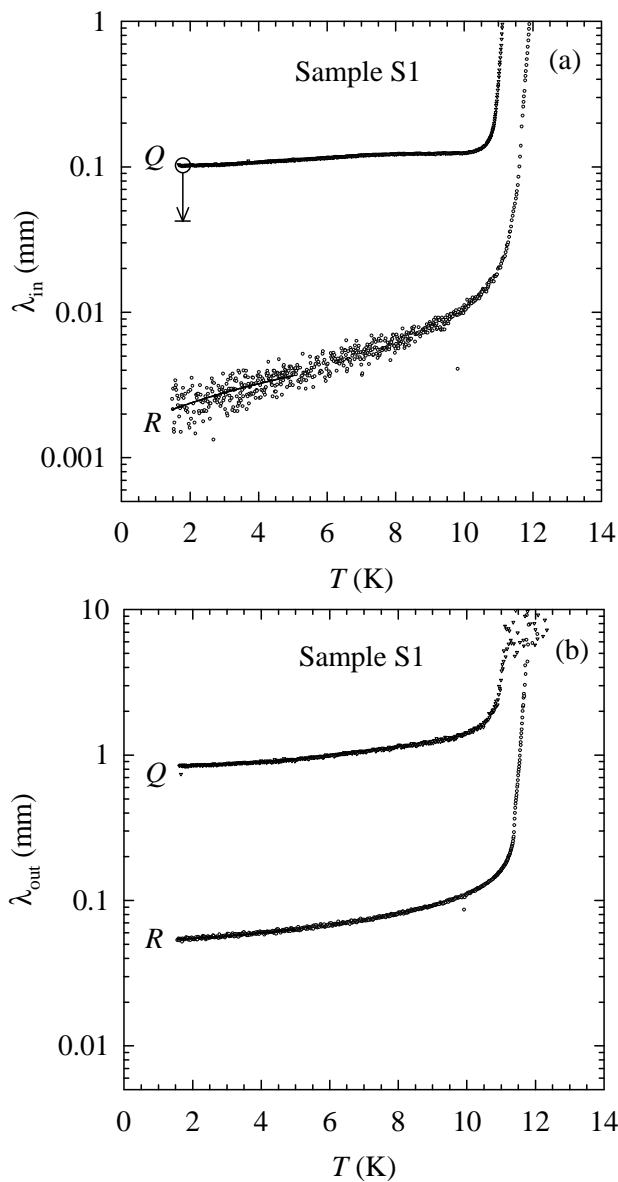


Fig. 5.9: Sample S1: (a) in-plane and (b) out-of-plane penetration depths for relaxed (R) and quenched (Q) states. Solid lines represent the fit to the power-law behavior, while the arrow in (a) illustrates the upper limit of the systematic error.

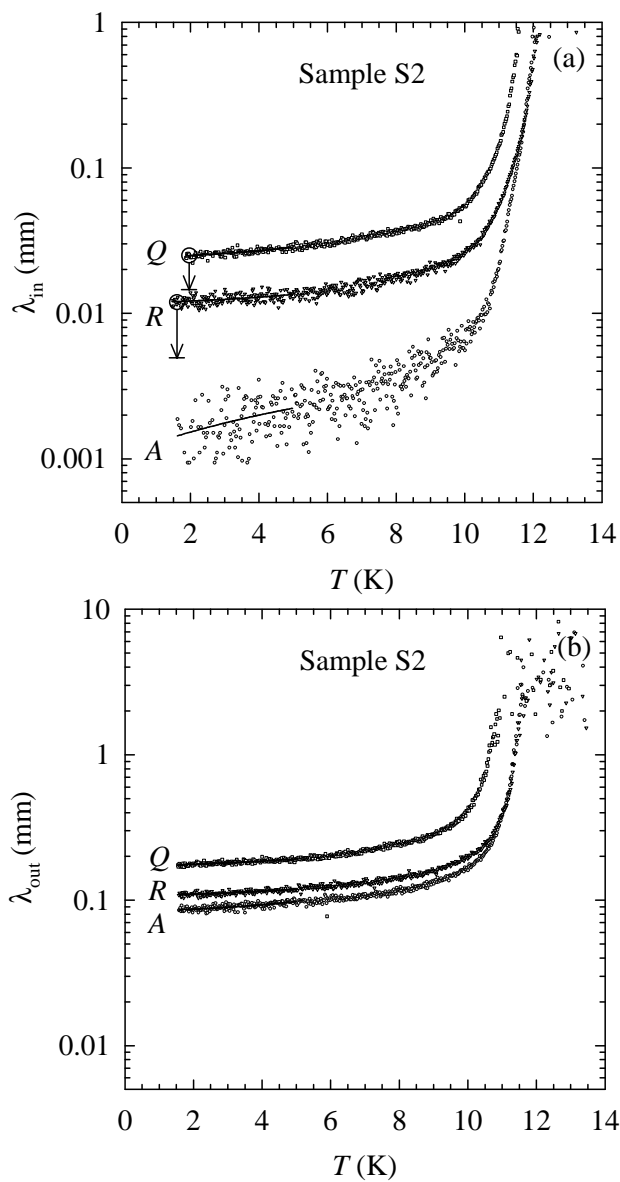


Fig. 5.10: Sample S2: (a) in-plane and (b) out-of-plane penetration depths for annealed (A), relaxed (R), and quenched (Q) states. Solid lines represent the fit to the power-law behavior, while the arrows in (a) illustrate the upper limit of the systematic error.

$\eta_{\text{out}}(5 \text{ K}) = 0.19$ and $\eta_{\text{in}}(5 \text{ K}) = 1.1$, $\eta_{\text{out}}(5 \text{ K}) = 0.15$ in the ground state of samples S1 and S2, respectively. First we note that η values are in perfect accordance for both samples, confirming that they are in the same – ground – state. Second, a difference between η_{in} and η_{out} values for almost one order of magnitude proves a strong anisotropy in physical properties between the two orientations. This also confirms our choice for the exponent in the power-law in Eqs. (5.3) and (5.4).

Finally, our third important result concerns the intermediate state (R state in sample S2), for which we get $\eta_{\text{in}}(5 \text{ K}) = 0.13$, $\eta_{\text{out}}(5 \text{ K}) = 0.10$. Unlike for the ground state, the temperature dependencies of λ_{in} and λ_{out} are so similar that they cannot any longer be described by different power laws as it was the case in the ground state. The obvious solution is to try to fit both penetration depths to the T^2 power-law behavior

$$\lambda_{\text{in}} = k_{\text{in}} \left(\frac{T}{T_C} \right)^2 + \lambda_{\text{in}}(0), \quad (5.6)$$

$$\lambda_{\text{out}} = k_{\text{out}} \left(\frac{T}{T_C} \right)^2 + \lambda_{\text{out}}(0), \quad (5.7)$$

which, as it will be discussed in Sec. 6.4, suggests a d -wave superconductor with impurities. We get $k_{\text{in}} = 9.2 \mu\text{m}$, $\lambda_{\text{in}}(0) = 12 \pm 6 \mu\text{m}$, and $k_{\text{out}} = 58 \mu\text{m}$, $\lambda_{\text{out}}(0) = 110 \pm 20 \mu\text{m}$. We point out that the fit to the s -wave model describes our data almost equally well (see Sec. 5.4). On the other hand, the s -wave model fails completely for the penetration depth temperature dependencies in the ground state of both samples S1 and S2.

Now we comment on the penetration depth results for the Q state. We find that $\eta_{\text{in}}(5 \text{ K}) = 0.11$, $\eta_{\text{out}}(5 \text{ K}) = 0.12$ and $\eta_{\text{in}}(5 \text{ K}) = 0.16$, $\eta_{\text{out}}(5 \text{ K}) = 0.10$ for samples S1 and S2, respectively. Here we apply the same arguments as in the case of the intermediate state and fit both λ_{in} and λ_{out} to the T^2 power-law behavior [Eqs. (5.6) and (5.7)]. We get $\lambda_{\text{in}}(0) = 100 \pm 50 \mu\text{m}$, $\lambda_{\text{out}}(0) = 830 \pm 100 \mu\text{m}$, and $\lambda_{\text{in}}(0) = 24 \pm 12 \mu\text{m}$, $\lambda_{\text{out}}(0) = 170 \pm 20 \mu\text{m}$ for sample S1 and S2, respectively. The fact that these fits describe well the penetration depth data again suggests a d -wave superconductor with impurities. Further, it should be noted that (i) $\lambda(0)$ values are larger for the Q state than for the intermediate state, suggesting a larger disorder in the former state, and (ii) $\lambda(0)$ values for the sample S1 are significantly larger than the ones for S2, suggesting a significantly larger disorder in the former sample in the Q state. Finally, the result that $\lambda_{\text{out}}(0)$ for the sample S1 is close to the crystal size indicates that the bulk superconductivity is not established, allowing us to define the boundary between bulk and non bulk SC at $\chi' = -0.7$ for the $H_{\text{ac}} \perp$ plane geometry.

State	$H_{ac} \perp$ plane			$H_{ac} \parallel$ plane		
	$\lambda_{in}(0)$ (μm)	k_{in} (μm)	$\eta_{in}(5\text{ K})$	$\lambda_{out}(0)$ (μm)	k_{out} (μm)	$\eta_{out}(5\text{ K})$
Sample S1						
R	1.5 ± 0.5	5.2	1.4	53 ± 10	56	0.19
Q	100 ± 50	60	0.11	830 ± 100	480	0.12
Sample S2						
A	1.1 ± 0.4	2.8	1.1	85 ± 10	69	0.15
R	12 ± 6	9.2	0.13	110 ± 20	58	0.10
Q	24 ± 12	22	0.16	170 ± 20	88	0.10

Table 5.2: Penetration depth properties, as defined in the text, for (i) sample S1 in the relaxed (ground) and quenched states, and (ii) sample S2 in annealed (ground), relaxed (intermediate), and quenched states.

For clarity, the most important results of the penetration depth properties presented in this Section are summarized in Table 5.2.

5.4 Superfluid density

In the following, we address the temperature dependance of the superfluid density in order to get the information on the symmetry of the superconducting state. Note that, as explained in Sec. 3.5, T_C and $\lambda(0)$ are obtained independently by the ρ_s analysis. Except for $\lambda(0) = 1.8 \mu\text{m}$ [compared to $\lambda(0) = 1.5 \mu\text{m}$ in the previous section] for the R state in the sample S1, penetration depth values obtained this way match perfectly to the ones obtained by the direct fit to the penetration depth data.

$\rho_{s,in}$ and $\rho_{s,out}$ for the ground state of the sample S1 (established in the R state) and for the ground state of the sample S2 (established in the A state) as a function of the reduced temperature $t = T/T_C$ are displayed in Figs. 5.11 and 5.12, respectively. There is a strong resemblance in the behavior found for both samples. Note that the leading terms, which describe the low-temperature behavior, are the T and T^2 terms for $\rho_{s,in}$ and $\rho_{s,out}$, respectively. This is to be expected, because T and T^2 terms describe the low-temperature behavior of the λ_{in} and λ_{out} in the ground state. If we fit the superfluid density data in the whole temperature region below T_C , as described in Sec. 3.5, we finally obtain for the sample S1

$$\rho_{s,in} = 1 - 1.95t + 1.45t^3 - 0.09t^4 - 0.41t^5, \quad (5.8)$$

$$\rho_{s,out} = 1 - 1.88t^2 - 0.73t^3 + 4.47t^4 - 2.86t^5, \quad (5.9)$$

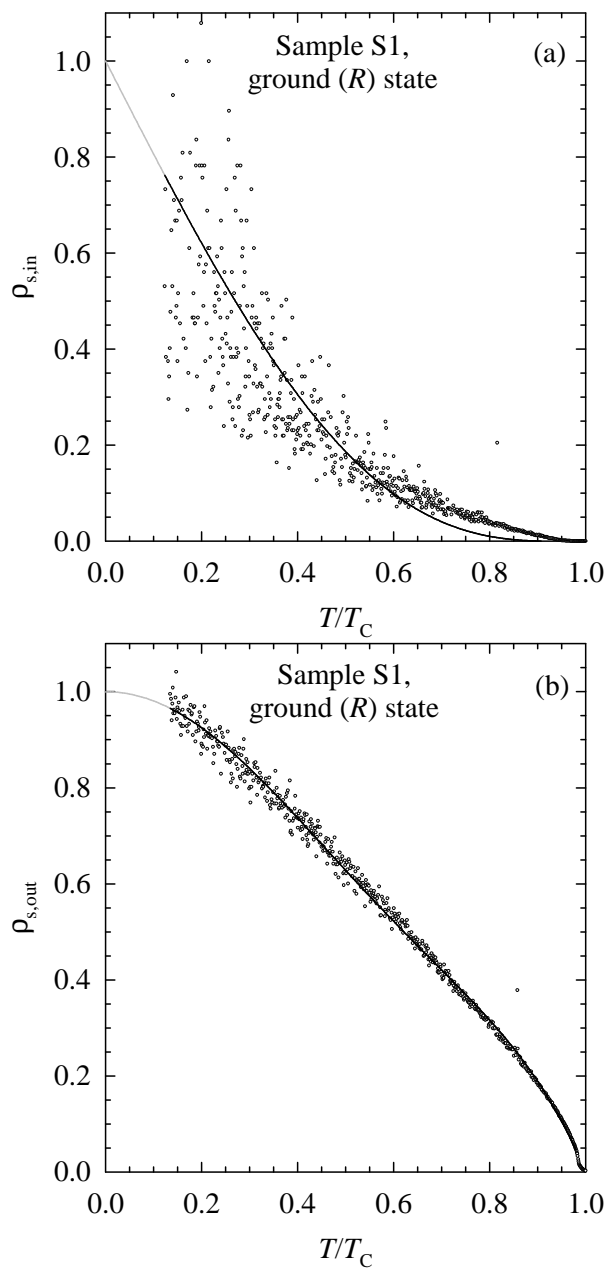


Fig. 5.11: Sample S1: (a) in-plane and (b) out-of-plane superfluid densities for the ground (R) state. Solid line is a fit to the polynomial expression. A large noise in $\rho_{s,in}$ is due to small values of $\lambda_{in}(0)$ (see text).

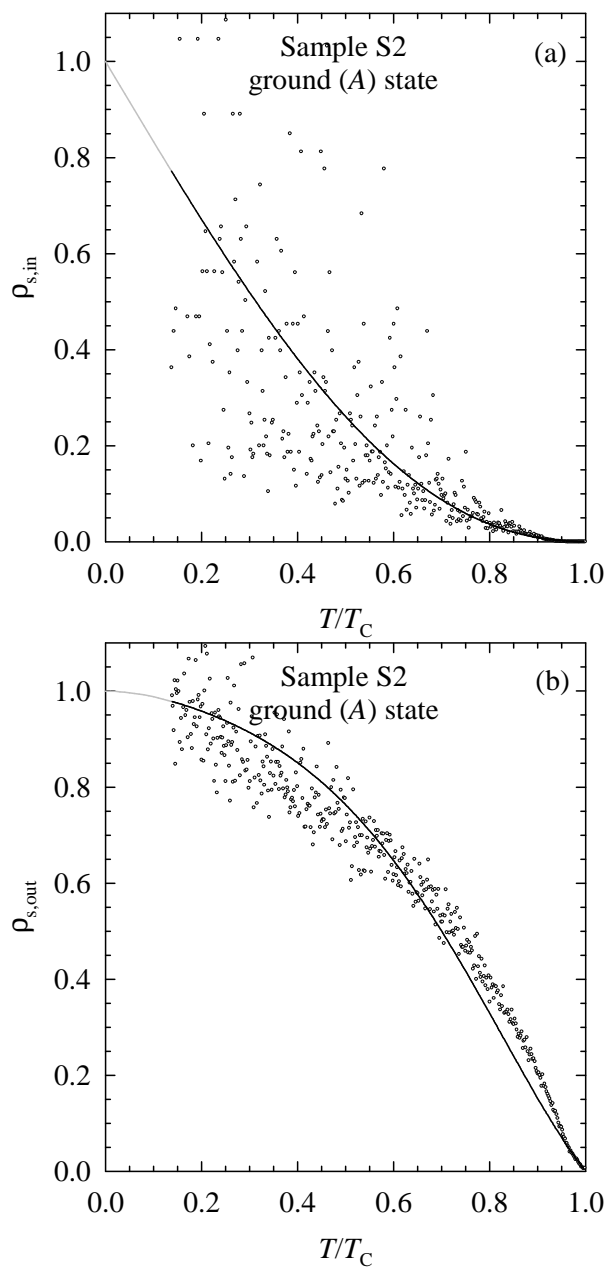


Fig. 5.12: Sample S2: (a) in-plane and (b) out-of-plane superfluid densities for the ground (A) state. Solid line is a fit to the polynomial expression. A large noise in $\rho_{s,in}$ is due to small values of $\lambda_{in}(0)$ (see text).

and for the sample S2

$$\rho_{s,\text{in}} = 1 - 1.68t + 0.78t^3 + 0.16t^4 - 0.26t^5, \quad (5.10)$$

$$\rho_{s,\text{out}} = 1 - 1.45t^2 + 2.98t^3 - 5.38t^4 + 2.84t^5. \quad (5.11)$$

Taking into account a relatively large experimental error in the penetration depth values (see Figs. 5.9 and 5.10), the leading coefficient values might be considered to be almost the same. In addition to the systematic error, there is also a noise, which is a mere consequence of the fact that $\rho_{s,\text{in}}$ is calculated according to the expression $\rho_{s,\text{in}}(T) = [\lambda_{\text{in}}(0)/\lambda_{\text{in}}(T)]^2$, so that the absolute noise in $\rho_{s,\text{in}}$ is proportional to the relative noise in the penetration depth data. That implies a larger noise for smaller values of $\lambda_{\text{in}}(0)$, which becomes substantial for $\lambda_{\text{in}}(0)$ of the order of $1 \mu\text{m}$. Finally, we point out that the shapes of curves for the in-plane and out-of-plane penetration depths in the ground state are qualitatively different from the s -wave dependence.

Further we want to correlate the presented results with the results obtained by an alternative (now obsolete) method. If the *improved* calibration is not used in the $H_{\text{ac}} \perp$ plane geometry, λ_{in} and $\rho_{s,\text{in}}$ dependencies are obtained using Eq. (3.15), as described in Secs. 3.4 and 3.5. In Fig. 5.13 $\rho_{s,\text{in}}$ in the ground states of sample S1 and S2 are displayed, using the $\lambda_{\text{in}}(0)$ value obtained by our *improved* calibration, that is $\lambda_{\text{in}}(0) = 1.1 \mu\text{m}$ and $1.8 \mu\text{m}$, respectively. The obtained results are quantitatively the same as those presented in Figs. 5.11 and 5.12, that is the behavior is strongly linear. Even more, if we check the obtained fits,

$$\rho_{s,\text{in}}(\text{sample 1}) = 1 - 1.69t + 0.78t^3 + 0.19t^4 - 0.28t^5, \quad (5.12)$$

$$\rho_{s,\text{in}}(\text{sample 2}) = 1 - 1.54t + 1.03t^3 - 0.89t^4 + 0.40t^5, \quad (5.13)$$

we see that the leading coefficients differ from those in Eqs. (5.8) and (5.10) within the experimental error.

We used this method [using $\lambda_{\text{in}}(0)$ values from the literature] in our first publication on the superconductivity state investigations in this material [64]. In this case an important question arises as to which $\lambda_{\text{in}}(0)$ value should be used. This is of primary interest, since the $\lambda_{\text{in}}(0)$ choice influences significantly the low-temperature $\rho_{s,\text{in}}$ behavior. We can see that if we expand the $\rho_{s,\text{in}}$ expression at low temperatures,

$$\rho_{s,\text{in}}(t) = \left(\frac{\lambda_{\text{in}}(0)}{\lambda_{\text{in}}(0) + k_{\lambda}t} \right)^2 \approx 1 - 2 \frac{k_{\lambda}}{\lambda_{\text{in}}(0)} t,$$

it is obvious that both the $\lambda_{\text{in}}(0)$ value, as well as the relative behavior of λ_{in} *significantly* influence the $\rho_{s,\text{in}}$ behavior and as a consequence also change the

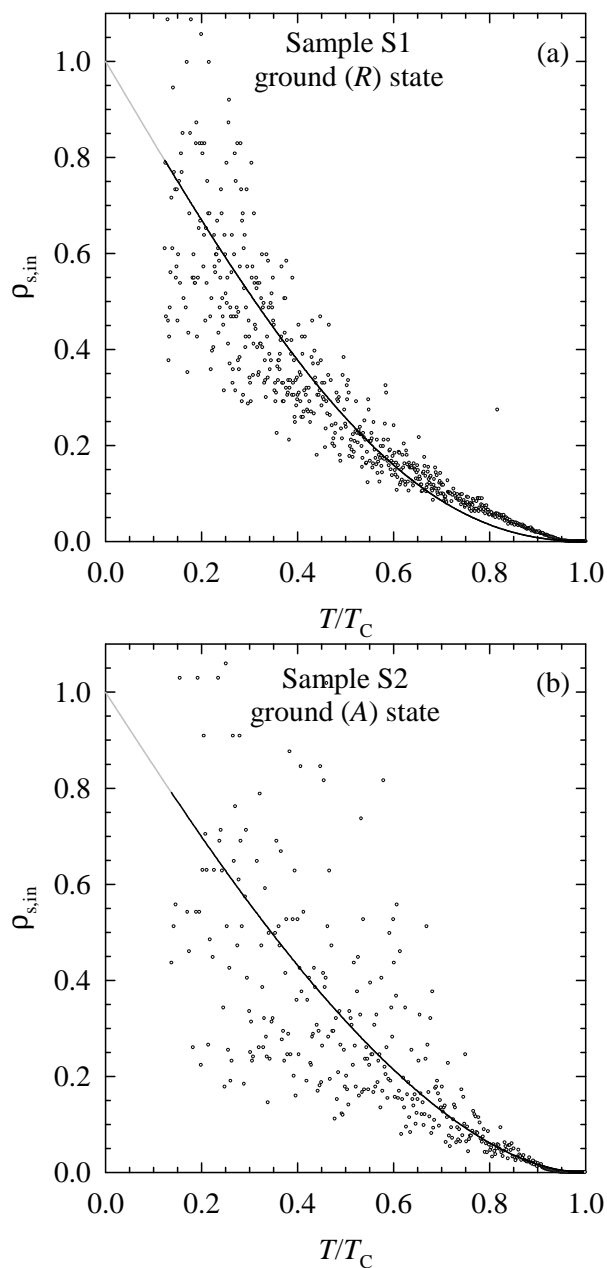


Fig. 5.13: In-plane superfluid density for the ground state of (a) sample S1 and (b) sample S2 without using the *improved* calibration but rather Eq. (3.15) and the same $\lambda(0)$ values.

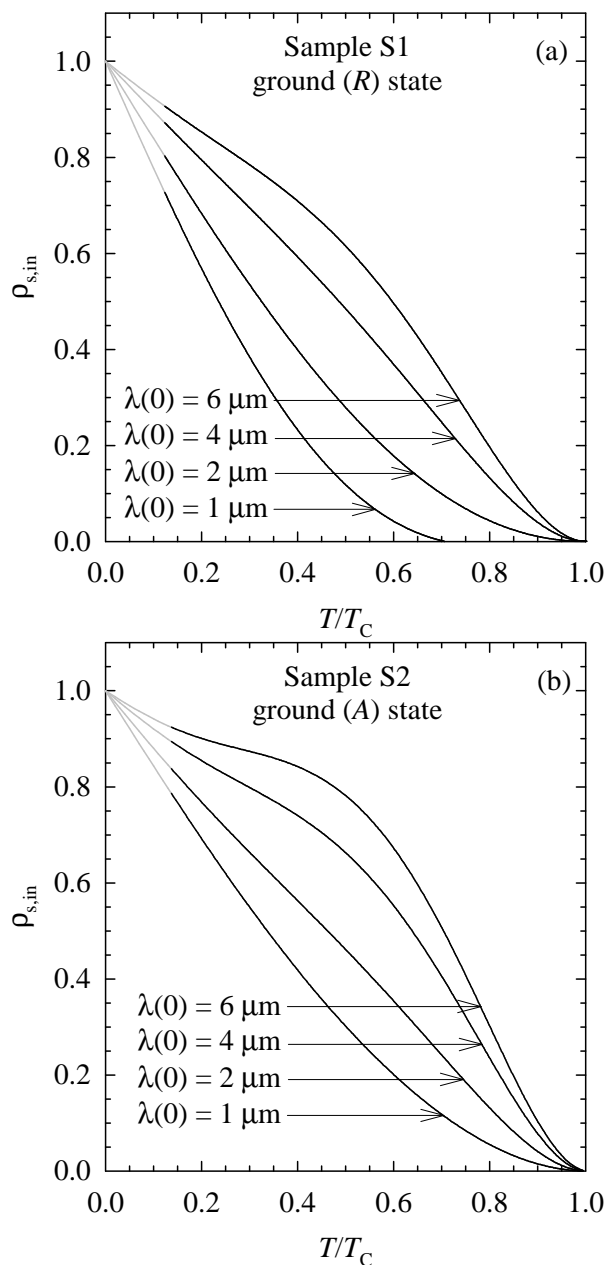


Fig. 5.14: In-plane superfluid density for the ground state of (a) sample S1 and (b) sample S2 using Eq. (3.15) and a few chosen $\lambda(0)$ values.

value of the leading coefficient. This fact is demonstrated for a few chosen $\lambda_{\text{in}}(0)$ values in Fig. 5.14, where the same experimental data as in Fig. 5.13 were used. Despite of the fact that it is obvious that the $\lambda_{\text{in}}(0)$ influence is significant, our primary conclusion does not change. Namely if we use $\lambda_{\text{in}}(0)$ from the literature, $0.5 \mu\text{m} < \lambda_{\text{in}}(0) < 2 \mu\text{m}$, we shall obtain a strong linear behavior with the leading coefficient of order of 1 or larger.

Finally, the behavior for the in-plane $\rho_{\text{s,in}}$ and out-of-plane $\rho_{\text{s,out}}$ superfluid densities for the intermediate state of the sample S2 (established in the R state) is displayed in Fig. 5.15. They were obtained in the same way as the results in the beginning of this Section by the use of the *improved* calibration. Here, the $\rho_{\text{s,in}}$ data are insensitive to the systematic error at low temperatures, since the correction for λ_{in} drops out from the expression for $\rho_{\text{s,in}}$. Note that the leading term, describing the low-temperature behavior, is the T^2 term for both the in-plane and out-of-plane superfluid densities:

$$\rho_{\text{s,in}} = 1 - 1.69t^2 + 2.77t^3 - 5.05t^4 + 2.97t^5, \quad (5.14)$$

$$\rho_{\text{s,out}} = 1 - 1.02t^2 + 1.34t^3 - 2.50t^4 + 1.18t^5. \quad (5.15)$$

As it will be shown in Sec. 6.4, this situation agrees well with the impurity scattering in the unitary limit. In order to demonstrate the fact that the superfluid density behavior in the intermediate state is also rather close to the dependence expected for the s -wave order parameter behavior, the s -wave model dependence is added as a dashed line for both orientations.

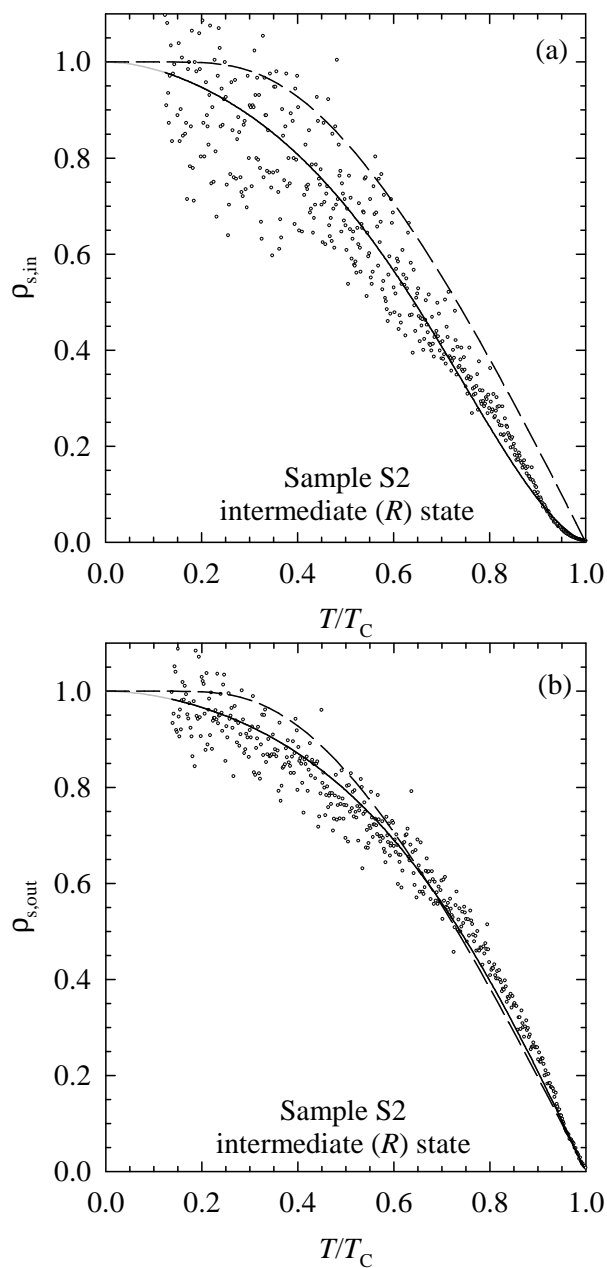


Fig. 5.15: Sample S2: (a) in-plane and (b) out-of-plane superfluid densities for the intermediate (R) state. The solid line is a fit to the polynomial expression, and the dashed line presents the s -wave model (see the text).

6 Discussion

6.1 Insulating spin density wave state

Previous magnetic measurements have shown that in κ -(ET)₂Cl, below the phase transition temperature $T_C = 22$ K, a commensurate spin density wave with a very small canting of spins is stabilized [6]. The anti-ferromagnetic spins are canted by an angle of 6×10^{-2} degrees from the b -axis in such a way that the vector of the ferromagnetic moment is aligned along the c -axis. The ferromagnetic crystal is naturally divided into domains with equivalent spin configurations. The measured magnetic moment per spin amounts to $0.4 - 1.0\mu_B$ /dimer [30], which is much larger than the value of $0.08 \mu_B$ /molecule observed in the case of the spin density wave in (TMTSF)₂PF₆, which is formed by itinerant spins [31] and therefore indicates the strong electron localization.

An important indication of the existence of the collective conductivity channel, associated with the spin density wave, is given by the increase of the conductivity above a finite electrical threshold field. At about 13 K, the electrical threshold field has a minimum value. Its increase toward the temperature of phase transition can be understood in the frame of the standard model of the sliding spin density wave, weakly pinned to randomly distributed impurities [69]. On the other hand, the increase of the electrical threshold field toward lower temperatures, with a concomitant rapid increase of the collective conductivity, cannot be explained in terms of the model for the spin density wave sliding. We argue that the spin density wave sliding mechanism is replaced by a new mechanism of the collective conduction.

Further confirmation of a new mechanism is given by the behavior of the parameters of the complex dielectric function. In particular, dielectric strength is of the order of 10^3 and it decreases with the decreasing of the temperature. This is in contradiction with the behavior observed in the case of the spin density wave in the Bechgaard salts, where the phason is a relaxation entity [72]. In the latter material $\Delta\varepsilon$ is of order of 10^9 and temperature independent. Therefore, we propose that in κ -(ET)₂Cl a charged domain

wall pair, connected to ferromagnetic domains, is the relaxation entity. Further, the $(1 - \alpha) \approx 0.75$ indicates a random ferromagnetic domain structure in the temperature region $13 \text{ K} < T < T_C$. The observation that below 13 K mode narrows, that is $(1 - \alpha)$ approaches 1, reveals a progressive restoration of a regular ferromagnetic domain structure at low temperatures. We suggest that above 13 K domains are numerous, and charged domain walls are pinned to randomly arranged impurities. By lowering the temperature, domains grow in size and below about 13 K become so large, that they stretch over a larger number of impurities. Consequently, their shape and distribution, as well as the distribution of domain walls becomes regular, as it is no longer related to the distribution of impurities. In the whole temperature region, the number of domain walls decreases concomitantly with the temperature decrease, which explains the gradual decrease of the relaxation strength value.

In the fluctuation region above T_C , the mean relaxation time is activated with the single particle activation energy $\Delta \approx \Delta_{fc} \approx 270 \text{ K}$ showing that the free-carrier screening is effective. However, below T_C the temperature independent behavior of τ_0 indicates a substantial reduction of the free-carrier screening in the ground state. Indeed, the free-carrier density below T_C , estimated on the basis of the resistance increase between room temperature and T_C , and allowing the electron to move inside a 2D plane, turns out to be smaller than the one electron per domain wall characteristic length $L_{\text{wall}} \approx 0.1 - 1 \mu\text{m}$. The latter might be also obtained from the theoretical expression which relates L_{wall} and E_T [73, 74]. These two distinct dissipation regimes (above and below T_C , which coincides with the crossover temperature T_C) are reflected in the behavior of ϵ' . At $T > T_C$ and $T < T_C$ the spin density wave dynamics is governed by the free-carrier activation energy $\Delta_{fc} \approx 270 \text{ K}$ and by low energy barriers $\Delta \approx 60 \text{ K}$, respectively.

Finally, it is worth mentioning that we observed qualitatively the same low-temperature behavior of the non-ohmic conductivity [75] and the dielectric response [76] in $\text{Cu}(\text{DCNQI})_2$ material. This is of no surprise if one notes that this commensurate charge density wave material shows domain structure due to the coexistence of the metallic and insulating (CDW ordered) islands. Therefore, both systems share the commensurate density wave ground state, the domain structure becoming regular at low temperatures and the same – a pair of charged domain walls – relaxation entity.

6.2 General remarks considering the superconducting state

We start the discussion by pointing out that the well-defined, ground-state properties – complex susceptibility, penetration depth, and superfluid density – were essentially reproducible for all studied κ -(ET)₂Br single crystals from both syntheses S1 and S2. Cooling-rate-dependent effects were also reproducible, but the observed behavior was the same only for single crystals from the same synthesis, while it differed significantly from the observed behavior for single crystals from the other synthesis.

First, we would like to comment on the anisotropy in T_C . The onset of superconductivity is observed to be at 12.0 K and 11.2 K for the $H_{ac} \perp$ plane and the $H_{ac} \parallel$ plane geometries, respectively. The observed difference in T_C is somewhat surprising, since no other experimental group has reported it so far. In order to eliminate spurious influences, we have verified, by performing test experiments on the piece of a niobium foil used for calibration, that no thermal gradient larger than 0.05 K exists along the sample holder. Therefore, the observed difference in T_C is not an experimental artifact. We suggest that this anisotropy might be the consequence of the fact that the diamagnetic shielding is no longer effective for the $H_{ac} \parallel$ plane geometry in the region of 0.5 K below T_C , which is due to the small sample dimensions and the huge out-of-plane (Josephson-like) penetration depth near T_C . However, we point out that the T_C anisotropy has negligible, if any, effects on our data analysis, which is primarily done in the low-temperature region and therefore does not influence the resulting conclusions regarding the low-temperature behaviour of the physical quantities.

Second, we address the observed differences in cooling rate effects between samples S1 and S2. As pointed out earlier, both samples show the same behavior in the ground state: almost full diamagnetism for the $H_{ac} \perp$ plane geometry and the same temperature dependence and zero-temperature value of the in-plane and the out-of-plane penetration depths, as well as the same superfluid density temperature dependence. However, we note that the sample S2 required a completely different cooling procedure with significantly longer time spent in the temperature region around 80 K, compared to the sample S1, in order to reach the ground state. Moreover, the sample S2 is much less sensitive to the cooling rate. That is, the difference regarding low-temperature susceptibility and zero-temperature penetration depth values between A and Q states for the sample S2 is much smaller than the difference between R and Q states for the sample S1. Both features indicate that (i) the low-temperature state is critically determined by the time scale

of experiment in the region of glass transition and (ii) relaxation times of ethylene groups in the single crystals originating from the synthesis S2 are much longer than the ones in the single crystals originating from the synthesis S1. When the applied time scale is much longer than the relaxation time of the ethylene moieties, the low-temperature state is the ground state. In contrast, if the relaxation time exceeds the time scale of experiment, the remnant disorder at low temperatures will be substantial and the Q state will be established.

Different relaxation times of ethylene groups might also explain why the resistivity ratio $RR(T_G/T_C)$ is much larger for samples from the synthesis S1 when the standard slow cooling rate is applied. At this stage, we can only speculate about the possible origin of different relaxation times. The experimental observations that the crystals from the synthesis S2 show weak metallic behavior, instead of a semiconducting behavior between RT and 100 K observed for samples of the synthesis S1, might be of the same origin. In order to reveal the origin of the differences, several additional measurements were performed on samples of the syntheses S1 and S2. ESR measurements [77] and X-ray measurements [78] did not show any differences within the sensitivity of the experimental setup. Further, it has been suggested that the difference in resistivity behavior could be also due to the contamination with the chlorine atoms which replace bromine atoms [79]. Since the ordering of ethylene fragment is closely linked to the halogen atom, the contamination may introduce some degree of ordering already at RT. Indeed, the performed mass spectroscopy [80] showed a slight difference in the fragmentation of the BEDT-TTF molecules, in particular regarding the breaking off of the ethylene groups. However, since the used experimental setup is not sensitive to low masses below 100 daltons, we were unable to check the level of the contamination.

Finally, it should be noted that we have also studied several κ -(ET)₂NCS samples, which the sample S3 represents. Because of the experimental limitations we were unable to obtain the ground state and moreover because of the sample tendency to disintegrate only one geometry was successfully measured. However, on the basis of the obtained results we can conclude that for this material the low-temperature state is critically determined by the time scale of experiment in the region of glass transition as well. Further, relaxation times of ethylene groups in the sample S3 are comparable to or even larger than the ones for the sample S2. This can be concluded if one takes into consideration that the obtained value for cooling rate sensitivity for the sample S3 is the smallest among all three samples.

6.3 Superfluid density

Next we comment on the behavior of the in-plane superfluid density in the ground state. Our starting point is the d -wave symmetry of the conductivity, proposed by most of the experiments, i.e., $g(\mathbf{k}) = \cos(2\varphi)$ or $g(\mathbf{k}) = \sin(2\varphi)$, where φ is the angle between the quasiparticle momentum \mathbf{k} and the a -axis. These two functions represent $d_{x^2-y^2}$ -wave and d_{xy} -wave symmetry for the cylinder-like (in z -direction symmetrical) Fermi surfaces, respectively. In order to obtain the theoretical expression of ρ_s , first we have to calculate the ratio of the superconducting transition temperature and the zero-temperature superconducting order parameter from Eq. (2.30). This equation can be written in the following compact form

$$\Delta(0) = \pi e^{-\gamma} k_B T_C \exp[-\langle g^2(\mathbf{k}) \ln g(\mathbf{k}) \rangle / \langle g^2(\mathbf{k}) \rangle], \quad (6.1)$$

if one designates the integrals over φ and ϑ , which have the meaning of the averaging over the Fermi surface, with $\langle \rangle$. Noting that $\langle g^2(\mathbf{k}) \ln g(\mathbf{k}) \rangle = \frac{1}{2} \ln \frac{1}{2} + \frac{1}{4}$ and $\langle g^2(\mathbf{k}) \rangle = \frac{1}{2}$, we obtain

$$\Delta(0) = \pi e^{-\gamma} k_B T_C \exp[\ln 2 - \frac{1}{2}] = 2.14 k_B T_C. \quad (6.2)$$

Now we can proceed with the calculation of the superfluid density using Eq. (2.39). If the substitution $\Delta x = \sqrt{\xi^2 + \Delta^2 g^2(\mathbf{k})}$ is used, we can transform the expression into the following compact form

$$\begin{aligned} \rho_{s,\text{in}}(t) &= 1 - \frac{\Delta}{2kT} \int_0^\infty \left\langle \frac{x}{\sqrt{x^2 - g^2(\mathbf{k})}} \right\rangle \frac{1}{\cosh^2(\Delta x / 2kT)} dx \\ &\approx 1 - 2(\ln 2) \frac{kT}{\Delta} - \frac{9}{4} \zeta(3) \left(\frac{kT}{\Delta} \right)^3 \\ &\approx 1 - 0.6478t - 0.276t^3. \end{aligned} \quad (6.3)$$

Here we used $\langle x / \sqrt{x^2 - g^2(\mathbf{k})} \rangle = \frac{2}{\pi} x K(x)$ for $x \leq 1$, where $K(x)$ is the complete elliptic integral [81]. In the last step we used Eq. (6.2).

The coefficient a of the leading term t in $\rho_{s,\text{in}} = 1 - at + \dots$ depends strongly on the ratio of the superconducting transition temperature and the zero-temperature superconducting order parameter. The comparison of values for a in Eq. (6.3) to those in Eqs. (5.8) and (5.10) or Eqs. (5.12) and (5.13) suggests that the superconducting order parameter Δ at $T = 0$ K is much smaller than the one predicted by the weak-coupling limit. As a result, this would also imply that the nodal region, the volume of which

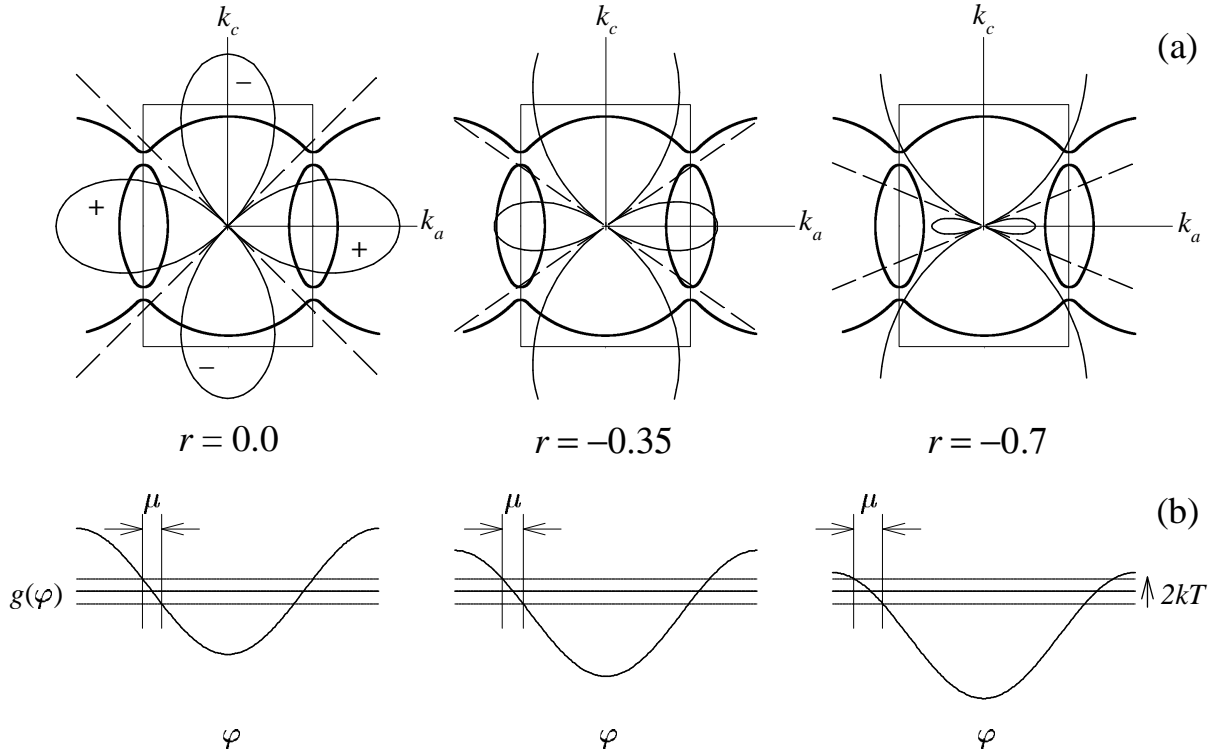


Fig. 6.1: The effects of the admixing of the s -wave component to the $d_{x^2-y^2}$ -wave, where r represents the s -wave component parameter. (a) The change of the node directions: Thick lines represent the Fermi surface, lines with a medium thickness superconducting gap and thin lines the Brillouin zone and crystallographic axes. Dashed lines represent node directions in the superconducting gap. (b) The change of the volume of the nodal region μ : The thick horizontal line represent the Fermi energy and thin horizontal lines the limits of the thermal excitations.

is inversely proportional to the angular slope of the gap near the node $\mu = dg(\varphi)/d\varphi|_{\text{node}}$ (Fig. 6.1(b)), occupies a much larger fraction of the phase space at low temperatures. We point out that the same behavior of ρ_{in} for $\lambda_{\text{in}}(0) \leq 1.3 \mu\text{m}$ was reported by Carrington *et al.* [39] They pointed out that only at $\lambda_{\text{in}}(0) \geq 1.8 \mu\text{m}$ does the slope become similar to the one reported for high-temperature superconducting cuprates and expected in the weak-coupling model. From our present data, we get $\lambda_{\text{in}}(0) \approx 3 \mu\text{m}$ for the crossover in-plane penetration depth value (see Fig. 5.14).

Obviously, since our results require a smaller superconducting order parameter Δ , the strong coupling model is of no help. On the other hand, a plausible interpretation of our results is to consider the mixture of the

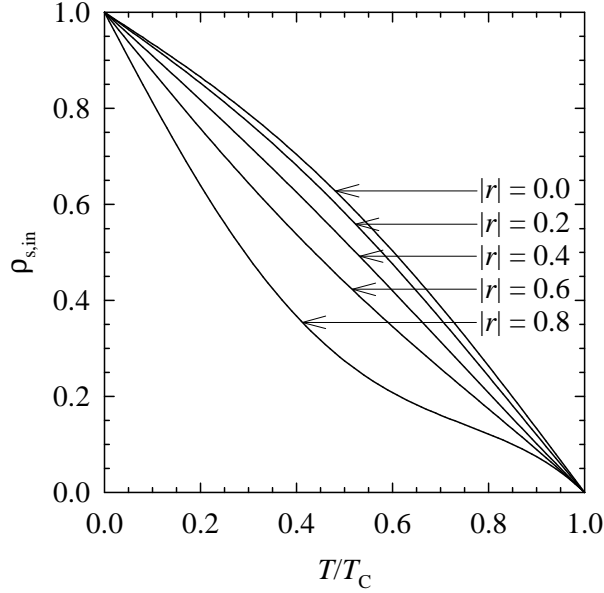


Fig. 6.2: Superfluid density in the $(d+s)$ -wave model for a few values of the s -wave component parameter r .

d -wave and s -wave order parameters, which corresponds to the superconducting order parameter $g(\mathbf{k}) = \cos(2\varphi) + r$, with r representing the s -wave component (Fig. 6.1) [82]. Using Eq. (6.1) and noting that $\langle g^2(\mathbf{k}) \ln g(\mathbf{k}) \rangle = (\frac{1}{2} + r^2) \ln \frac{1}{2} + \frac{1}{4} + \frac{3}{4}r^2$ and $\langle g^2(\mathbf{k}) \rangle = \frac{1}{2} + r^2$, we obtain

$$\Delta(0) = 2\pi e^{-\gamma} k_B T_C \exp\left[\ln 2 - \frac{1}{2} - \frac{2r^2}{1 + 2r^2}\right]. \quad (6.4)$$

If in the last step of Eq. (6.3) we use Eq. (6.4) instead of Eq. (6.2), leading linear coefficient a increases with the increase of r according to the expression

$$a = \frac{2 \ln 2}{2.14\sqrt{1 - r^2}} \exp\left[\frac{2r^2}{1 + 2r^2}\right]. \quad (6.5)$$

Additional factor $\sqrt{1 - r^2}$ is the result of the fact that, in case of $(d+s)$ -wave order parameter, $\rho_{s,in}$ becomes anisotropic and should be averaged over the conductivity plane.

The shapes of the superfluid density curves for several values of parameter r are given in Fig. 6.2. For our results, $|r| \approx 0.7$ gives a very good agreement, which is, on the other hand, theoretically very unlikely, as it will be shown in the next paragraph.

Recently, an admixture of the s -wave component with $r = -0.067$ for κ -(ET)₂NCS was suggested [82] based on the angular-dependent magnetothermal conductivity data [49]. These data suggest that the $d_{x^2-y^2}$ -wave

(depicted in Figs. 2.1 and 6.1) instead of the d_{xy} -wave pairing is responsible for the superconductivity in κ -(ET) $_2X$ materials. As argued in Sec. 1.4, this symmetry implies that both Fermi surfaces participate in pairing, which is in contradiction to the previous assumption that spin fluctuations are responsible for the superconducting mechanism [47]. Therefore, the origin of the electron pairing should be found elsewhere. The Coulomb interaction, which is responsible for the d -wave superconductivity, gives rise to both spin and charge fluctuations, so the obvious solution appears to be that charge fluctuations play the principal role in the κ -(ET) $_2X$ superconductivity. The value $r = -0.07$ suggests that the node lines in $g(\mathbf{k})$ pass through the gap between two Fermi surfaces. This is consistent with the $(d + s)$ -wave model in which the superconductivity is due to the charge fluctuations between different groups of dimers. On the other hand, for $r \approx -0.7$, the nodal directions cross the oval-shaped quasi-two-dimensional cylinders (Fig. 6.1(a)), and for $r \approx 0.7$, the nodal directions cross a pair of open quasi-one-dimensional sheets. If the $d+s$ superconductivity model is generated by the charge fluctuations, such a scenario is unlikely to work, since this implies a strong intra-Coulomb repulsion in each energy band. Indeed, the reported Coulomb repulsion exceeds the value of 1 eV [2]. Therefore, the exact mechanism of the pairing remains unclear and further theoretical as well as experimental work should be done to resolve this question.

On the other hand, to calculate the out-of-plane superfluid density coherent Josephson tunneling between superconducting layers is assumed, as proposed by K. Maki [83]. The calculation is performed within the Ambegaokar-Baratoff model [84], properly generalized for the d -wave superconductor. It was assumed that only the direction, but not the magnitude of the in-plane electron momentum is conserved. Finally, this gives

$$\begin{aligned} \rho_{s,\text{out}}(t) &= \frac{\pi}{2} \frac{\Delta}{\Delta(0)} \left\langle g(\mathbf{k}) \tanh \left(\frac{\Delta g(\mathbf{k})}{2kT} \right) \right\rangle \\ &\approx \left\{ 1 - \frac{\pi^2}{6} \left(\frac{kT}{\Delta} \right)^2 - \frac{7\pi^4}{120} \left(\frac{kT}{\Delta} \right)^4 \right\} \left\{ 1 - \frac{3}{2} \zeta(3) \left(\frac{kT}{\Delta} \right)^3 \right\} \quad (6.6) \\ &\approx 1 - 0.3592t^2. \end{aligned}$$

Here $1 - 3\zeta(3)(kT/\Delta)^3$ comes from $\Delta/\Delta(0)$. It should be also pointed out that the related Josephson plasmons have been reported in the κ -(ET) $_2$ NCS material [85]. Comparing theoretical expression Eq. (6.6) to the experimental ones, Eqs. (5.9) and (5.11) show qualitatively the same behavior with a small discrepancy in the value of the first coefficient of the expansion.

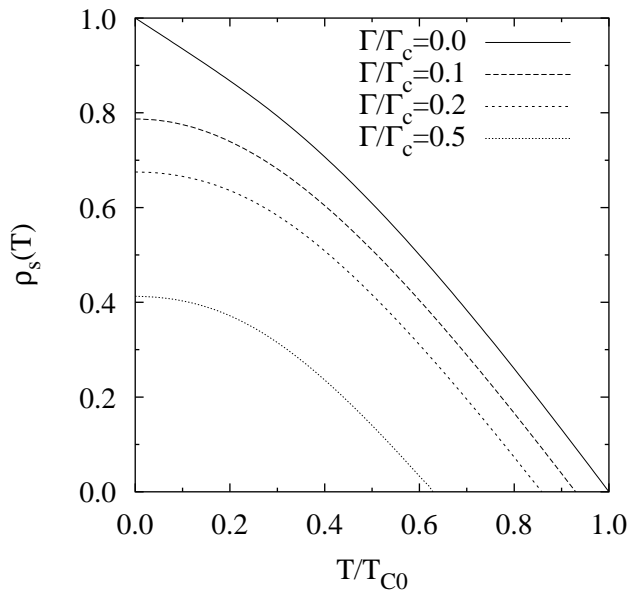


Fig. 6.3: The superfluid density as a function of T/T_{C0} for the state with no scattering, and three states with a different degree of the scattering. T_{C0} is the temperature of phase transition for the state with no scattering. Note that all depicted superfluid densities share the same $\lambda(0)$, obtained from the state with no scattering. [87]

6.4 Remnant disorder in the superconducting state

Now, we address the behavior of the in-plane superfluid density in states with different cooling rates. In this discussion we will concentrate on the changes observed for the sample S2, but the same conclusions could be obtained in the case of the sample S1. A quick inspection of Tables 5.1 and 5.2 shows two distinct effects of the increased cooling rate: a large increase of the penetration depth and a rather small suppression of the phase transition temperature. The similar conclusions were obtained also by magnetization studies by Aburto *et al.* [86]. Furthermore, considering the polynomial fit in the intermediate state in Eq. (5.14), we see that the in-plane superfluid density low-temperature variation changes to the squared temperature dependence.

First of all, we ascribe the difference between the A state (ground state), the R state (intermediate state), and the Q state to the residual degree of the ethylene disorder. The A state we discussed is the ground state with the least disorder in the ethylene groups. Indeed, this idea is consistent with the

theoretical predictions. Hirschfeld *et al.* [88] pointed out that an infinitesimal amount of disorder in unconventional superconducting states with nodes has two effects near $T = 0$ K: First, a non-zero density of states at zero energy exists, leading to the existence of the “gapless” temperature regime. Second, the penetration depth increases compared to the no scattering case, and its variation, as well as the superfluid density variation, change to the squared temperature dependence. Furthermore, Sun *et al.* [89, 90] studied thermodynamic quantities and superfluid density for the d -wave model with the impurity scattering in the unitary limit in the whole temperature range (Fig. 6.3). However, there is a serious discrepancy between our experimental data and the impurity model, which established that a small disorder also depresses T_C dramatically. That is, in our experiment, it seems that T_C is practically unaffected by the ethylene disorder for the intermediate state, achieved by the slow cooling of -0.2 K/min in the region of the glass transition. Further, taking into account the fact that the $\lambda(0)$ increases for at least by a factor of 6, the superconducting electron density at 0 K, $n_s(0) \propto \lambda^{-2}(0)$, decreases at least by a factor of 36. Such a simple impurity model cannot describe the surprising combination of these two features. On the other hand, the results for other low-temperature states achieved by cooling rates $q_C < -1$ K/min for the sample S1 and for the Q state in the sample S2 are more consistent with the theory. In these cases both T_C , $\chi'(0)$, and therefore $\lambda(0)$ are simultaneously influenced by the remnant ethylene disorder (see Tables 5.1 and 5.2). However, it is still difficult to correlate the observed behavior to the impurity model quantitatively. This discrepancy might indicate that the degree of disorder at low temperatures, as defined by the cooling rate in the region of the glass transition, has also a profound influence on electronic correlations, responsible for the SC pairing.

Further we address other explanations for the observed effects of the remnant disorder in the superconducting state. For example, the authors of Ref. 91 concluded that the suppression of the diamagnetism in the deuterated material is due to the mixing of a superconducting and an antiferromagnetic phases. However, this possibility does not imply any suppression of the phase transition temperature, in contrast to the observed small suppression in our results [86]. The authors of Ref. 86 studied the situation that combines two theoretical situations mentioned above – the possibility that for the scattering in the unitary limit the defects may form clusters of the antiferromagnetic phase. If this is so, one should consider the existence of a non-superconducting fraction and the actual $\lambda(0)$ variations would be smaller than the ones computed from the magnetization data, leaving the T_C variations untouched. However, the performed calculations did not agree well with the experimental results. Another appealing possibility comes from

the effect of the weak localization [86]. Unlike in the impurity scattering in the unitary limit discussed above, where the product $\Delta(0)\tau$ (where τ is the scattering time) determines both T_C and $\lambda(0)$ variations, in case of the weak localization variation of T_C is determined by $\varepsilon_F\tau$ (where ε_F is Fermi energy). This enables the possibility of variations of T_C and $\lambda(0)$ being different. The quantitative considerations, however, did not give a good correspondence to the experimental results.

At this point we would like to recall the result of Kund *et al.* [26], which showed changes in the crystal structure parameters for κ -(ET)₂Br in the region of the glass transition. In particular, while the first in-plane lattice parameter a value displays a peak, the second in-plane lattice parameter c , as well as out-of-plane lattice parameter b values display kinks at the same temperature. It might be that these changes are also susceptible to the cooling rate. In addition, the authors of Ref. 4 have pointed out that the role of disorder in this class of superconductors might be different than in the other unconventional superconductors due to the vicinity of the insulating state in the phase diagram. This is due to the fact that in the former the electrons are strongly correlated, which suggests the vicinity of the Mott transition. The authors argue that the effect of disorder in the metallic state near the antiferromagnetic Mott insulator is qualitatively different from the situation of the simple Anderson localization.

Coming back to the intermediate state, the most intriguing fact about Fig. 5.15 is that in the intermediate state the observed data could be well described by the s -wave model as well. This gives a possible explanation for the contradictory findings in favor of the s -wave and d -wave models in the same material. The behavior is obviously strongly influenced by both thermal history and synthesis, which suggests that the same material was not measured in the same low-temperature state.

6.5 Coexistence of two phases

Now we shall study in more detail the appealing possibility of coexistence of AF and SC phases already mentioned in the previous section. Regarding indication of the decrease in the superconducting electron density, which was pointed out in the previous section, we suggest that it may be related to the reduction of the superconducting volume. It has been already reported that cooling rates combined with progressive deuteration influence the low-temperature electronic state in κ -(ET)₂Br samples [4, 91]. The deuterated κ -(ET)₂Br system is situated in the critical region between an insulating AF transition at 15 K and a SC transition at 11.5 K. Despite the slow cool-

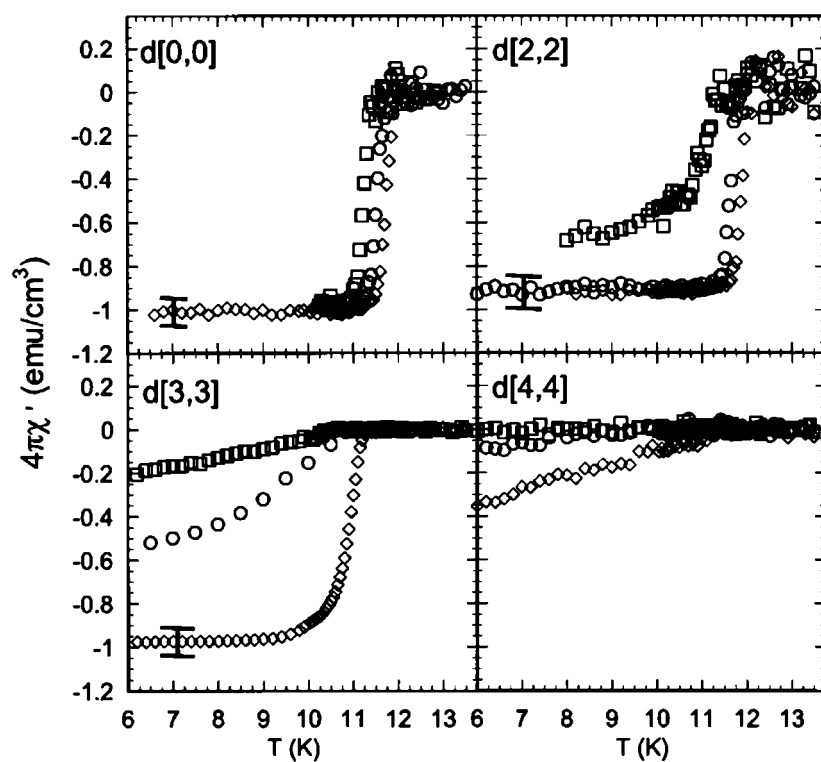


Fig. 6.4: ac susceptibility of $d(0,0)$ -, $d(2,2)$ -, $d(3,3)$ -, and $d(4,4)$ - x -(ET)₂Br in the various cooling conditions: a rapid cooling of 10 K/min (\square), a slow cooling of 0.5 K/min (\circ), and an annealing at 70 K for 12h (\diamond). n, n' in $d(n, n')$ represent number of the deuterium in each ethylene group. [4]

ing rate, the deuterated sample gives almost the same T_C as in the hydrogenated κ -(ET)₂Br system, the SC state being not fully established in the bulk (Fig. 6.4). Note that this result strongly resembles to what we observed for the S2 samples in the intermediate (*R*) state. In addition, a gradual decrease of the susceptibility below T_C in the deuterated system strongly indicates the inhomogeneous nature of the SC state. This is in contrast to what we observe in the sample S2, in which the susceptibility curves are rather sharp even in the *Q* state. More rapid cooling rates induce a decrease of T_C and a substantial decrease of the SC volume fraction. The authors of Refs. 4 and 91 have argued that since the electronic specific heat of rapidly cooled deuterated samples did not show any finite electronic contribution at low temperatures, the missing part of the superconducting phase should be considered to be the magnetic insulating phase. The question arises if their conclusion might also be valid in the hydrogenated system. Taking into account the structure of the phase diagram of this class of superconductors (Fig. 1.2), we think that this might be the case. However, the specific heat data under carefully controlled cooling cycles are needed to resolve this issue.

The intimate relation between antiferromagnetic and superconducting states is also supported by anomalous behavior in the susceptibility (see Sec. 5.2.1). This suggests that the SC and AF domains compete in the ground state and that in certain conditions an AF domain could turn into a SC one or vice-versa. It is interesting to see whether this domain effects could be somehow connected to the charged domain walls in the insulating spin density wave ground state. Indeed, some recent articles suggest that the superconducting ground state in the cuprates consists of antiferromagnetic regions called *stripes*, bordered by the charge domain walls. These structures are easily detected in the AF ground state of the cuprates, where they are pinned to the background lattice [92]. Nevertheless, authors of Ref. 92 argue that they might exist even in the SC state, where they are hard to observe because of their dynamic behavior. Indeed, while the elastic neutron scattering shows no stripe structure, the inelastic neutron scattering in the Meissner superconducting state ($H < H_{C1}$) show incommensurate magnetic peaks possibly related to dynamic stripe structure. However, the consensus about the stripe existence in the SC state still does not exist and the answer to the question whether the presence of the stripes induces or destroys the SC state remains open. It should also be noted that our estimate of the charged domain wall size at 22 K in the κ -(ET)₂Cl insulating spin density wave state, amounting to about $L_{\text{wall}} \approx 0.1 - 1 \mu\text{m}$, is much larger than the typical size of the charged domain walls of order of 10 Å in the cuprates. It is plausible that the charge domain walls become thinner and eventually comparable to the ones in the cuprates by the reduction of the temperature. On the other

hand, since we expect rather huge antiferromagnetic domains in κ -(ET)₂Cl, the question how can we relate them to thin antiferromagnetic stripes of order of 10 Å in the cuprates remains open. Therefore, further work is necessary to investigate the possibility of domain size shrinking and domain walls number increase by the applied pressure to the κ -(ET)₂Cl material.

7 Summary

The family of quasi-two-dimensional κ -(ET)₂X organic materials distinguishes itself by the rich phase diagram, very similar to the one found in the high-temperature superconducting cuprates. Because of this similarity, an enormous effort was made in order to understand the superconducting state in these materials. Despite of that, a long time controversy regarding the symmetry of the superconducting state has persisted to this day.

In order to make a breakthrough in the understanding of the problem, we concentrated our attention on three important issues. First, if one wants to understand the superconducting ground state, one has to correlate its properties with the properties of the neighboring insulating spin density wave ground state and the normal state. Second, sample-dependent and thermal history effects should be accounted for. And finally, the full characterization of the superconducting state should be made on one single crystal and, if possible, using one experimental method. Indeed, in our investigation we successfully addressed all of these issues.

Normal state properties point to strong electron correlations, which, depending on the subtle crystal properties, lead to either an antiferromagnetic or a superconducting state. The situation is further complicated by the existence of the important relaxation effects, due to the glass transition, that influence the properties of the superconducting ground state. Our measurements of the insulating spin density wave ground state included the measurement of the single-particle resistivity, the non-ohmic conductivity and the dielectric spectroscopy. The obtained non-ohmic and dielectric response can be explained only by the existence of the collective mode. The behavior of physical parameters, related to the response, suggests that the short-wavelength – charge domain wall pairs – excitations are the entities responsible for the observed properties. The existence of domain walls is naturally connected to the existence of the reported weak ferromagnetic ordering, which also implies the existence of domains.

Next, the full characterization of the superconducting state was made for samples of different syntheses. Further, every sample was cooled using

several different well-controlled conditions in the temperature region that corresponds to the glass transition. Large differences in the properties of the superconducting state were observed and the ground state was assigned to the low-temperature state obtained by the slowest cooling rate.

The investigation of the superconducting state was performed by the extraction of the penetration depth. This method has a large advantage as regarding to the fact that the superfluid density can be calculated directly from the penetration depth. The measurements were performed using the ac susceptometer of high precision, which was inevitable in order to account for small dimensions of the studied samples. The measurements were done in magnetic fields, more than an order of magnitude smaller than the Earth's field, which is far below the lower critical magnetic field, so the genuine Meissner state was measured and the possible vortex effects were avoided. Finally, a specially developed improved calibration was designed in order to obtain the reliable absolute value of the penetration depth for two distinct geometries, with the direction of the magnetic field parallel and perpendicular to the isotropic crystal planes.

The qualitative temperature dependence of both the in-plane and the out-of-plane superfluid densities in the genuine superconducting ground state undoubtedly revealed that the symmetry of the superconductivity requires the existence of the linear nodes in the superconducting gap, which is in a good agreement with the d -wave model. Also, to obtain the temperature dependence of the out-of-plane suprafluid density, Josephson coupling between the conducting planes has to be taken into account. The nodes in the superconducting gap are not surprising if one takes into consideration that an antiferromagnetic state is located in the vicinity of the superconducting one, which points to the unconventional superconductivity. In order to also get a quantitative agreement, the $(d + s)$ -wave model was used, however, a rather large s -wave component needed to fit our data was not consistent with the recent thermal conductivity results. On the other hand, the superconducting state, obtained by the faster cooling rate, can be well described by the model of the d -wave superconductor with impurities. Even more important, this state can be correlated fairly well to the s -wave coupling superconducting model, with no nodes in the superconducting gap. This fact suggests a possible way out of the contradicting results in the scientific community.

Finally, few domain effects in the superconducting state, combined with the domain structure in the neighboring insulating spin density wave ground state, point to an important possibility of the existence of a novel ground state. Since κ -(ET)₂X materials are in many ways very similar to high-temperature superconducting cuprates, a question appears if this state can be somehow related to newly reported structures – stripes – in the latter materials.

Bibliography

- [1] D. Jérôme, A. Mazaud, M. Ribault, and K. Bechgaard, *J. Phys. Lett. Paris* **41**, L95 (1980).
- [2] K. Kanoda, *Hyperfine Interact.* **104**(1–4), 235 (1997).
- [3] S. Lefebvre, P. Wzietek, S. Brown, C. Bourbonnais, D. Jérôme, C. Mézière, M. Fourmigué, and P. Batail, *Phys. Rev. Lett.* **85**(25), 5420 (2000).
- [4] H. Taniguchi, A. Kawamoto, and K. Kanoda, *Phys. Rev. B* **59**(13), 8424 (1999).
- [5] L. I. Buravov, N. D. Kushch, V. A. Merzhanov, M. V. Osherov, A. G. Khomenko, and E. B. Yagubskii, *J. Phys. I France* **2**, 1257 (1992).
- [6] M. Pinterić, M. Miljak, N. Biškup, O. Milat, I. Aviani, S. Tomić, D. Schweitzer, W. Strunz, and I. Heinen, *Eur. Phys. J. B* **11**(2), 217 (1999).
- [7] K. Oshima, H. Urayama, H. Yamochi, and G. Saito, *Physica C* **153–155**, 1148 (1988).
- [8] J. M. Williams, A. M. Kini, H. H. Wang, K. D. Carlson, U. Geiser, L. K. Montgomery, G. J. Pyrka, D. M. Watkins, J. M. Kommers, S. J. Boryschuk, A. V. Strieby Crouch, W. K. Kwok, *et al.*, *Inorg. Chem.* **29**, 3272 (1990).
- [9] B. Thoma, *Temperaturabhängige Leitfähigkeits-, Thermokraft- und Magnetowiderstandsuntersuchungen an organischen Leitern*, B.S. thesis, University of Stuttgart (1996).
- [10] L. K. Montgomery, R. M. Vestal, K. P. Starkey, B. W. Fravel, M. J. Samide, D. G. Peters, C. H. Mielke, and J. D. Thompson, *Synth. Met.* **103**, 1878 (1999).

-
- [11] C. H. Mielke, N. Harrison, D. G. Rickel, A. H. Lacerda, R. M. Vestal, and L. K. Montgomery, Phys. Rev. B **56**(8), R4309 (1997).
- [12] U. Geiser, A. J. Schultz, H. H. Wang, D. M. Watkins, D. L. Stupka, J. M. Williams, J. E. Schirber, D. L. Overmyer, D. Jung, J. J. Novoa, and M.-H. Whangbo, Physica C **174**, 475 (1991).
- [13] Y.-N. Xu, W. Y. Ching, Y. C. Jean, and Y. Lou, Phys. Rev. B **52**(17), 12946 (1995).
- [14] J. Singleton, Rep. Prog. Phys. **63**, 1111 (2000).
- [15] H. Weiss, M. V. Kartsovnik, W. Biberacher, E. Steep, E. Balthes, A. G. M. Jansen, K. Andres, and N. D. Kushch, Phys. Rev. B **59**(19), 12370 (1999).
- [16] Y. Nogami, J. P. Pouget, H. Ito, T. Ishiguro, and G. Saito, Solid State Commun. **89**(2), 113 (1994).
- [17] P. Wzietek, H. Mayaffre, D. Jérôme, and S. Brazovskii, J. Phys. I France **6**(12), 2011 (1996).
- [18] T. Arai, K. Ichimura, K. Nomura, S. Takasaki, J. Yamada, S. Nakatsuji, and H. Anzai, Synth. Met. **120**, 707 (2001).
- [19] M. Kubota, G. Saito, H. Ito, T. Ishiguro, and N. Kojima, Mol. Cryst. Liq. Cryst. **284**, 367 (1996).
- [20] M. Pinterić, *Niskofrekventna dielektrična spektroskopija i nelinearni električni transport vala gustoće spina*, Master's thesis, University of Zagreb (2000).
- [21] H. Akutsu, K. Saito, and M. Sorai, Phys. Rev. B **61**(6), 4346 (2000).
- [22] J. Müller, M. Lang, F. Steglich, J. A. Schlueter, A. M. Kini, and T. Sasaki, Phys. Rev. B **65**, 144521 (2002).
- [23] M. A. Tanatar, T. Ishiguro, T. Kondo, and G. Saito, Phys. Rev. B **59**(5), 3841 (1999).
- [24] K. Kanoda, unpublished.
- [25] X. Su, F. Zuo, J. A. Schlueter, M. E. Kelly, and J. M. Williams, Phys. Rev. B **57**(22), R14056 (1998).

-
- [26] M. Kund, H. Müller, W. Biberacher, K. Andres, and G. Saito, *Physica B* **191**, 274 (1993).
- [27] Y. Watanabe, H. Sato, T. Sasaki, and N. Toyota, *J. Phys. Soc. Jpn.* **60**(11), 3608-3611 (1991).
- [28] H. Taniguchi and K. Kanoda, *Synth. Met.* **103**, 1967 (1999).
- [29] U. Welp, S. Fleshler, W. K. Kwok, G. W. Crabtree, K. D. Carlson, H. H. Wang, U. Geiser, J. M. Williams, and V. M. Hitsman, *Phys. Rev. Lett.* **69**(5), 840 (1992).
- [30] K. Miyagawa, A. Kawamoto, Y. Nakazawa, and K. Kanoda, *Phys. Rev. Lett.* **75**, 1174 (1995).
- [31] T. Takahashi, Y. Maniwa, H. Kawamura, and G. Saito, *J. Phys. Soc. Jpn.* **55**, 1364 (1986).
- [32] H. Kino and H. Fukuyama, *J. Phys. Soc. Jpn.* **64**(8), 2726 (1995).
- [33] I. Dzyaloshinsky, *J. Phys. Chem. Solids* **4**, 241 (1958); T. Moriya, *Phys. Rev.* **120**(1), 91 (1960).
- [34] J. Hagel, S. Wanka, D. Beckmann, J. Wosnitza, D. Schweitzer, W. Strunz, and M. Thumfart, *Physica C* **291**, 213 (1997).
- [35] M. Lang, *Supercond. Rev.* **2**, 1 (1996).
- [36] M. Dressel, O. Klein, G. Grüner, K. D. Carlson, H. H. Wang, and J. M. Williams, *Phys. Rev. B* **50**(18), 13603 (1994).
- [37] S. L. Lee, F. L. Pratt, S. J. Blundell, C. M. Aegerter, P. A. Pattenden, K. H. Chow, E. M. Forgan, T. Sasaki, W. Hayes, and H. Keller, *Phys. Rev. Lett.* **79**(8), 1563 (1997).
- [38] D. Achkir, M. Poirier, C. Bourbonnais, G. Quirion, C. Lenoir, P. Batail, and D. Jérôme, *Phys. Rev. B* **47**(17), 11595 (1993).
- [39] A. Carrington, I. J. Bonalde, R. Prozorov, R. W. Giannetta, A. M. Kini, J. Schlueter, H. H. Wang, U. Geiser, and J. M. Williams, *Phys. Rev. Lett.* **83**(20), 4172 (1999).
- [40] P. A. Mansky, P. M. Chaikin, and R. C. Haddon, *Phys. Rev. B* **50**(21), 15929 (1994).

-
- [41] N. H. Tea, F. A. B. Chaves, U. Klostermann, R. Giannetta, M. B. Salamon, J. M. Williams, H. H. Wang, and U. Geiser, *Physica C* **280**, 281 (1997).
- [42] H. Mayaffre, P. Wzietek, D. Jérôme, C. Lenoir, and P. Batail, *Phys. Rev. Lett.* **75**(22), 4122-4125 (1995).
- [43] Y. Nakazawa and K. Kanoda, *Phys. Rev. B* **55**, R8670 (1997).
- [44] S. Belin, K. Behnia, and A. Deluzet, *Phys. Rev. Lett.* **81**(21), 4728 (1998).
- [45] L. P. Le, G. M. Luke, B. J. Sternlieb, W. D. Wu, Y. J. Uemura, J. H. Brewer, T. M. Riseman, C. E. Stronach, G. Saito, H. Yamochi, H. H. Wang, A. M. Kini, *et al.*, *Phys. Rev. Lett.* **68**(12), 1923 (1992).
- [46] K. Kanoda, K. Akiba, K. Suzuki, T. Takahashi, and G. Saito, *Phys. Rev. Lett.* **65**(10), 1271 (1990).
- [47] R. Louati, S. Charfi-Kaddour, A. Ben Ali, R. Bennaceur, and M. Héritier, *Phys. Rev. B* **62**(9), 5957 (2000); R. Louati, S. Charfi-Kaddour, A. Ben Ali, R. Bennaceur, and M. Héritier, *Synth. Met.* **103**, 1857 (1999).
- [48] T. Arai, K. Ichimura, K. Nomura, S. Takasaki, J. Yamada, S. Nakatsuji, and H. Anzai, *Phys. Rev. B* **63**, 104518 (2001).
- [49] K. Izawa, H. Yamaguchi, T. Sasaki, and Y. Matsuda, *Phys. Rev. Lett.* **88**(2), 027002 (2002).
- [50] D. R. Harshman, R. N. Kleiman, R. C. Haddon, S. V. Chichester-Hicks, M. L. Kaplan, L. W. Rupp, Jr., T. Pfiz, D. L. Williams, and D. B. Mitzi, *Phys. Rev. Lett.* **64**(11), 1293 (1990).
- [51] M. Lang, N. Toyota, T. Sasaki, and H. Sato, *Phys. Rev. Lett.* **69**(9), 1443 (1992).
- [52] H. Elsinger, J. Wosnitza, S. Wanka, J. Hagel, D. Schweitzer, and W. Strunz, *Phys. Rev. Lett.* **84**(26), 6098 (2000).
- [53] J. Müller, M. Lang, R. Helfrich, F. Steglich, and T. Sasaki, *Phys. Rev. B* **65**, 140509 (2002).
- [54] J. Bardeen, L. N. Cooper, and J. R. Schrieffer, *Phys. Rev.* **108**(5), 1175 (1957).

- [55] M. Tinkham, *Introduction to Superconductivity* (McGraw-Hill, New York, 1996).
- [56] V. P. Mineev and K. V. Samokhin, *Introduction to Unconventional Superconductivity* (Gordon and Breach science publishers, Amsterdam, 1999).
- [57] K. Maki, in *Lectures on the Physics of Highly Correlated Electron Systems*, edited by F. Mancini (American Institute of Physics, 1998), pp. 83–128, ISBN 0-56396-789-8.
- [58] L. N. Cooper, Phys. Rev. **104**(4), 1189 (1956).
- [59] M. Sigrist and K. Ueda, Rev. Mod. Phys. **63**(2), 239 (1991).
- [60] Đ. Drobac, *Ac susceptibilnost nekih amorfnih feromagnetskih slitina u području faznog prijelaza*, Ph.D. thesis, University of Zagreb (1997).
- [61] <http://www.cryobind.com/>.
- [62] J. A. Osborn, Phys. Rev. **67**(11-12), 351 (1945).
- [63] G. W. Crabtree, Phys. Rev. B **16**(3), 1117 (1977).
- [64] M. Pinterić, S. Tomić, M. Prester, Đ. Drobac, O. Milat, K. Maki, D. Schweitzer, I. Heinen, and W. Strunz, Phys. Rev. B **61**(10), 7033 (2000).
- [65] M. Pinterić, S. Tomić, M. Prester, Đ. Drobac, and K. Maki, Phys. Rev. B **66**(17), 174521 (2002).
- [66] Đ. Drobac, J. Magn. Magn. Mater. **183**, 71 (1998).
- [67] M. Tinkham, *Introduction to Superconductivity* (McGraw-Hill, New York, 1996), p. 20.
- [68] K. Maki and A. Virosztek, Phys. Rev. B **42**(1), 655 (1990).
- [69] S. Tomić, J. Cooper, W. Kang, D. Jérôme, and K. Maki, J. Phys. I France **1**, 1603 (1991).
- [70] Y. T. Tseng, G. X. Tessema, and M. Skove, Phys. Rev. B **48**(7), 4871 (1993).
- [71] M. Tinkham, *Introduction to Superconductivity* (McGraw-Hill, New York, 1996), p. 25.

- [72] T. Vuletić, D. Herman, N. Biškup, M. Pinterić, A. Omerzu, S. Tomić, and M. Nagasawa, *J. Phys. IV* **9**(10), Pr10-275 (1999).
- [73] A. Bjeliš and K. Maki, *Phys. Rev. B* **44**(13), 6799 (1991).
- [74] M. Pinterić, N. Biškup, S. Tomić, D. Schweitzer, W. Strunz, and I. Heinen, in *35th International Conference on Microelectronics, Devices and Materials and Workshop on Microsystems, October 13. - 15. 1999, Ljubljana, Slovenia. Proceedings*, edited by S. Amon, L. Trontelj, and I. Šorli (MIDEM - Society for Microelectronics, Electronic Components and Materials, Ljubljana, 1999), pp. 83–88, ISBN 961-90001-7-X.
- [75] T. Vuletić, M. Pinterić, M. Lončarić, S. Tomić, and J. U. von Schütz, *Synth. Met.* **120**, 1001 (2001).
- [76] M. Pinterić, T. Vuletić, M. Lončarić, S. Tomić, and J. U. von Schütz, *Eur. Phys. J. B* **16**(3), 487 (2000).
- [77] S. Dolanski Babić, unpublished.
- [78] O. Milat, unpublished.
- [79] M. A. Tanatar, private communication.
- [80] D. Srzić and S. Dolanski Babić, unpublished.
- [81] H. Won and K. Maki, *Phys. Rev. B* **49**(2), 1397 (1994).
- [82] H. Won and K. Maki, *Physica B* **312-313**, 44 (2002).
- [83] S. Tomić, M. Pinterić, K. Maki, M. Prester, Đ. Drobac, O. Milat, D. Schweitzer, I. Heinen, and W. Strunz, *J. Phys. IV* **9**(10), Pr10-301 (1999).
- [84] V. Ambegaokar and A. Baratoff, *Phys. Rev. Lett.* **10**(11), 486 (1963); V. Ambegaokar and A. Baratoff, *Phys. Rev. Lett.* **11**(2), 104 (1963).
- [85] T. Shibauchi, M. Sato, A. Mashio, T. Tamegai, H. Mori, S. Tajima, and S. Tanaka, *Phys. Rev. B* **55**(18), R11977 (1997).
- [86] A. Aburto, L. Fruchter, and C. Pasquier, *Physica C* **303**, 185 (1998).
- [87] H. Won, unpublished.
- [88] P. J. Hirschfeld and N. Goldenfeld, *Phys. Rev. B* **48**(6), 4219 (1993).

- [89] Y. Sun and K. Maki, Phys. Rev. B **51**(9), 6059 (1995).
- [90] Y. Sun and K. Maki, Europhys. Lett. **32**(4), 355 (1995).
- [91] A. Kawamoto, K. Miyagawa, and K. Kanoda, Phys. Rev. B **55**(21), 14140 (1997).
- [92] J. M. Tranquada, B. J. Sternlieb, J. D. Axe, Y. Nakamura, and S. Uchida, Nature **375**, 561 (1995).

List of publications

- [1] Silvia Tomić, Neven Biškup, **Marko Pinterić**, J. U. von Schütz, Holger Schmitt, and Roger Moret. Low-frequency dielectric response of charge-density wave pinned by commensurability in $(2,5(\text{OCH}_3)_2\text{DCNQI})_2\text{Li}$. *Europhys. Lett.* **38**(3), 219–224 (1997).
- [2] **Marko Pinterić**, Silvia Tomić, and J. U. von Schütz. Transport properties of charge-density wave in the $(2,5(\text{OCH}_3)_2\text{DCNQI})_2\text{Li}$. In Marko Hrovat, Dejan Križaj, and Iztok Šorli, editors, *34th International Conference on Microelectronics, Devices and Materials with the Satellite Minisymposium on Semiconductor Radiation Detectors, September 23. - 25. 1998, Rogaska Slatina, Slovenia. Proceedings* pages 99–104 Ljubljana (1998). MIDEM - Society for Microelectronics, Electronic Components and Materials.
- [3] **Marko Pinterić**, Mladen Prester, Silvia Tomić, Kazumi Maki, Dieter Schweitzer, Ilsabe Heinen, and Werner Strunz. Superconducting state in the layered organic superconductor κ -(BEDT-TTF) $_2$ Cu[N(CN) $_2$]Br. *Synth. Met.* **103**, 1869–1872 (1999).
- [4] **Marko Pinterić**, Neven Biškup, Silvia Tomić, Dieter Schweitzer, Werner Strunz, and Ilsabe Heinen. Collective charge response in the weak ferromagnetic phase of κ -(BEDT-TTF) $_2$ Cu[N(CN) $_2$]Cl. *Synth. Met.* **103**, 1937 (1999).
- [5] **Marko Pinterić**, Neven Biškup, Silvia Tomić, and J. U. von Schütz. Non-ohmic electrical transport in the charge-density wave state of $(2,5(\text{OCH}_3)_2\text{DCNQI})_2\text{Li}$. *Synth. Met.* **103**, 2185–2186 (1999).
- [6] **Marko Pinterić**, Marko Miljak, Neven Biškup, Ognjen Milat, Ivica Aviani, Silvia Tomić, Dieter Schweitzer, Werner Strunz, and Ilsabe Heinen. Magnetic anisotropy and low-frequency dielectric response of weak ferromagnetic phase in κ -(BEDT-TTF) $_2$ Cu[N(CN) $_2$]Cl, where

- BEDT-TTF is bis(ethylenedithio)tetrathiafulvalene. *Eur. Phys. J. B* **11**(2), 217–225 (1999).
- [7] **Marko Pinterić**, Neven Biškup, Silvia Tomić, Dieter Schweitzer, Werner Strunz, and Ilsabe Heinen. The low-frequency dielectric response and non-linear DC electrical transport in κ -(BEDT-TTF)₂Cu[N(CN)₂]Cl. In Slavko Amon, Lojze Trontelj, and Iztok Šorli, editors, *35th International Conference on Microelectronics, Devices and Materials and Workshop on Microsystems, October 13. - 15. 1999, Ljubljana, Slovenia. Proceedings* pages 83–88 Ljubljana (1999). MIDEM - Society for Microelectronics, Electronic Components and Materials.
- [8] Tomislav Vuletić, Damir Herman, Neven Biškup, **Marko Pinterić**, Aleš Omerzu, Silvia Tomić, and Mitsuharu Nagasawa. Single-particle and spin-density wave charge dynamics in (TMTSF)₂PF₆ and (TMTSF)₂AsF₆: A comparative overview. *J. Phys. IV* **9**(10), Pr10–275–Pr10–277 (1999).
- [9] Silvia Tomić, **Marko Pinterić**, Kazumi Maki, Mladen Prester, Đuro Drobac, Ognjen Milat, Dieter Schweitzer, Ilsabe Heinen, and Werner Strunz. Out-of-plane superfluid density of a layered organic superconductor: The coherent Josephson tunneling. *J. Phys. IV* **9**(10), Pr10–301–Pr10–303 (1999).
- [10] **Marko Pinterić**, Silvia Tomić, Mladen Prester, Đuro Drobac, Ognjen Milat, Kazumi Maki, Dieter Schweitzer, Ilsabe Heinen, and Werner Strunz. Probing the order parameter of the layered organic superconductor κ -(BEDT-TTF)₂Cu[N(CN)₂]Br by AC susceptibility measurements. *Phys. Rev. B* **61**(10), 7033–7038 (2000).
- [11] Silvia Tomić, **Marko Pinterić**, Kazumi Maki, Mladen Prester, Đuro Drobac, Ognjen Milat, Dieter Schweitzer, Ilsabe Heinen, and Werner Strunz. In-plane and out-of-plane superfluid density of the layered organic superconductor κ -(BEDT-TTF)₂Cu[N(CN)₂]Br. *J. Phys. IV* **10**(3), Pr3–161–Pr3–166 (2000).
- [12] **Marko Pinterić**, Tomislav Vuletić, Martin Lončarić, Silvia Tomić, and J. U. von Schütz. Low frequency dielectric spectroscopy of the Peierls-Mott insulating state in the deuterated copper-DCNQI systems. *Eur. Phys. J. B* **16**(3), 487–493 (2000).
- [13] Silvia Tomić, **Marko Pinterić**, Tomislav Vuletić, J. U. von Schütz, and Dieter Schweitzer. Low-frequency dielectric spectroscopy of commensurate density waves. *Synth. Met.* **120**, 695–698 (2001).

-
- [14] Tomislav Vuletić, **Marko Pinterić**, Martin Lončarić, Silvia Tomić, and J. U. von Schütz. Non-ohmic electrical transport in the Peierls-Mott state of deuterated copper-DCNQI systems. *Synth. Met.* **120**, 1001–1002 (2001).
- [15] **Marko Pinterić**, Tomislav Vuletić, Silvia Tomić, and J. U. von Schütz. Complex low-frequency dielectric relaxation of the charge-density wave state in the $(2,5(\text{OCH}_3)_2\text{DCNQI})_2\text{Li}$. *Eur. Phys. J. B* **22**(3), 335–341 (2001).
- [16] Silvia Tomić, **Marko Pinterić**, Mladen Prester, Đuro Drobac, and Kazumi Maki. Superconductivity and magnetism in organic layered superconductors. *Physica C* **364-365**, 247–250 (2001).
- [17] **Marko Pinterić**, Silvia Tomić, Mladen Prester, Đuro Drobac, and Kazumi Maki. Influence of internal disorder on the superconducting state in the organic layered superconductor κ -(BEDT-TTF) $_2\text{Cu}[\text{N}(\text{CN})_2]\text{Br}$. *Phys. Rev. B* **66**(17), 174521 (2002).
- [18] Silvia Tomić, Tomislav Vuletić, **Marko Pinterić**, and Bojana Korin-Hamzić. Modalities of self-organized charge response in low dimensional systems. *J. Phys. IV* **12**(9), Pr9–211–Pr9–214 (2002).

Biography

I was born in Maribor, Slovenia in 1972. I finished elementary and high school in the home town. In 1997 I graduated at the Faculty of Science in Zagreb, Croatia, with the thesis title “Niskofrekventni dielektrični odgovor sumjerljivog vala gustoće naboja” (“The low-frequency dielectric response of the commensurate charge density wave”). Since that same year I have been employed at the Faculty of Civil Engineering in Maribor as an assistant lecturer and an assistant researcher, while the most of my research is performed at the Institute of Physics in Zagreb. In 2000 I won a Master’s degree at Faculty of Science with the thesis title “Niskofrekventna dielektrična spektroskopija i nelinearni električni transport vala gustoće spina” (“Low-frequency dielectric spectroscopy and non-linear electric transport of the spin density wave”).

I am married to Gordana and I am the father of two children, Lucija and Dominik, aged 3 years and 3 months, respectively.

List of Figures

1.1	Proposed phase diagram for κ -(ET) ₂ X quasi-two-dimensional materials. An increase of the ratio of the effective Coulomb interaction and the bandwidth (U_{eff}/W) is analogous to the decrease of the pressure P on the material. Shaded area corresponds to the phase diagram region, in which the ratio U_{eff}/W is critical in regard to the Mott transition. “SC” denotes the superconducting phase.	7
1.2	The experimental phase diagram of κ -(ET) ₂ Cl. “I”, “M”, “AF” and “SC” denote the insulating, metallic, antiferromagnetic and superconducting phases, respectively. Shaded area denotes region of the inhomogeneous phase coexistence, while double-dashed line represents the AF-SC boundary.	8
1.3	BEDT-TTF molecule.	9
1.4	Three-dimensional view of the unit cell for the κ -(ET) ₂ Cl and κ -(ET) ₂ Br crystals.	10
1.5	Three-dimensional view of the unit cell for the κ -(ET) ₂ NCS crystal.	11
1.6	Numerically obtained dispersion relations for the two highest occupied bands. Dashed line designates Fermi energy.	12
1.7	Numerically obtained Fermi surface associated with the half-filled band of Fig. 1.6. The box in the center denotes the Brillouin zone.	13
1.8	Temperature dependence of the Knight shift normalized by its room temperature value for κ -(ET) ₂ Br at 1 bar (●) and 4 bar (○).	14
1.9	$1/T_1T$ versus temperature for κ -(ET) ₂ Br at different pressures: 1 bar (●), 1.5 kbar (Δ), 3 kbar (◇), and 4 kbar (○).	14
1.10	Temperature dependence of the ESR molar magnetic susceptibility for κ -ET ₂ Cl.	15
1.11	Two possible conformations of the ethylene group.	16

1.12	Two possible arrangements of the outer C-C bonds: (a) eclipsed and (b) staggered.	16
1.13	Coefficient of the thermal expansion perpendicular to the planes, α_{\perp} , versus T close to the glass transition for (a) κ -(ET) ₂ Cl (b) κ -(ET) ₂ Br, and (c) κ -(ET) ₂ NCS. Solid and open symbols denote the heating and cooling curves, respectively. No cooling-rate dependence of behavior was observed for rates between -0.02 K/min and -5 K/min.	17
1.14	The resistivity as a function of the temperature for the κ -(ET) ₂ Br sample cooled at different cooling rates.	18
1.15	Torque versus angle in the bc -plane at 4.2 K for two field values. Arrows (1,2,3) and (4) indicate the increasing and decreasing fields ($H = 300$ Oe), respectively.	20
1.16	Lower critical field H_{C1} for κ -(ET) ₂ Br for the field perpendicular to isotropic planes determined by two different methods.	21
2.1	Order parameter $d_{x^2-y^2}$ for κ -(ET) ₂ X materials. Thick lines represent the Fermi surface, lines with a medium thickness superconducting gap and thin lines the Brillouin zone and crystallographic axes. Dashed lines represent node directions in the superconducting gap.	30
3.1	Schematic diagram of the ac susceptibility measurement. For clarity, the secondary coils are drawn outside of the primary coil.	40
3.2	Block scheme of the ac susceptometer.	42
3.3	The κ -(ET) ₂ Br (above) and its reference sample (below).	45
3.4	Approximation of the real sample with face area A and thickness b with the disk of diameter $d = 2\sqrt{A/\pi}$ and length of $l = b$	48
3.5	Simulation of the systematic experimental error in the penetration depth evaluation: the ratio of actual and experimentally obtained penetration depth as a function of experimentally obtained susceptibility for <i>plain</i> calibration (solid lines) and our <i>improved</i> calibration (dashed lines). The circle denotes the area of the most interest.	49
3.6	Simplified depiction of the sample in (a) $H_{ac} \parallel$ plane and (b) $H_{ac} \perp$ plane geometry. Shaded parts of the sample represent the volume penetrated by the magnetic field. Condition $\lambda_{out}/\lambda_{in} \gg l_{in}/l_{out}$ in (a) ensures that λ_{in} can be neglected in the analysis.	52

3.7	Simplified depiction of the sample in the $H_{ac} \parallel$ plane geometry for the situations (a) when the sample sides are perfectly aligned to the magnetic field and (b) when the sample sides are canted from the magnetic field direction. Shaded parts of the sample represent the area (volume) penetrated by the magnetic field. λ_{in} contribution is not shown.	53
4.1	The temperature dependence of the dc resistance for the first cooling and the first warming. Insert shows the temperature dependence of the activation energy.	60
4.2	The electrical field dependent conductivity normalized to its ohmic value at six representative temperatures.	61
4.3	The electrical threshold field as a function of the temperature. Full lines correspond to the fit to the expression $E_T(T) = A \exp[-T/T_0] + B$. See the text for details.	62
4.4	The non-ohmic conductivity at twice the threshold field, normalized to its ohmic value, as a function of the temperature.	62
4.5	Frequency dependent real part conductivity normalized to its ohmic value at seven representative temperatures.	63
4.6	The real and imaginary parts of the dielectric function <i>versus</i> the frequency at three representative temperatures. Full lines correspond to fits to the HN function.	64
4.7	(a) Dielectric strength ($\Delta\varepsilon$), (b) width of the relaxation time distribution ($1 - \alpha$), (c) mean relaxation time (τ_0 , points) and dc resistance (R , full lines) <i>versus</i> inverse temperature.	65
4.8	The real part of the dielectric function <i>versus</i> the inverse temperature at a few representative frequencies. A full thick line represent the condition $\omega\tau_0 = 1$	66
5.1	Sample S1: Temperature dependance of resistance.	68
5.2	Sample S2: Temperature dependance of resistivity in cooling and warming half-cycle.	68
5.3	Batch S2: real and imaginary parts of the susceptibility in two distinct directions in the $H_{ac} \parallel$ plane geometry.	70
5.4	Sample S1: real and imaginary parts of the susceptibility for relaxed (R) and quenched (Q) states in the (a) $H_{ac} \perp$ plane and (b) $H_{ac} \parallel$ plane geometry. The arrow in (a) illustrates the upper limit of the systematic error.	72

5.5	Sample S2: real and imaginary parts of the susceptibility for annealed (A), relaxed (R), and quenched (Q) states in the (a) $H_{ac} \perp$ plane and (b) $H_{ac} \parallel$ plane geometry. The arrows in (a) illustrate the upper limit of the systematic error.	73
5.6	Sample S3: real and imaginary parts of the susceptibility for relaxed (R) and quenched (Q) states in the $H_{ac} \perp$ plane geometry. The error bars illustrate the upper limit of the systematic error.	74
5.7	A sample from batch S1: Small jumps in susceptibility for two different cooling rates (a) -0.1 K/min and (b) -100 K/min. Inserts enlarge the range of the greatest interest.	76
5.8	A sample from batch S2: The residual superconductivity in the part of the sample in the temperature region 11–14 K.	76
5.9	Sample S1: (a) in-plane and (b) out-of-plane penetration depths for relaxed (R) and quenched (Q) states. Solid lines represent the fit to the power-law behavior, while the arrow in (a) illustrates the upper limit of the systematic error.	78
5.10	Sample S2: (a) in-plane and (b) out-of-plane penetration depths for annealed (A), relaxed (R), and quenched (Q) states. Solid lines represent the fit to the power-law behavior, while the arrows in (a) illustrate the upper limit of the systematic error.	79
5.11	Sample S1: (a) in-plane and (b) out-of-plane superfluid densities for the ground (R) state. Solid line is a fit to the polynomial expression. A large noise in $\rho_{s,in}$ is due to small values of $\lambda_{in}(0)$ (see text).	82
5.12	Sample S2: (a) in-plane and (b) out-of-plane superfluid densities for the ground (A) state. Solid line is a fit to the polynomial expression. A large noise in $\rho_{s,in}$ is due to small values of $\lambda_{in}(0)$ (see text).	83
5.13	In-plane superfluid density for the ground state of (a) sample S1 and (b) sample S2 without using the <i>improved</i> calibration but rather Eq. (3.15) and the same $\lambda(0)$ values.	85
5.14	In-plane superfluid density for the ground state of (a) sample S1 and (b) sample S2 using Eq. (3.15) and a few chosen $\lambda(0)$ values.	86
5.15	Sample S2: (a) in-plane and (b) out-of-plane superfluid densities for the intermediate (R) state. The solid line is a fit to the polynomial expression, and the dashed line presents the s -wave model (see the text).	88

- 6.1 The effects of the admixing of the s -wave component to the $d_{x^2-y^2}$ -wave, where r represents the s -wave component parameter. (a) The change of the node directions: Thick lines represent the Fermi surface, lines with a medium thickness superconducting gap and thin lines the Brillouin zone and crystallographic axes. Dashed lines represent node directions in the superconducting gap. (b) The change of the volume of the nodal region μ : The thick horizontal line represent the Fermi energy and thin horizontal lines the limits of the thermal excitations. 94
- 6.2 Superfluid density in the $(d+s)$ -wave model for a few values of the s -wave component parameter r 95
- 6.3 The superfluid density as a function of T/T_{C0} for the state with no scattering, and three states with a different degree of the scattering. T_{C0} is the temperature of phase transition for the state with no scattering. Note that all depicted superfluid densities share the same $\lambda(0)$, obtained from the state with no scattering. 97
- 6.4 ac susceptibility of $d(0,0)$ -, $d(2,2)$ -, $d(3,3)$ -, and $d(4,4)$ - κ -(ET)₂Br in the various cooling conditions: a rapid cooling of 10 K/min (\square), a slow cooling of 0.5 K/min (\circ), and an annealing at 70 K for 12h (\diamond). n, n' in $d(n, n')$ represent number of the deuterium in each ethylene group. 100

List of Tables

1.1	Lattice parameters in order of size, the angle between the longest axis and the plane defined by other two axes, and the volume of the unit cell, for the compounds elaborated in this thesis.	9
2.1	Basis functions $\psi_\alpha(\hat{k})$ of even ($S = 0$) representations of group D_{4h} (tetragonal crystals). Γ denotes representation name and d its dimensionality.	29
2.2	Basis functions $\psi_\alpha(\hat{k})$ of even ($S = 0$) representations of group D_{2h} (orthorhombic crystals). Γ denotes representation name and d its dimensionality.	29
2.3	Basis functions $\psi_\alpha(\hat{k})$ of even ($S = 0$) representations of group C_{2h} (monoclinic crystals). Γ denotes representation name and d its dimensionality.	29
5.1	Susceptibility properties, as defined in the text, for (i) sample S1 in the relaxed (ground) and quenched states, and (ii) sample S2 in the annealed (ground), relaxed (intermediate), and quenched states.	75
5.2	Penetration depth properties, as defined in the text, for (i) sample S1 in the relaxed (ground) and quenched states, and (ii) sample S2 in annealed (ground), relaxed (intermediate), and quenched states.	81

Index

- anisotropy, 11, 20, 44, 55, 91
- annealed state, 69
- antiparamagnons, **25**
- BEDT-TTF, **9**, 8–11
- cooling rate sensitivity, **71**, 74, 92
- demagnetization effect, **45**, 45–50
- demagnetization factor, **44**, 44–50, 71
- dielectric strength, 64, **64**, 65, 89
- electrical threshold field, **61**, 62, 89
- Fermi surface, 12–13, 21, 34, 93, 96
- filling factor, 41, **42**, 43, 44, 46
- glass transition, 16–19, 69, 92, 98, 99
- Havriliak-Negami, **64**
- intermediate state, **71**
- Knight shift, 15, 21, **37**
- mean relaxation time, **64**, 65, 66, 90
- node, 22, 30, 34, 94
 - line, 35–38, 96
 - point, 35–38
- order parameter, **28**
- paramagnetic susceptibility, **36**
- paramagnons, **25**
- penetration depth, 20, 21, 39, 51–54, **81**, 77–81, 97–99
- phase transition temperature, 20, 34, **75**, 91, 97–99
- phonons, **25**
- quenched state, 67, 69
- reference sample, **45**
- relative change of the penetration depth, **77**
- relaxed state, 69
- resistivity ratio, 18, 67, **67**, 92
- specific heat, 21, 22, **35**
- spin-lattice relaxation rate, 15, 19, 21, **37**
- stripes, **101**
- superfluid density, **38**, 54–57, 81–87, 93–98
- synthesis, 11, 12, 19, 67, 69, 71, 77, 91–92, 99
- unconventional superconductivity, **25**, **28**
- weak coupling limit, **25**, 33
- width of the relaxation time distribution, **64**, 65, 66, 90
- Yosida function, **36**